2-4-2014

Synthesis and Electron Emission Properties of Aligned Carbon Nanotube Arrays

Suman Neupane
sneup001@fiu.edu

FLORIDA INTERNATIONAL UNIVERSITY

Miami, Florida

SYNTHESIS AND ELECTRON EMISSION PROPERTIES OF ALIGNED CARBON NANOTUBE ARRAYS

A dissertation submitted in partial fulfillment of

the requirements for the degree of

DOCTOR OF PHILOSOPHY

in

PHYSICS

by

Suman Neupane

2014

To: Dean Kenneth G. Furton
College of Arts and Sciences

This dissertation, written by Suman Neupane, and entitled Synthesis and Electron Emission Properties of Aligned Carbon Nanotube Arrays, having been approved in respect to style and intellectual content, is referred to your judgment.

We have read this dissertation and recommend that it be approved.

_____
Yesim Darici

_____
Chulei (Peggy) Wang

_____
Xuewen Wang

_____
Wenzhi Li, Major Professor

Date of Defense: February 4, 2014

The dissertation of Suman Neupane is approved.

_____
Dean Kenneth G. Furton
College of Arts and Sciences

_____
Dean Lakshmi N. Reddi
University Graduate School

Florida International University, 2014

DEDICATION

I dedicate this dissertation to my family members– without their tremendous support and understanding, it would have been impossible to complete this research.

ACKNOWLEDGMENTS

I would like to sincerely thank my advisor, Dr. Wenzhi Li, for his unrelenting support during the course of this dissertation. Working alongside him, I have developed several skills which I cannot explain in this small paragraph. Dr. Li introduced the topic of this dissertation and carefully guided me through it. I am grateful for his guidance and tireless help at each and every step of my research. His constructive approach has guided me through these years and will be a guiding factor towards my future research endeavors.

I would also like to give my special gratitude to Dr. Xuewen Wang for his expert guidance and analytical support. He was always available to answer my questions and provide useful insights to the experimental results. I would also like to thank Dr. Yesim Darici and Dr. Chunlei Wang for their timely support and encouragement at various stages of my PhD research. I would also like to thank Dr. Jin He for his crucial support and the feedback he provided me during the group meetings.

My special gratitude goes to all the group members in NanoPhysics lab at Florida International University. Post-doctoral associates, Dr. Latha Kumari, Dr. Guohai Chen, Dr. Yanli Zhao and, Dr. Mengjin Yang have been there besides me whenever I needed them. I owe special appreciation to Dr. Latha Kumari who taught me several basic laboratory skills during my initial days. Dr. Chen helped me understand the process of electron field emission in carbon nanotubes and I am truly indebted to him. I would also like to express gratitude to my lab mates Yuehai Yang, Kamal Kadel, and Rui Guo for their role during this research. I thank undergraduate students Mauricio Lastres, Melissa Chiarella, Ariel Cabrera, Daniel Martinez, Matthew Fey and High School student

Matthew Llopis for their support and cooperation during this study. I am also thankful to all the faculties and support staff members in the Physics department at Florida International University.

I am grateful to my extended family members including my parents, uncles, aunts, brothers, sisters, cousins, grandparents and in-laws. They have inspired me to join the PhD program and finish it in a timely manner. Their support and understanding has been phenomenal in the last six years. Finally, I would like to thank my wife Prakriti, and daughter Suriti for their unswerving support, without which this work would not be possible.

ABSTRACT OF THE DISSERTATION

SYNTHESIS AND ELECTRON EMISSION PROPERTIES OF ALIGNED CARBON NANOTUBE ARRAYS

by

Suman Neupane

Florida International University, 2014

Miami, Florida

Professor Wenzhi Li, Major Professor

Carbon nanotubes (CNTs) have become one of the most interesting allotropes of carbon due to their intriguing mechanical, electrical, thermal and optical properties. The synthesis and electron emission properties of CNT arrays have been investigated in this work. Vertically aligned CNTs of different densities were synthesized on copper substrate with catalyst dots patterned by nanosphere lithography. The CNTs synthesized with catalyst dots patterned by spheres of 500 nm diameter exhibited the best electron emission properties with the lowest turn-on/threshold electric fields and the highest field enhancement factor. Furthermore, CNTs were treated with NH_3 plasma for various durations and the optimum enhancement was obtained for a plasma treatment of 1.0 min. CNT point emitters were also synthesized on a flat-tip or a sharp-tip to understand the effect of emitter geometry on the electron emission. The experimental results show that electron emission can be enhanced by decreasing the screening effect of the electric field by neighboring CNTs.

In another part of the dissertation, vertically aligned CNTs were synthesized on stainless steel (SS) substrates with and without chemical etching or catalyst deposition.

The density and length of CNTs were determined by synthesis time. For a prolonged growth time, the catalyst activity terminated and the plasma started etching CNTs destructively. CNTs with uniform diameter and length were synthesized on SS substrates subjected to chemical etching for a period of 40 minutes before the growth. The direct contact of CNTs with stainless steel allowed for the better field emission performance of CNTs synthesized on pristine SS as compared to the CNTs synthesized on Ni/Cr coated SS.

Finally, fabrication of large arrays of free-standing vertically aligned CNT/SnO_2 core-shell structures was explored by using a simple wet-chemical route. The structure of the SnO_2 nanoparticles was studied by X-ray diffraction and electron microscopy. Transmission electron microscopy reveals that a uniform layer of SnO_2 is conformally coated on every tapered CNT. The strong adhesion of CNTs with SS guaranteed the formation of the core-shell structures of CNTs with SnO_2 or other metal oxides, which are expected to have applications in chemical sensors and lithium ion batteries.

TABLE OF CONTENTS

LIST OF FIGURES

CHAPTER 1.0

Introduction

The aim of this study is to develop carbon nanotube (CNT) electron emitters with superior field enhancement for possible applications in electron field emission. The approach is to develop CNT emitters that overcome the shortcomings and disadvantages of existing emitters. In this dissertation, the performance of CNT emitters is extensively investigated to develop a better understanding of the process of field emission. Considerable effort has been directed toward the study of CNTs synthesized on conducting substrates like copper or stainless steel. In addition, CNTs/SnO_2 core-shell structures, which have applications as energy storage materials, have been fabricated.

1.1 Overview

Carbon nanotubes have attracted significant research interest after the landmark report on the discovery of CNTs by Iijima in 1991 [1]. Carbon nanotubes exhibit superior chemical stability, remarkable electrical and thermal conductivities and robust structural integrity [2, 3]. Carbon nanotube emitters also demonstrate promising field emission properties with high current densities and low extraction fields as a consequence of their large aspect ratio [4]. In addition, CNT electrodes offer a large surface area for electrolytes and ions to interact, and hence, perform as efficient electrode materials with quick response time. Figure 1.1(a) shows the trend of the number of publications related to CNTs over the period 1990-2010 [5]. The steady increase in publications has been

possible as a result of contributions from many scientists who are doing research in this fast-growing research field.

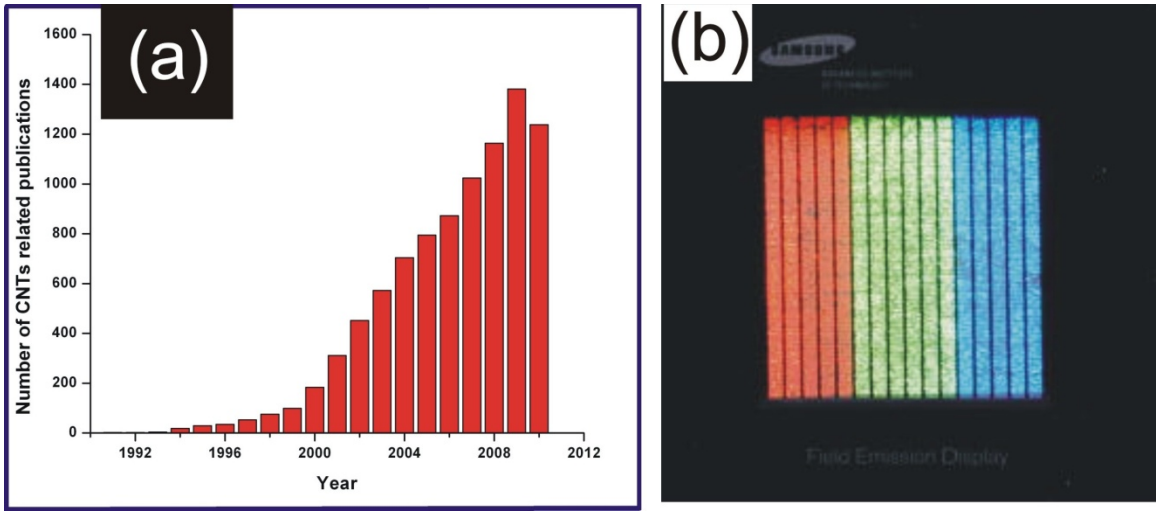

Figure 1.1: *Research trends and applications of CNTs. (a) Number of publications related to CNT growth over last two decades [5]. (b) A 4.5 inch CNT field emission display with red, green and blue phosphor columns [6].*

Electron field emission is the quantum mechanical tunneling of electrons through a triangular potential barrier at the surface of a conductor caused by applying a very high electric field. Arrays of CNT emitters have been used as electron sources in various applications including flat panel displays, cold cathodes, vacuum electronics, and x-ray sources [7-9]. The devices that use electron field emission offer a wide view, high brightness displays with excellent color and contrast resolution. Samsung developed a prototype 4.5 inch CNT-based display in 1999 (Fig. 1.1(b)) [6], and has since developed a 38 inch color display. Carbon nanotube arrays have also demonstrated the potential for application as efficient electrode material during electrochemical tests [10]. Cyclic voltammetry measurements have demonstrated the superior conductivity and great charge transfer ability of CNT arrays employed as working electrodes. In addition, CNTs have

attracted significant interest as host material for lithium (Li) insertion because of their unique structural, electrical, and mechanical properties. Consequently, there are several reports that have explored the possibility of using CNTs in Li-ion battery for charge storage [11, 12].

The main shortcomings of the presently available CNT emitters is the lack of vertical alignment and their requirement of post growth treatment to transfer the samples onto a conducting substrate [13]. In situ fabrication of CNT emitters on conducting substrates prevents the introduction of impurities and defects on CNTs incurred during the transfer of CNTs. However, a dense growth of CNTs results in the screening of the electric field at the tip of a CNT by the neighboring CNTs and a diminished field enhancement at the CNT tip [14]. Hence, it is more desirable to synthesize CNTs of specific density at a predetermined location. Currently available methods to pattern the catalysts by e-beam lithography and photolithography are relatively expensive and time-consuming. Although chemically treated or plasma etched stainless steel (SS) substrates can be employed to synthesize CNTs [15], the degree of alignment and density of the CNTs synthesized on SS substrate is not satisfactory.

The core-shell structures of CNT/SnO_2 show promising charge/discharge capacity. Most of the reported results for forming CNTs/SnO_2 core-shell structures are dedicated to using wet chemical methods on randomly-oriented multi-walled CNTs [11, 12]. However, vertically aligned CNTs are more promising materials for applications in Li-ion battery and other electrochemical applications because of the availability of higher accessible surface area. The size of SnO_2 nanoparticles coated on CNTs plays a vital role

for the stability of electrodes during lithiation and delithiation cycles. It is reported that uniformly distributed SnO_2 nanoparticles tend to minimize the pulverization failure of SnO_2 coated CNT electrode, thereby, improving the cyclability and performance [12].

One of the possible solutions to fabricate CNT emitters of pre-determined density is achieved by patterning catalyst islands using nanosphere lithography (NSL). Nanosphere lithography is a versatile approach to create catalyst patterns of different densities over a wide range of metallic, semiconducting, or insulating surfaces. Nanospheres, with different diameters, can be used in NSL to change the size of the catalyst dots. Carbon nanotubes synthesized on catalyst dots patterned by NSL and separated by optimum distance experience the minimum screening effects by the neighboring CNTs and demonstrate the improved emission characteristics with a lower turn-on electric field and a higher field enhancement factor.

The field emission performance of CNTs can also be improved by plasma treatment of CNTs. Plasma treatment enhances the electric field emission from CNTs by changing the geometry of their tips, by decreasing the work-function of the CNTs, by changing the morphology and alignment of the CNTs, and by introducing the structural defects. The field emission properties can also be improved by changing the emitter geometry. The degree of alignment and graphitization of CNTs synthesized on SS can be improved by using direct current (DC) plasma enhanced chemical vapor deposition (PECVD) method.

In order to increase the stability of a Li-ion battery, CNTs can be uniformly coated with SnO_2 nanoparticles. The theoretical charge storage capacity of SnO_2 (781

$mAhg^{-1}$) is over twice as much as graphite anodes (372 $mAhg^{-1}$). The greater charge storage capacity of SnO_2 nanoparticles can be incorporated with the strength of CNTs to create electrodes with improved performance compared to conventionally used carbon electrodes. Such core-shell structures are also expected to withstand large volume changes during charging and discharging processes.

1.2 Objectives and scope of the research

The goal of this research was to synthesize arrays of vertically aligned CNTs and to fabricate CNT emitters capable of delivering a stable emission current for an extended period of time. The first part of the research focused on the controlled synthesis of CNT arrays over a wide range of conducting substrates. A novel lithography technique, using polystyrene nanospheres, was employed to create masks over which catalyst patterns were developed to fabricate CNT emitters with various densities [16]. The tests on the performance of the as-synthesized CNT emitters involved a detailed analysis of the various parameters pertaining to electron emission, enhancement of the local electric field at the CNT tips, and stability. In another approach, as-synthesized CNTs were treated with NH_3 plasma and the performance of CNT emitters was studied. Plasma treatment has proven to be an efficient method for enhancing the field emission performance of CNTs by changing the CNT morphology, alignment, work-function, and structural defects [17]. To study the effect of emitter geometry, CNT emitters have been fabricated directly on Cu wires with sharp or flat tips. The nanostructures and field emission properties of CNT emitters on two kinds of surfaces were investigated. In another section of the dissertation, a detailed study of the synthesis of CNTs fabricated on SS has been

performed. The analysis of the topological features of the substrate after chemical etching for different durations helped to achieve an understanding of the evolution of the surface and its subsequent effect on the growth of the CNTs. The electrical properties of the as-synthesized CNTs have been investigated. To study the effect of the adhesion layer between the CNTs and the SS substrate on the field emission performance, CNT arrays were synthesized on pristine SS and Ni/Cr catalyzed SS and tested for emitters. Finally, CNT/SnO_2 core-shell structures were fabricated aiming at applications in energy storage.

1.3 Outline of the dissertation

This dissertation is organized into seven chapters. Chapter 2 is dedicated to the background literature review on CNT structures, methods of synthesis, and their properties. Special attention has been focused on the mechanical, thermal, electrical, and electrochemical properties of CNTs relevant to the scope of the dissertation. The applications of the CNTs have been discussed with an emphasis on electron field emission and energy storage. Chapter 3 describes the experimental procedures involved to create patterns of catalyst dots by nanosphere lithography and the subsequent synthesis of CNTs using PECVD. Various characterization tools employed to evaluate the performance of CNT arrays are also discussed in chapter 3. The results of the enhancement of electron field emission by varying the density of CNTs, changing the geometry of the CNT emitters, and applying NH_3 plasma treatment are discussed in chapter 4. Chapter 5 is dedicated to electron field emission property of vertically aligned carbon nanotubes on stainless steel substrates. Efforts to fabricate CNT/SnO_2 core-shell structure are reported in chapter 6. Finally, chapter 7 summarizes the research results

with recommendations for future research. The flow chart of the dissertation research is shown in Fig. 1.2.

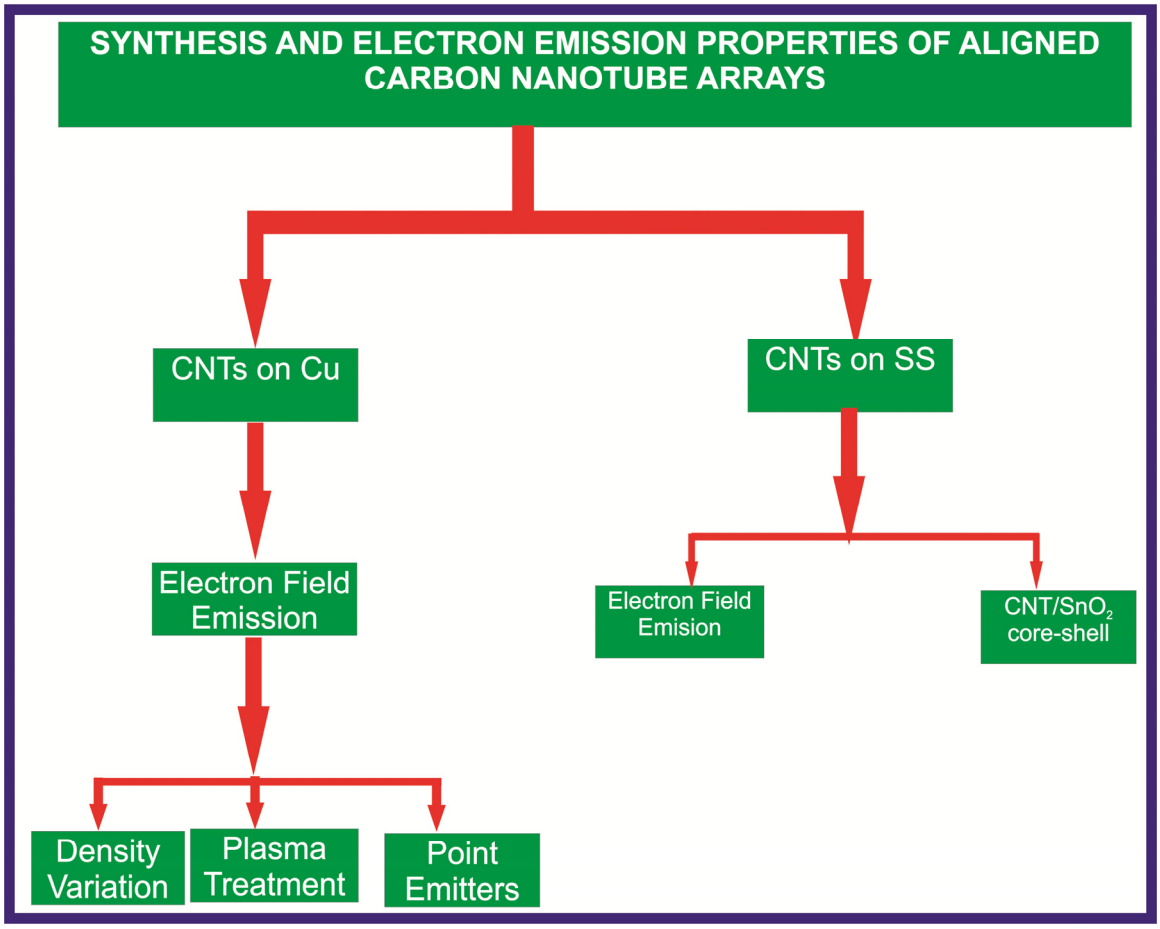

Figure 1.2: *Flow chart of the dissertation research.*

1.4 References

[1] Iijima S 1991 *Nature* 354, 56

[2] Treacy M M J, Ebbesen T W and Gibson J M 1996 *Nature* 381, 678

[3] Berber S, Kwon Y K and Tomanek D 2000 *Physical Review Letters* 84, 4613

[4] Deheer W A, Chatelain A and Ugarte D 1995 *Science* 270, 1179

[5] Hong G, Chen Y B, Li P and Zhang J 2012 *Carbon* 50, 2067

[6] Kim J M, Choi W B, Lee N S and Jung J E 2000 *Diamond and Related Materials* 9, 1184

[7] Lee N S, Chung D S, Han I T, Kang J H, Choi Y S, Kim H Y, Park S H, Jin Y W, Yi W K, Yun M J, Jung J E, Lee C J, You J H, Jo S H, Lee C G and Kim J M 2001 *Diamond and Related Materials* 10, 265

[8] Yue G Z, Qiu Q, Gao B, Cheng Y, Zhang J, Shimoda H, Chang S, Lu J P and Zhou O 2002 *Applied Physics Letters* 81, 355

[9] Milne W I, Teo K B K, Minoux E, Groening O, Gangloff L, Hudanski L, Schnell J P, Dieumegard D, Peauger F, Bu I Y Y, Bell M S, Legagneux P, Hasko G and Amaratunga G A J 2006 *Journal of Vacuum Science & Technology B* 24, 345

[10] Koehne J, Li J, Cassell A M, Chen H, Ye Q, Ng H T, Han J and Meyyappan M 2004 *Journal of Materials Chemistry* 14, 676

[11] Han W Q and Zettl A 2003 *Nano Letters* 3, 681

[12] Wang Z Y, Chen G and Xia D G 2008 *Journal of Power Sources* 184, 432

[13] Tsai T Y, Lee C Y, Tai N H and Tuan W H 2009 *Applied Physics Letters* 95, 013107

[14] Dionne M, Coulombe S and Meunier J L 2008 *IEEE Transactions on Electron Devices* 55, 1298

[15] Masarapu C and Wei B Q 2007 *Langmuir* 23, 9046

[16] Neupane S, Lastres M, Chiarella M, Li W Z, Su Q M and Du G H 2012 *Carbon* 50, 2641

[17] Chen G, Neupane S, Li W Z, Chen L and Zhang J 2013 *Carbon* 521, 468

CHAPTER 2.0

Progress and trends in carbon nanotube research

The present chapter includes a comprehensive summary of peer-reviewed research in the field of carbon nanotubes.

2.1 Structure of carbon nanotubes

Carbon nanotubes (CNTs) can be visualized as sheets of graphene rolled into a tubular structure. A graphene layer is a 2D-sheet of carbon atoms arranged in a hexagonal array such that each carbon atom has three nearest neighbor atoms, Fig. 2.1(a). A single-walled CNT (SWNT) consists of a single layer of graphene rolled into a cylindrical structure while a multi-walled CNT (MWNT) consists of multiple layers of graphite rolled into a cylindrical structure, Fig. 2.1(b). The properties of SWNTs are determined by the diameter and length of the tubes, atomic arrangement available during the rolling, and the presence of defects. The way a graphene layer is wrapped is represented by a pair of indices (*n, m*) called the chiral vector $\boldsymbol{C}_h = n\,\boldsymbol{a}_1 + m\,\boldsymbol{a}_2$ [1]. The integers *m* and *n* denote the number of unit vectors along two directions in the honeycomb crystal lattice of graphite, Fig. 2.1(a). If $m = 0$, the SWNTs are called zigzag nanotubes; if $n = m$, they are called armchair nanotubes; and the remaining are called chiral nanotubes. The difference in the graphene structure creates different band gaps that determine the electrical properties of SWNTs. The electrical conductivity of a SWNT can be easily determined by the (*n, m*) indices of the graphene sheet. A (*n*, *m*) nanotube is metallic if the difference $n - m$ is an integer multiple of three, otherwise, the nanotube is

semi-conducting. Furthermore, the diameter of a SWNT can be expressed in terms of chiral indices (n, m) as $d = \frac{a}{\pi}\sqrt{\left(n^2 + nm + m^2\right)}$, where $a = 0.246\ nm$. While SWNTs can be either metallic or semiconducting, on the basis of tube chirality, MWNTs are conductive, in most cases, as a result of the proximity of parallel graphene sheets.

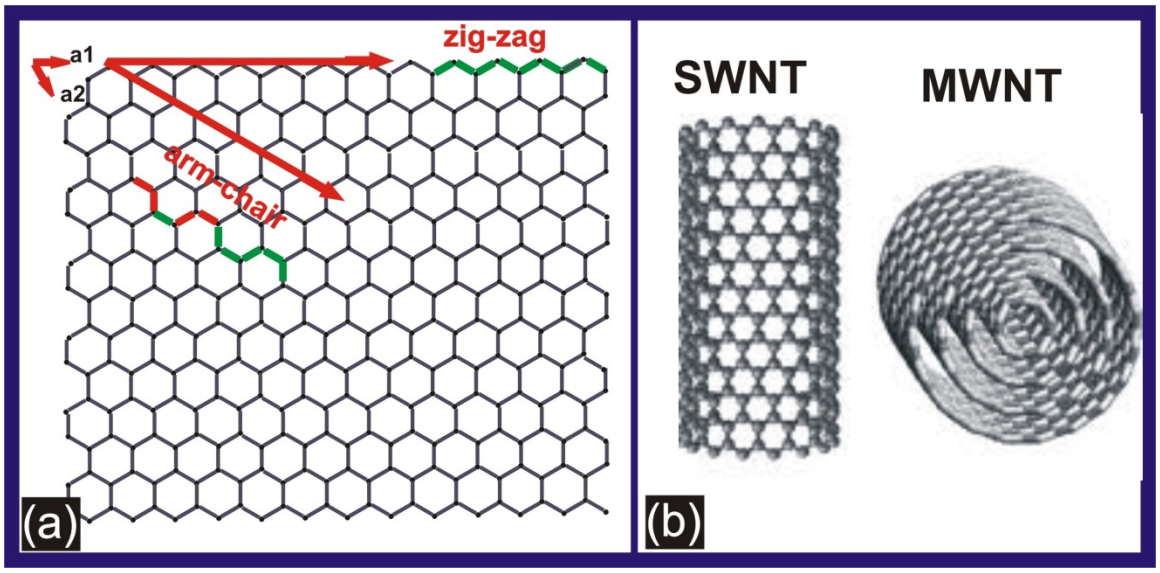

Figure 2.1: *Schematics of a graphene layer and CNTs. (a) Infinite graphene sheet with unit vectors* $\mathbf{a}_1$ *and* $\mathbf{a}_2$*. The red arrows show the directions for rolling of graphene sheets to form a zig-zag or arm-chair CNT. (b) Schematic representation of a SWNT and a MWNT [2].*

2.2 Synthesis methods

Carbon nanotubes can be synthesized using various methods. A detailed description of some commonly used synthesis procedures is provided in the following section.

2.2.1 Arc-discharge method

Iijima reported the discovery of MWNTs synthesized by using an arc-discharge method [3]. A high direct current (DC), typically about 200 A in magnitude, is applied between two graphitic electrodes separated by a distance of about 1 mm inside a chamber filled with Ar gas at 100 torr. The schematic of an arc-discharge apparatus is shown in Fig 2.2(a). The MWNTs had diameters of 4-30 nm and length of about 1 μm. The potential difference of 20 V was maintained between the electrodes. Two years later, Iijima *et al.* and Bethune *et al.*, simultaneously, reported the synthesis of SWNTs [4, 5]. Iijima *et al.* added an iron catalyst to the graphitic electrode in the arc-discharge chamber filled with a gas mixture consisting of CH_4 at 10 torr and Ar at 40 torr. The SWNTs had diameters in the range of 0.7- 1.6 nm and a length about 700 nm. Figure 2.2(b) shows the electron micrographs of CNTs having 5, 2, and 7 walls with diameters of 6.7, 5.5, and 6.5 nm, respectively. The TEM image of a SWNT having a diameter of 1.37 nm and produced by arc-discharge is shown in Fig. 2.2(c). Large scale synthesis of MWNTs was achieved by Ebessen via applying a electrical potential difference of 18 V between the electrodes in helium gas at a pressure of 500 torr [6]. Journet *et al.* synthesized SWNTs, on a large scale, using a mixture of metallic catalysts and graphite powder placed in a

graphite anode. The arc-discharge was created by a current of 100 A; a voltage drop of 30 V between two electrodes was maintained in a helium environment at 495 torr [7].

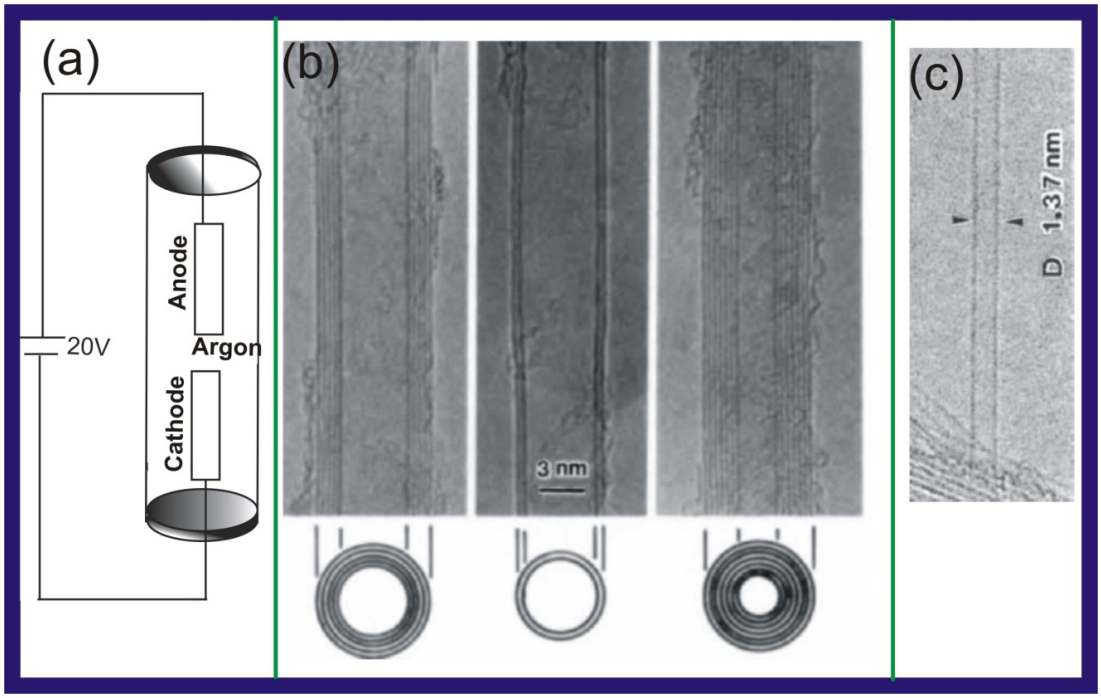

Figure 2.2: *Schematic of the arc-discharge apparatus and transmission electron micrographs of CNTs. (a) Schematic of arc-discharge method. (b) Electron micrographs of MWNTs having 5, 2, and 7 walls, respectively [3]. (c) Electron micrograph of a SWNT with a diameter of 1.37 nm produced by arc-discharge method [4].*

2.2.2 Laser ablation method

Laser ablation is a process of removing particles from a solid surface by irradiating the surface with a high-energy laser beam. Guo *et al.* pioneered the large scale synthesis of CNTs by using Nd:YAG laser pulses over a graphite target heated to 1200 ºC inside a 50-cm-long, 2.5-cm-diameter quartz tube, Fig. 2.3(a) [8]. The graphite target was heated inside the tube with the pressure maintained at 500 torr by flowing Ar gas at a

linear flow rate of 0.2 – 2 cm/s. Carbon nanotubes were collected on the Cu rod cooled by circulating water. These MWNTs were 300 nm long and consisted of 4-24 layers of graphite. The quality of the MWNTs declined as the synthesis temperature was reduced from 1200 ºC to 900 °C until no nanotubes were formed at 200 °C. Addition of transition metal catalysts to the graphite targets resulted in the production of metallic SWNT with a yield greater than 70% [9]. These uniform SWNTs self-organized into ropes with bundles of 5-20 nm in diameters and several micrometers in length and exhibited metallic transport properties at room temperature, Fig. 2.3(b).

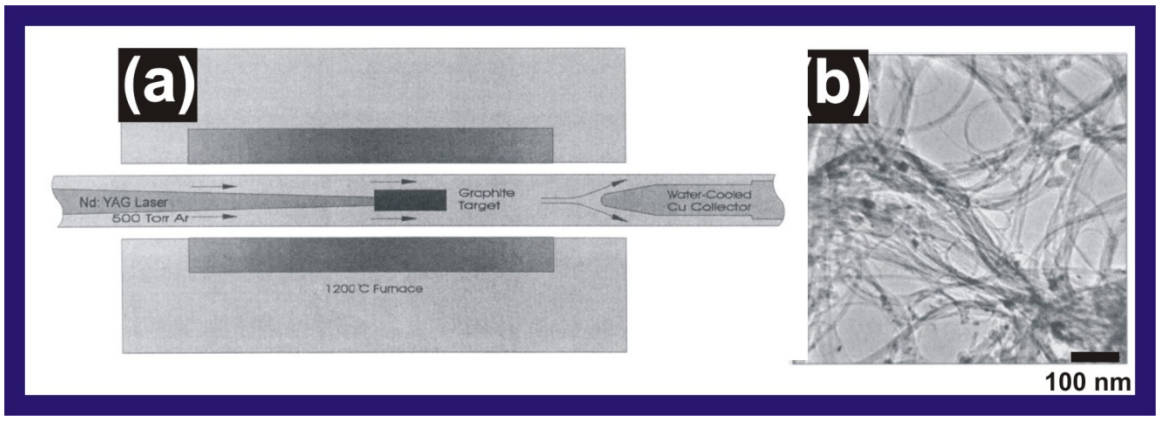

Figure 2.3: *CNTs produced from laser ablation. (a) Schematic of the laser vaporization chamber for the growth of CNTs [8]. (b) TEM image showing ropes of entangled SWNTs together with a small amount of catalyst particles coated with amorphous carbon [9].*

2.2.3 Electrochemical synthesis

Matveev and co-workers synthesized MWNTs using an electrochemical approach [10]. To synthesize MWNTs, dry NH_3 gas was cooled to -40 °C and mixed with C_2H_2 in a glass vessel. The electrolysis of cooled C_2H_2 solution, between metal electrodes, produced carbon on the anode. A DC bias of 150 V was applied between n-type silicon electrodes for 5-10 h during the electrolysis. The atomic hydrogen generated on the cathode during electrolysis facilitated the dissociation of C_2H_2 for the growth of CNTs. The MWNTs were collected at the cathode and consisted of 10-20 graphite layers with an average diameter of 15 nm and aspect ratio (length/diameter) greater than 1000.

2.2.4 Diffusion flame synthesis

Wal *et al.* and Yuan *et al.* have used a simple laboratory-scale diffusion flames at temperatures between 1200-1500 °C for the synthesis of CNTs [11, 12]. Methane mixed with air, was used to produce a stable, visible laminar flame at normal atmospheric pressure. CNTs were deposited on a stainless steel grid held in the flame and supported by an alloy of Ni-Cr-Fe wire. These randomly-oriented and bamboo-shaped CNTs were 20-60 nm in diameter.

2.2.5 Chemical vapor deposition

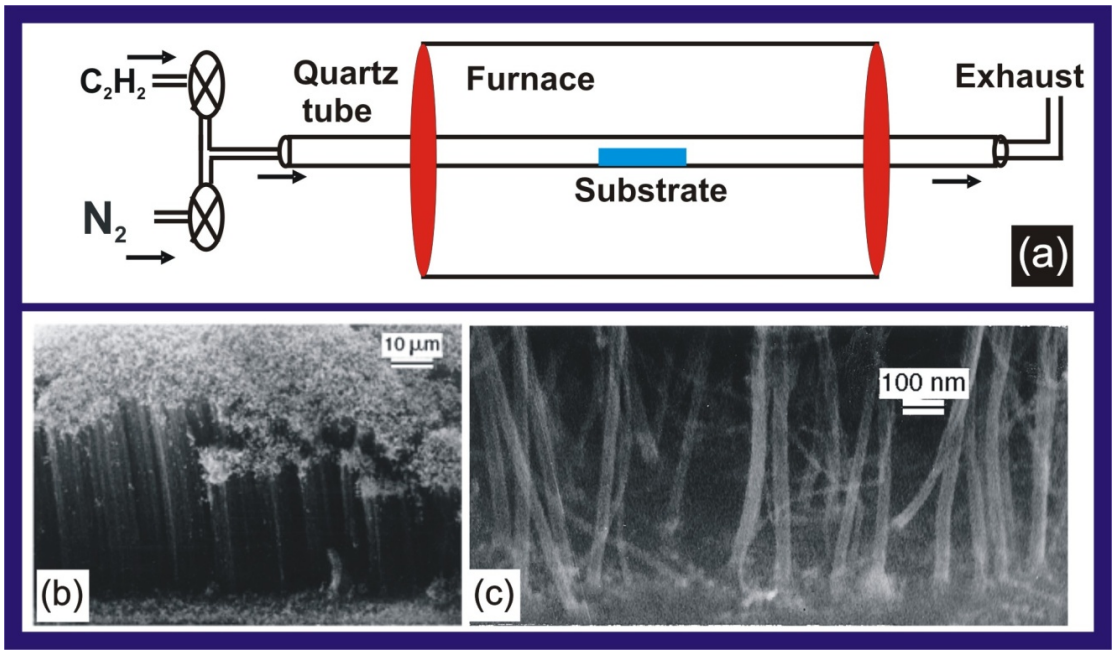

Figure 2.4: *Chemical vapor deposition process. (a) Schematic of the set-up for CVD. The substrate is placed at the center of a quartz tube heated inside a tube furnace. (b) Low magnification SEM images of CNT array synthesized by CVD. (c) High magnification SEM image showing the isolation of CNTs from each other [13].*

Carbon nanotubes were synthesized by Yacaman *et al.* using chemical vapor deposition (CVD) [14]. Iron particles impregnated in a graphite substrate were reduced in a mixture of N_2 and H_2 to form catalyst particles. Then, a mixture of C_2H_2 and N_2 was introduced at 700 °C for several hours at standard atmospheric pressure. The as-grown CNTs measured about 50 µm in length and 5-20 nm in diameter. The diameter and length of the CNTs could be controlled by the concentration of catalysts and the duration of the synthesis time of the CNTs. In a typical CVD process, the synthesis temperature is lower than that in arc-discharge and laser-ablation methods. A substrate is placed inside a

quartz tube heated inside a tube furnace, Fig. 2.4(a). The reaction gases are then decomposed at a high temperature and a pre-determined pressure to produce CNTs. Various transition metal catalysts including Co, Ni, and Fe were used to synthesize CNTs using carbon precursors like CH_4, C_2H_2, C_2H_4 [15-17]. Li *et al.* used CVD to grow arrays of vertically aligned CNTs perpendicular to a silica substrate on a large scale [13]. Mesoporous silica containing iron nanoparticles were prepared by a sol-gel process. Acetylene, diluted by N_2 was used as the carbon precursor to grow 50 μm long CNTs having diameters of about 30 nm separated by ~ 100 nm spacing, Fig. 2.4(b-c). The high resolution TEM images revealed the presence of around 40 concentric graphitic shells with 0.34 nm spacing between two adjacent layers. Vertical alignment of CNTs has also been possible by confining the growth in nanopores of anodic aluminum oxide (AAO) templates [18]. There are also several reports of growth of horizontally aligned CNTs by CVD. The horizontal alignment has been achieved as a result of the application of an external electric field, directed gas-flow in the CVD, lattice-directed growth, and other factors [19-21]. The horizontally aligned CNTs find applications in transistors, sensors, nanofluidic channels, logic gates *etc.*, while vertically aligned CNTs synthesized by CVD have been used to develop electron emitters, scanning probe equipment and other types of devices [22-27].

2.2.6 Plasma enhanced chemical vapor deposition

The PECVD method is used to generate a glow discharge in a reaction chamber by applying a high potential difference between two electrodes. The electric field that results in the plasma enables the growth of a CNT along the direction of the applied

electric field in the PECVD process. Figure 2.5(a) shows a schematic of a typical PECVD apparatus with two parallel plate electrodes separated by about 1 cm. A substrate is placed on top of an electrode heated with a graphitic heater. The annealing treatment, in the presence of gases like NH_3 or H_2, helps in the formation of nanoscopic fine metal catalyst particles of Fe, Ni, or Co on the substrate at elevated temperatures. The plasma discharge dissociates a precursor gas, such as C_2H_2, CH_4, C_2H_4, C_2H_6 *etc*., and assists in the graphitization of carbon atoms to produce vertically aligned CNTs, Fig. 2.5(b). It should be noted that the actual temperature of the substrate during the PECVD growth can be higher than the temperature recorded at the beginning of the experiment with the use of graphitic heater alone in absence of plasma. Vertically aligned CNTs (VACNTs) were synthesized on quartz substrate by using PECVD by Ren *et al.* [28]. The electric field from the plasma helps to maintain the vertical alignment of CNTs and growth has been achieved at lower temperatures than used in conventional CVD processes.

The catalyst film thickness and the diameter of catalyst nanoparticles formed from the catalyst thin film have a strong effect on the diameter, length, growth rate, wall thickness, and morphology of the as-synthesized CNTs. Several versions of the PECVD processes, such as, hot filament-PECVD, microwave-PECVD, radio-frequency PECVD, and inductive-PECVD have been devised to produce VACNTs at lower temperatures than the conventional CVD processes.

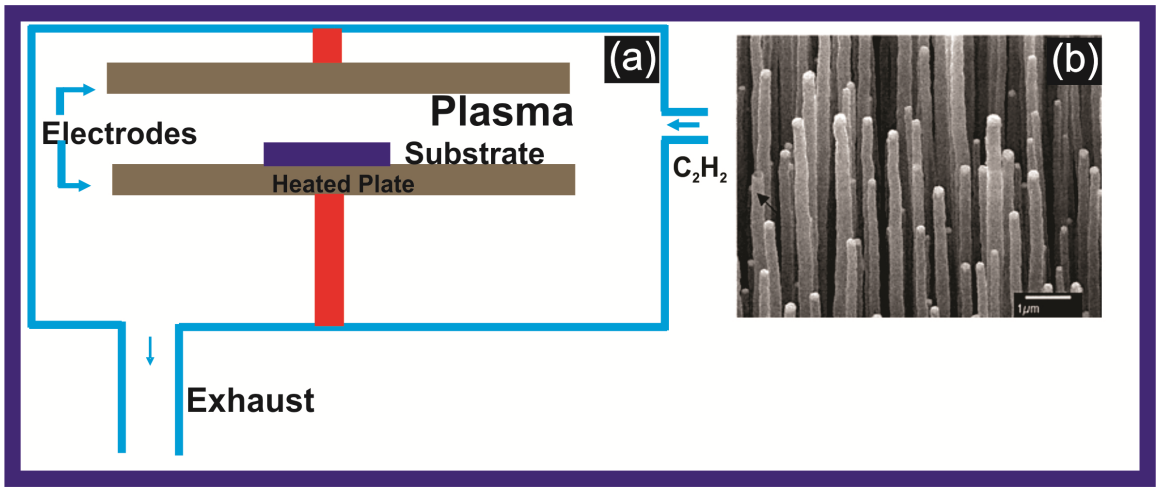

Figure 2.5: *CNTs synthesized from PECVD. (a) Schematic of the PECVD setup. (b) Vertically aligned CNTs synthesized on quartz [28].*

2.3 Mechanical properties of CNTs

The C-C bonding in the graphitic plane is considered to be the strongest bonding in nature and this contributes to the tremendous strength of CNTs. In addition, the low density and fibril shape make CNTs a viable reinforcement material in composites. Theoretical calculations and experimental measurements have yielded an exceptionally high Young's modulus of SWNTs and MWNTs [29]. Treacy *et al.* determined a Young's modulus of 1.8 TPa for individual CNTs by measuring the amplitude of their intrinsic thermal vibrations inside a transmission electron microscope [30]. Wong *et al.* determined a value of 1.3 TPa for the Young's modulus of MWNTs by employing an atomic force microscope (AFM) [31]. Hernandez *et al.* and Gao *et al.* estimated a theoretical value in the range of 0.4-0.6 TPa for the Young's modulus of individual SWNTs [32, 33]. Experimentally, Yu *et al.* obtained an average value of 1 TPa and Zhu *et al.* obtained an average value of ~100 GPa for strands of SWNTs of diameter 5-20 μm,

[34, 35]. On the basis of these exceptional mechanical properties, CNTs have the potential for applications in light-weight, stress-free reinforcement material.

2.4 Thermal properties of CNTs

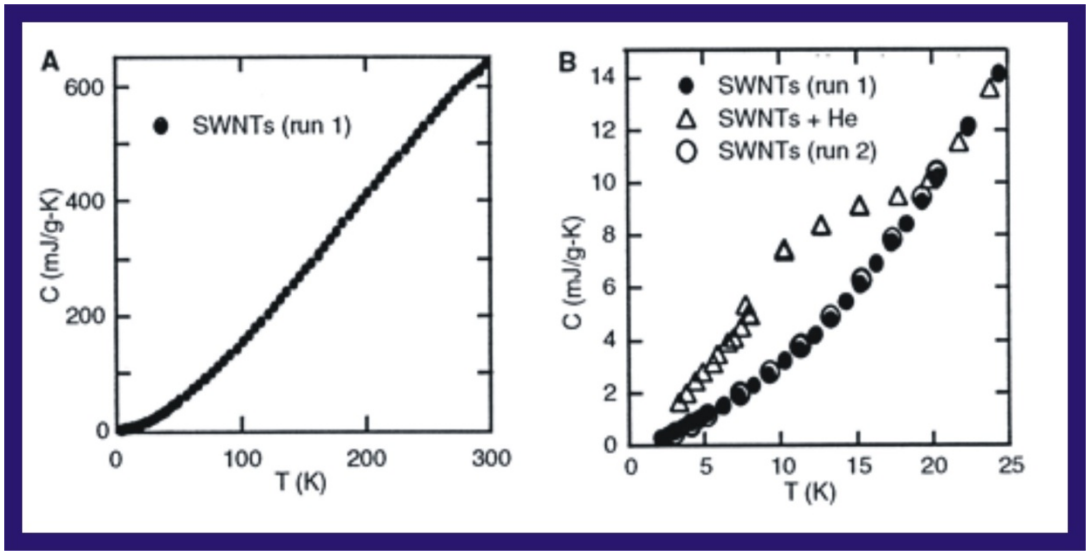

Figure 2.6: *Specific heat capacity of CNTs. (a) Specific heat of a sample consisting mainly of SWNT ropes on cooling from 300 – 2 K. (b) Low temperature behavior of specific heat [36].*

In a graphene sheet, the phonon contribution dominates the electronic contribution to the thermal conductivity and specific heat capacity at lower temperatures. Hence, the thermal transport properties of CNTs are completely characterized by the response of phonons at different temperatures. The specific heat capacity of SWNTs exhibits a linear dependence on temperature from 300 K to 2 K, Fig. 2.6(a), while it exhibits $\sim T^{0.63}$ dependence below 1 K [36-38]. Figure 2.6(b) represents the low temperature behavior of specific heat: solid dots represent the first run (run 1), and open triangles represent a heating run after leaving the sample at 4 K overnight showing the effects of helium adsorption at 4 K and desorption at 20 K. Open circles were recorded

for the second cooling run (run 2) after warming to 77 K and overlap perfectly with the first run. The linear k-vector dependence of the frequency of the longitudinal and twist acoustic phonons results in a linear temperature dependence of the specific heat capacity. The observed behavior of the specific heat capacity below 1 K can be attributed to the transverse acoustic phonons with a quadratic dependence of the wave-vector [39]. These results suggest that inter-wall coupling is rather weak in MWNTs, as compared to graphite, so that one can treat MWNTs as a few decoupled two-dimensional single wall tubules [37].

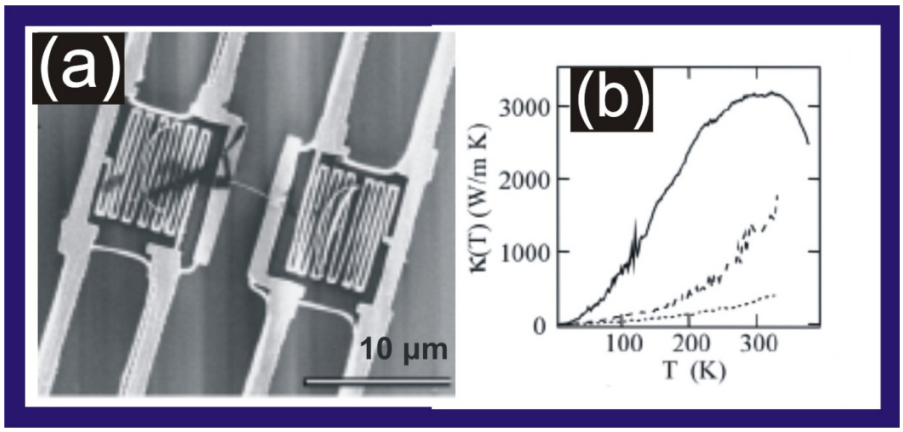

Figure 2.7: *Thermal conductivity of CNTs. (a) SEM image of a suspended CNT device for the measurement of thermal conductivity. (b) The temperature dependence of the thermal conductivity of MWNT samples [40].*

Kim *et al.* measured the thermal conductivity of a suspended microdevice fabricated with CNTs [40]. In the experimental setup, the islands of two silicon nitride membranes were suspended on silicon nitride beams. A platinum thin-film resistor served as a heater on each of the islands. A small bundle of CNTs formed a bridge between the islands to form a thermal contact, Fig. 2.7(a). The thermal conductivity (κ) of MWNTs is

linear above 120 K and becomes almost quadratic ($\kappa \propto T^{1.98\pm0.03}$) at lower temperature, Fig 2.7(b). The solid line represent thermal conductivity of an individual MWNT of diameter 14 nm while the broken and dotted lines are for bundles of diameters 80 nm and 200 nm, respectively. The experimental thermal conductivity is more than 3000 W/K·m at room temperatures, which is two orders of magnitudes greater than the estimation using millimeter-sized macroscopic samples of CNT films [37]. The temperature dependence of the thermal conductivity of CNTs exhibits a peak at 320 K because of the onset of Umklapp phonon scattering, Fig. 2.7(b).

Berber *et al.* estimated an unusually high value of 6600 W/K·m for an isolated (10, 10) CNT at room temperature by combining equilibrium and non-equilibrium molecular dynamics simulations [41]. The high value of thermal conductivity is associated with the large phonon mean free paths in the CNTs, while substantially lower values are predicted and observed for the basal plane of bulk graphite. The numerical data indicate that the thermal conductivity of CNTs is reduced significantly in the presence of interlayer coupling. The thermal conductivity of a CNT film consisting of vertically aligned CNTs (VACNTs) arrays on a glass substrate was found to be higher

(8.3082 W/K·m) than CNT composite films (1.2 W/K·m) [42, 43]. Owing to their superior thermal conductivity, CNTs are ideal materials for applications in integrated circuit cooling and heat transferring during the field emission process [44, 45].

2.5 Electrical properties

Over the past decades, great improvements have been made in understanding the unique electronic and electrical properties of CNTs. A brief review of the electrical transport properties of CNTs is presented in the following section.

2.5.1 Electrical conductivity of CNTs

Carbon nanotubes are ideal one-dimensional conductors and exhibit interesting single electron charging, resonant tunneling through discrete energy levels, and proximity induced superconductivity. Langer *et al.* reported on the electrical resistance of a MWNT bundle from room temperature down to 0.3 K in magnetic fields of up to 14 T [46]. The nanotubes exhibited semi-metallic behavior analogous to rolled graphene sheets with a similar band structure. A magnetic field applied perpendicular to the sample axis lowered the resistance. Langer *et al.* further reported on the electrical resistance measurements of individual CNTs down to a temperature of 20 mK [47]. The conductance exhibits a logarithmic temperature dependence and saturates at low temperatures. A magnetic field applied perpendicular to the tube axis increases the conductance and produces aperiodic fluctuations. Bockrath *et al.* measured the electrical properties of bundles of SWNTs [48]. A gap that formed because of suppressed conductance at low bias was observed in the

current-voltage curves at low temperatures, Fig 2.8(a). Further, several prominent peaks are observed in the conductance as a function of a gate voltage which can be explained by Coulomb blockade transport in quantum wires and dots. Tans *et al.* measured the

electrical characteristics of individual SWNTs at different gate voltages [49]. Figure 2.8(b) shows the I-V curves at gate voltage of 88.2 mV for trace A, 104.1 mV for trace B and 120.0 mV for trace C. The inset shows similar I-V curves with a gate voltage ranging from 50 mV (bottom) to 136 mV (top). The I-V curves showed a clear gap around zero bias voltage. For higher voltages, the current increases in steps. The gaps were suppressed for certain gate voltages and have the maximum value corresponding to zero bias voltage. The variation of the gap with gate voltage around zero bias voltage implies Coulomb charging of the tube.

Zhu *et al.* used a lift-off process to pattern catalysts and then used CVD to synthesize vertical CNT arrays [50]. Two-probe electrical measurements of the CNT arrays indicate a resistivity of 0.01 $\Omega \cdot$cm compared to $8 \times 10^{-4}\ \Omega \cdot$cm and $12 \times 10^{-4}\ \Omega \cdot$cm of individual SWNTs, with a capacitance of the nanotube bundle of 2.55 pF as the voltage was scanned from -1 V to 1 V, suggesting the possible use of these CNTs as interconnect materials [50].

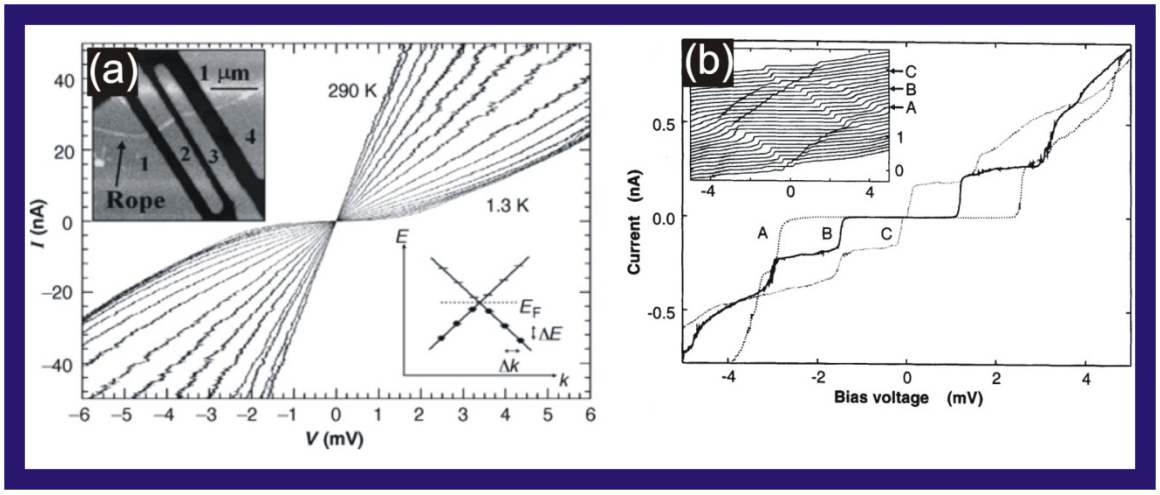

Figure 2.8: *Electrical properties of CNTs. (a) I-V characteristics at different temperatures for the rope segment between contacts 2 and 3. The left inset is an AFM image of the device fabricated to measure the electrical property of a CNT rope. Right inset is schematic energy-level diagram of the two 1D sub-bands near one of the Dirac points with k along the tube axis [48]. (b) I-V characteristics of the nanotube at different gate voltages [49].*

2.5.2 Field emission

Field emission is the quantum mechanical tunneling of the electrons through a potential barrier greater than the kinetic energy of electrons. Carbon nanotubes are a good source of electrons through the process of field emission because of their large aspect-ratio (length/diameter). The emission current from CNTs can be expressed by Fowler-Nordheim (F-N) equation: $I = a\,E_{eff}^2 exp\,(-b/E_{eff})$ where the constants a and b are dependent on the work-function of the material and the local electric field at the emission tip [51]. The effective electric field (E_{eff}) can be expressed as $E_{eff} = \beta E_o$, where E_o is the applied electric field between the CNT emitters and the anode, and β is the field enhancement factor. Carbon nanotubes are ideal materials for the electron field emission

because of their large aspect-ratio which enables a higher field enhancement and consequently the increased emission current.

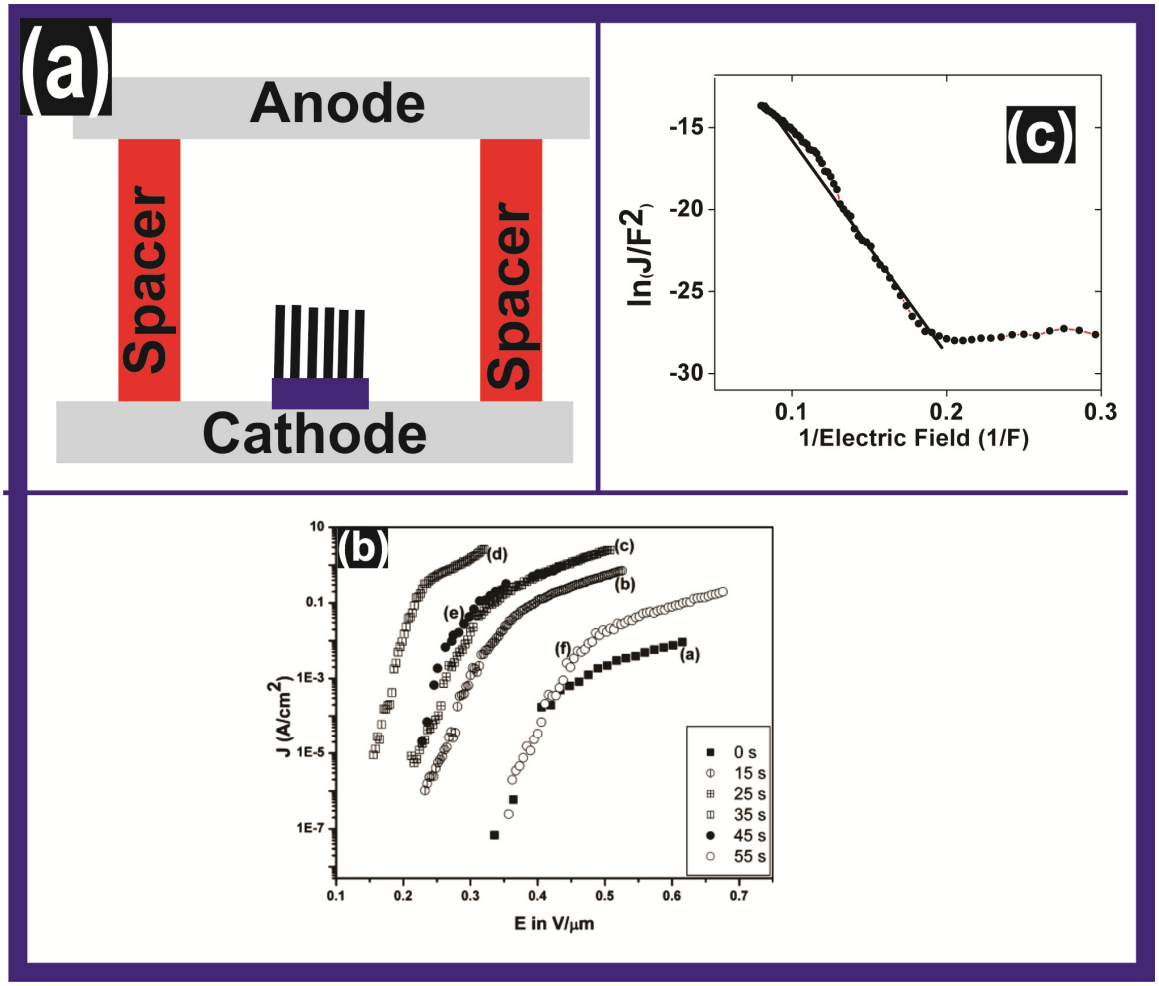

Figure 2.9: *Field emission properties of CNTs. (a) Schematic of the set-up of a CNT based field emission measurement. (b) Typical curves showing the current density (J) of the emission current versus the applied electric field (E) for CNT tips pruned by plasma for different times [52] (c) The linear segment in Fowler-Nordheim (F-N) plot suggests the quantum tunneling of electrons during the process of field emission.*

The experimental setup to measure the field emission property is shown in Fig. 2.9(a). Carbon nanotubes are used as cathodes and a high electric field of the order of ~2 V/μm is created between a metal anode and the CNT cathode to measure electron

emission in a low vacuum of about ~10^{-7} torr. De Heer *et al.* and others determined the emission characteristics of films of oriented nanotubes and as-grown CNT arrays (CNTA) *[51, 53-55]*. De Heer *et al.* pioneered a CNT-film based electron gun to measure the emission current at low applied voltages. The gun was air-stable, easy and inexpensive to fabricate, and stable for a long times.

The total emission current from a CNT forest depends upon the CNTs radius (r), height (h) and spacing (d). The local electric field around the CNT tip is weak when the radius of the CNT is big. Therefore, the average current density decreases with the increment of a CNT radius. The separation between the CNTs influences the distribution of the electric field at the tip of a CNT. When the separation between CNTs becomes large, the screening of electric field is weak and the electric field around the tip of CNTs becomes strong. However, the number of CNTs in the array becomes small and the total emission current is reduced. Therefore, a detailed study of effects of spacing, radius and height of CNTs for the optimum emission current is necessary. Zhang *et al.* reported the experimental and theoretical values of emission from CNTAs, which were consistent with each other [56]. The optimum space (d) between two neighboring CNTs was reported to be about 75 times the radius of CNTs. From the simulation results, the emission current saturated when the height of the CNTs was 2.6 times larger than their separation.

The performance of CNT based emitters can also be improved by other approaches. Hajra *et al.* studied the effect of plasma treatment on the emission current density of CNTs *[52]*. The plasma sharpened tips of CNTs resulted in the dramatic

enhancement of the emission current density by a factor > 10^6 as compared to pristine CNT pillars, Fig. 2.9(b). Saturation in the emission current density was proposed because of the significant change in the tunneling barrier for a nanosized tip in a very high local electric field.

Saurakhiya *et al.* used laser-pruning to modify the structure of as-grown CNTs and studied their field emission current [57]. It was reported that laser modification enhanced the emission current by introducing structural changes to CNTs. Suh *et al.* studied the field-screening effect of highly ordered CNTAs and concluded that field emission was optimal when the tube height was similar to the intertube distance in agreement with the predictions by Nilsson *et al.* [58, 59]. Charlier *et al*. demonstrated that boron doped CNTs exhibited better field emission with a lower threshold voltage than as-prepared CNTs [60].

A typical Fowler-Nordheim (F-N) plot is shown in Fig. 2.9(c). The numerical value for the field enhancement of CNT emitters is estimated from the slope of the straight line observed in the F-N plot.

2.6 Applications of CNTs

The following section will present several interesting applications of materials derived from CNTs including energy storage, high performance sensors, and field emission displays.

2.6.1 Hydrogen storage

Carbon nanotubes, like other allotropes of carbon, have applications in batteries, fuel cells, and electrochemical devices as a consequence of their small dimensions, smooth surface topology and high electron transfer rate at the carbon electrodes. Because of their hollow, cylindrical and nanometer-scale diameters, CNTs can store a significant amount of hydrogen. Dillon and coworkers compared the hydrogen storage capacity of carbon soot containing only about a 0.1 to 0.2 weight percentage of SWNTs to that of activated carbon at 133 K [61]. The SWNTs with diameter of 1.2 nm were synthesized in an electric arc-discharge process. The adsorption of hydrogen on the SWNTs was probed with temperature programmed desorption spectroscopy (TPD) in an ultrahigh vacuum chamber inside a liquid nitrogen cryostat. Hydrogen desorbs from SWNTs and activated carbons within the same temperature range but with different intensities. The signal from SWNTs is ~ 10 times greater than the signal from the activated carbon with the gravimetric storage density in SWNT ranging from ~5% to 10 weight-percent, Fig. 2.10(a).

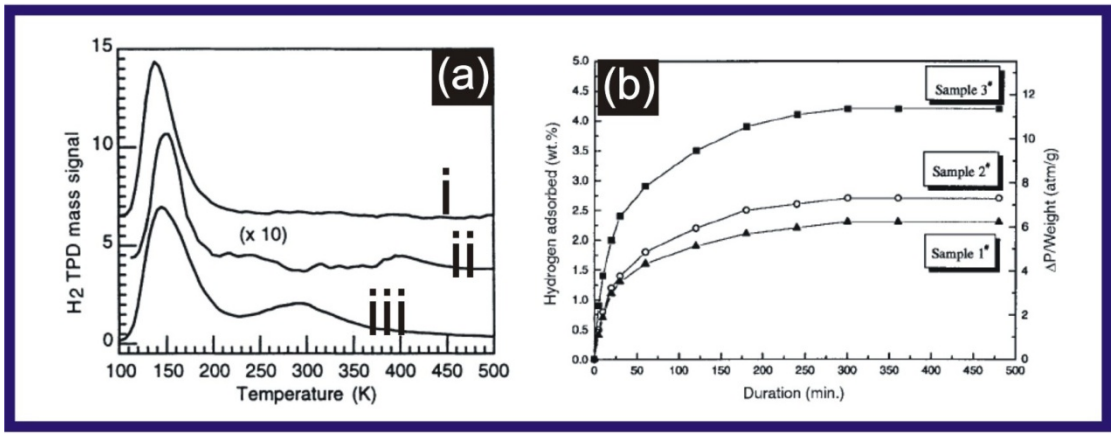

Figure 2.10: *Hydrogen storage in CNTs. (a) Curve (i) is TPD spectra of an as-produced SWNT sample; curve (ii) is from an activated carbon sample (magnified 10 times), and curve (iii) is from SWNT sample after heating in vacuum to 970 K after standard hydrogen exposure [61]. (b) The H_2 uptake of as-synthesized (sample 1), acid-treated (sample 2), and heat-treated SWNTs (sample 3) [62].*

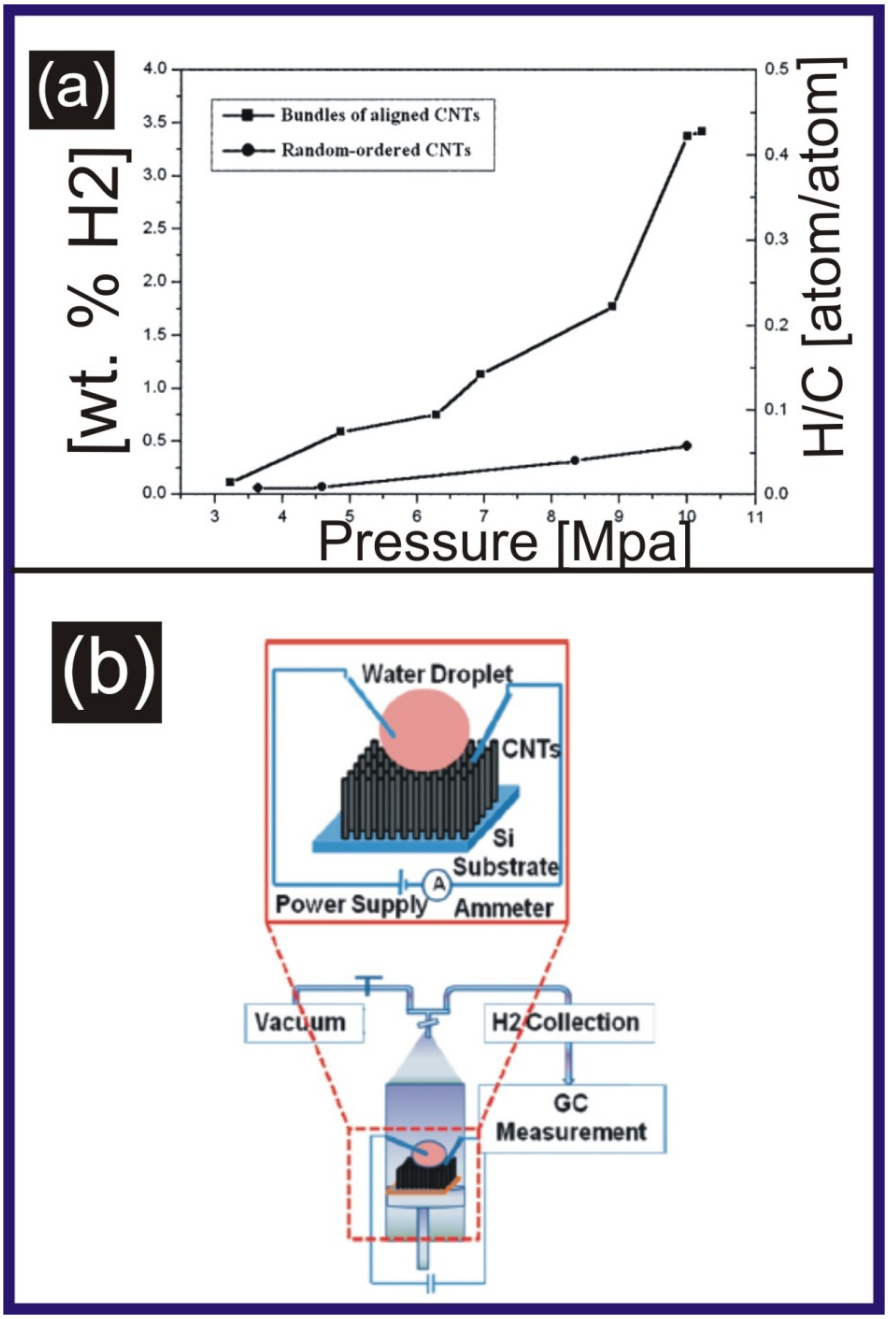

Figure 2.11: *Hydrogen storage in CNT arrays (a) Comparison of H_2 adsorption between bundles of aligned SWNTs and randomly oriented SWNTs [63]. (b) Experimental setup used for measuring electrolytic reaction measurements on the CNT forests [64].*

Liu *et al.* studied hydrogen storage of SWNTs with a mean diameter 1.85 nm, and purity in the range of 50 to 60 weight-percent at room temperature [62]. Fig. 2.10(b) shows the uptake of H_2 for three samples. Sample 1 used as-synthesized SWNTs; sample 2 was soaked in concentrated HCl acid for 48 h to partly eliminate the residual catalysts, then the sample was rinsed with deionized water and dried at 423 K; sample 3 was heated in vacuum at 773 K for 2 h after receiving the same treatment as in sample 2. The heat treatment evaporated the organic compounds and functional groups formed in SWNTs during the synthesis procedure. A hydrogen storage capacity of 4.2 weight-percent was achieved at the pressure of 10 MPa. Furthermore, about 78.3% of the adsorbed hydrogen (3.3 weight-percent) was released under ambient pressure at room temperature. Ye *et al.* demonstrated the adsorption of H_2 exceeding 8 weight-percent on highly purified crystalline ropes of SWNTs at a temperature of 80 K and pressure of ~100 Pa [65].

Zhu *et al.* measured the H_2 absorption of well aligned and randomly ordered MWNTs produced by catalytic pyrolysis on a quartz substrate at 290 K and a pressure between 3-10 MPa [63]. Figure 2.11(a) shows that the bundles of aligned MWNTs are better suited for hydrogen adsorption as compared to randomly ordered MWNTs under similar conditions. The higher H_2 absorption capacity of 3.4 weight-percent of CNTA as compared to 0.5 weight-percent of the random-MWNTs can be attributed to the strong interaction between the H_2 molecules in the interstitial spacing between the CNTs and the inter-layers of some cap-opened CNTs.

Wang *et al.* have performed Monte Carlo simulations to calculate the absorption of hydrogen in tube arrays at 77 K and 298 K [66]. The tube lattice spacing was varied to

study optimum hydrogen uptake using triangular and square lattices. The strength of the solid-fluid interaction potential was adjusted to identify a combination of potential and geometry that meet the Department of Energy (DOE) targets of 6.5 weight-percent for hydrogen storage or fuel cell vehicles. The DOE target values could not be reached even by tripling the fluid-wall potential at ambient temperatures. However, it was possible to achieve the DOE targets at a temperature of 77 K, if the strength of the interaction potential was increased by about a factor of two and the lattice spacing of the tubes was optimized.

Misra *et al.* used electrically conducting surfaces of CNTAs as cathodes for H_2 generation and absorption by electrolyzing water [64]. Figure 2.11(b) shows the experimental setup used for the electrolytic measurements on the CNTAs. An electrochemical cell was assembled by inserting a metal tip connected to a power supply with a deionized water bubble on top of the CNTA acting as the cathode. The DC measurements were performed using a Cascade, M150 probe station, attached to a Keithley-2635 source inside a vacuum chamber. An application of an external voltage between the electrodes resulted in collection of hydrogen gas near the surface of the CNTA from the electrochemical deposition of water. The amount of H_2 measured ($2.2 \pm 0.35 \times 10^{-5}$ gm) is less than the amount of hydrogen expected to be generated (2.6×10^{-4} gm) from flowing current over a period of 1 hour. This observation suggests that the missing H_2 must be stored in CNTs.

2.6.2. CNTs as sensors

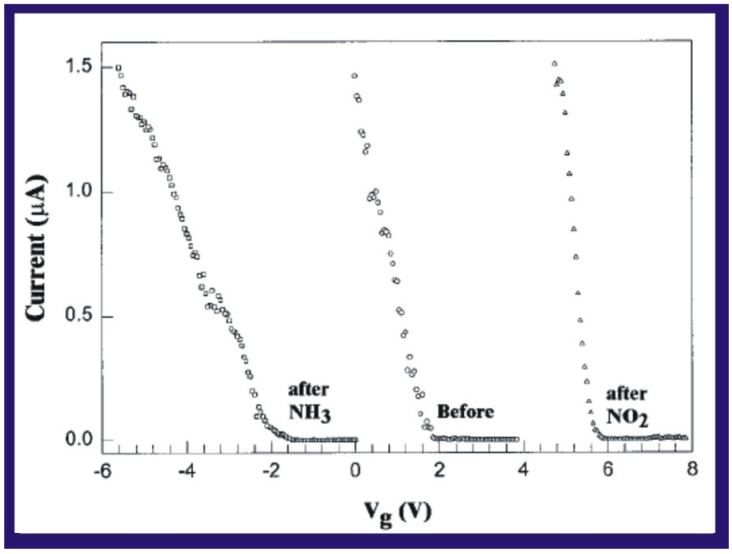

Figure 2.12: *Application of CNTs as gas sensors. Current versus gate voltage curves before NO_2 (circles), after NO_2 (triangles) and after NH_3 (squares) exposure [67].*

Carbon nanotubes can be used as chemical or biological sensors by exploiting their variation in optical, electrical, and electrochemical properties. For example, upon exposure to gaseous molecules like NH_3, NO_2, H_2O_2 *et cetera* or biological species such as enzymes, CNTs exhibit a dramatic increase or decrease in resistance. Sensitivity and recovery time are two key components for the sustainable use of CNTs in detection of foreign elements. Kong *et al.* studied the electric response of semiconducting SWNTs before and after the introduction of NH_3 and NO_2 [67]. The I-Vg curve shifted by -4 V or +4 V when NH_3 or NO_2 was introduced into the chamber, respectively, as shown in Fig. 2.12. These shifts have been explained as the depletion or enhancement of hole carriers brought about by the introduction of the respective gases. Qi *et al.* used arrays of electrical devices each comprised of multiple SWNT sensors for detecting gas molecules

[68]. Polymer functionalization was used to impart high sensitivity and selectivity to the sensors to fabricate n-type nanotube devices capable of detecting NO_2 at less than 1 ppb (parts-per-billion) concentrations while being insensitive to NH_3. Arrays of CNTs have been effectively used to detect glucose, H_2O_2, DNA, protein, and other materials by tracking their electrical or optical response before and after the introduction of particular species [69-71].

2.6.3 CNTs for battery and supercapacitor applications

Carbon nanotubes have applications as electrode materials for highly efficient batteries as a consequence of their high electrochemical stability, large surface area, and unique electrical and electronic properties. Single-walled CNTs exhibit higher capacity for Li intercalation than graphite and disordered carbon. Theoretical calculations predicted the possibility of almost complete charge transfer between Li and SWNTs with relatively small deformation in the structure [72]. Both the interstitial sites and inner side of the tubes are energetically favorable sites for Li intercalation. Theoretical calculations predict the possibility of one Li atom intercalation for every two carbon atoms. Cyclic voltammograms confirm that the reversible intercalation of Li^+ and the presence of Fe, Pt, or Ru nanoparticles within the tube will double the intercalation capacity [73]. Figure 2.13(a) is a schematic illustration of the mechanism of the operation of a Li-ion battery including the movement of the ions between electrodes (solid lines) and electron transport through the complete electrical circuit (dashed lines) during charge (blue) and discharge (red) states [74, 75]. Figure 2.13(b) shows the cyclic efficiency of graphite as a function of added weight percent of CNTs. The efficiency of graphitic anodes increased

continuously until the composition of 10 wt % CNTs which resulted in an efficiency of almost 100% up to 50 cycles [76]. Wu *et al.* demonstrated high Li ion storage capacity at 700 $mAhg^{-1}$ by CNTs [77]. Gao *et al.* improved the storage capacity from 400 $mAhg^{-1}$ for as-prepared SWNTs to 700 $mAhg^{-1}$ after removing impurities and 1000 $mAhg^{-1}$ by ball-milling the SWNTs [78].

The super-capacitance property of CNTs has also been extensively studied because they are able to store and deliver energy rapidly and efficiently for a long life cycle via a simple charge separation process. Ma *et al.* were able to construct electrochemical capacitors based on CNT electrodes with specific capacitances of about 25 Fcm^{-3} with H_2SO_4 as the electrolyte [79]. An *et al.* reported a maximum specific capacitance of 180 F/g and a measured power density of 20 kW/ kg at energy densities in the range of 7 to 6.5 W h/kg by using SWNTs as electrode material in a supercapacitor [80]. Similar measurements also reported the specific capacity of 102 F/g for the electrodes using MWNTs [81].

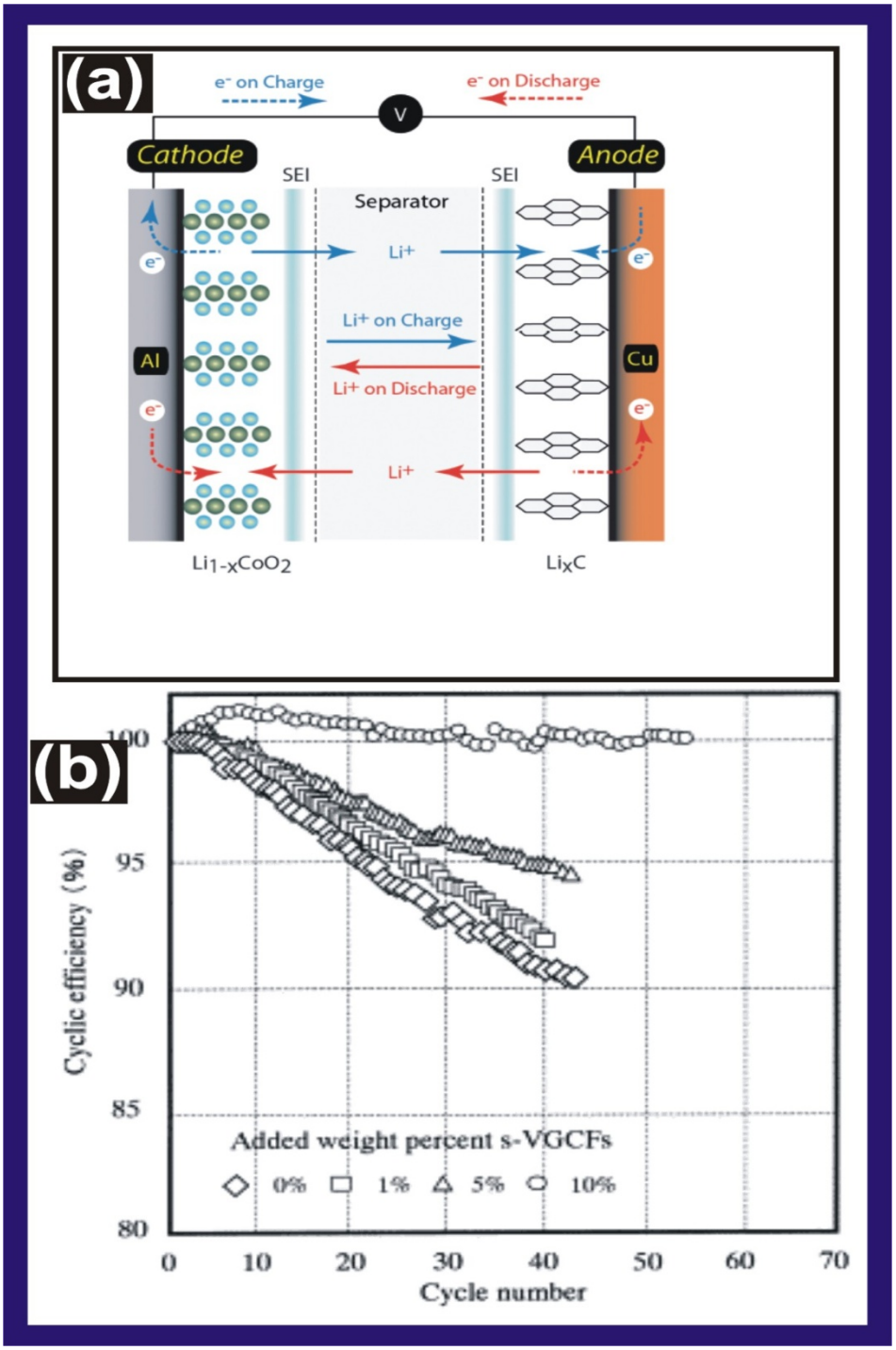

Figure 2.13: *CNTs for Li-ion battery. (a) Schematic of a Li-ion battery [74] (b) The cyclic efficiency of graphite as a function of added weight percent of CNTs [76].*

2.6.4 CNTs for photovoltaic device

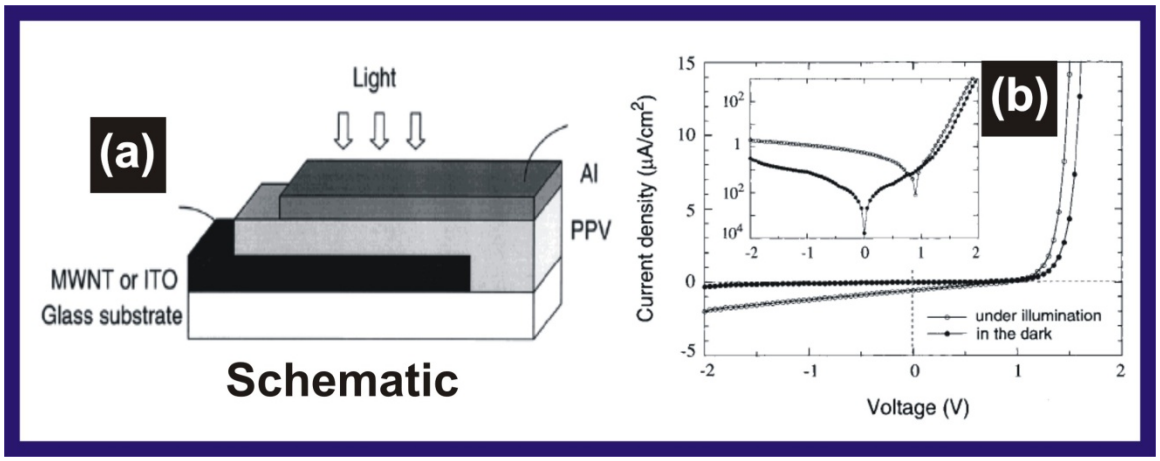

Figure 2.14: *CNTs for solar cells. (a) Schematic of a photovoltaic device. (b) I-V characteristics in the dark (closed circles) and under illumination at a wavelength of 485 nm and intensity of 37μW/cm^2 (open circles). Inset is the representation of the same data with a logarithmic current axis [82].*

Ago *et al.* fabricated a photovoltaic device, shown in Fig. 2.14(a), using MWNTs as an electrode to collect holes and obtained an efficiency twice that of a standard device with an indium-tin oxide (ITO) electrode[82]. Visible light is incident through a semitransparent Al electrode and then passes through polyphenylene vinylene (PPV) of thickness 210 nm and MWNT film of thickness 140 nm in the photovoltaic device. The IV characteristics exhibited a clear diode rectification, Fig 2.14(b). Upon illumination of the device by light of wavelength 485 nm and intensity 37 μW/cm^2, the photocurrent was observed with an open-circuit voltage of 0.90 V along with short-circuit current of 0.56 μA/cm^2. The external quantum efficiency of the MWNT/PPV/Al was typically 1.5 to 2 times greater than the standard ITO device. The higher efficiency could be attributed to the complex interpenetrating network of PPV chains with the MWNT film and the

relatively high work function of the MWNT film. Lagemaat *et al.* have also reported similar successful replacement of In_2O_3:Sn by CNTs in an organic solar cell [83].

2.6.5 CNTs for field emission displays and transistors

Carbon nanotubes have been studied for the possible applications in electron field emission immediately after the understanding of CNT growth, electrical properties, and mechanical properties were established. Nowadays, research is mainly focused on exploiting their superior aspect-ratio and low emission voltage to fabricate CNT-based displays. The field emitting guns of CNTs have promising future in cheap, energy-efficient, and performance-enhanced displays. A single nanotube emitter has been fabricated by physical adhesion on a wire structure or by direct growth on AFM tips [84-86].

Planar emitter can be fabricated by directly growing CNTs on a conducting substrate, by transferring CNT arrays, networks or films on the substrate, or by spraying a CNT suspension on a heated substrate [87-89]. There are also reports of patterned growth of CNTs for the possible application in field emission [90, 91]. All types of CNT emitters have shown remarkable stability with lower extraction fields and higher field enhancement factors. The field emission properties displays a wide range of variation between individual reports by different groups because of the structural difference of the CNTs in aspect ratio, synthesis and measurement condition, open/closed cap structure, presence of defects and other factors.

2.7 Other applications

Carbon nanotubes find applications on scanning probe instruments as a result of their flexibility. CNTs have demonstrated an improved resolution in comparison to conventional metal or Si tips when used as AFM or STM tips [85, 92]. CNTs have been used as electromechanical actuators to mimic the actuating mechanism present in natural muscles. The large elasticity of CNTs allows them absorb enormous energy during collision and makes them ideal component in the development of new structural materials. CNTs have been used to spin fibers with elevated strength for the possible applications in composite materials and other applications [93-95]. Another possible application of CNTs is in molecular transport and drug delivery [96]. The hollow channels in the CNTs provide an ideal model to help understand the transport of organic molecules inside the nanometer sized hydrophobic pores. Carbon nanotubes have an atomically smooth surface over a significant length to allow for the frictionless motion of particles and fluids. Furthermore, CNTs can be used for selective transfer of molecules by suitable modifications. Carbon nanotubes have also been investigated as template material to synthesize other nanostructures [97]. In summary, CNTs have demonstrated a large potential of applications in various fields. CNTs will play an important role in nanotechnology in the coming decades. An extensive study on the CNTs is critical to transfer these academic achievements into industrially scalable products.

2.8 References

[1] Dresselhaus M S and Eklund P C 2000 *Advances in Physics* 49, 705

[2] Dresselhaus M S, Lin Y M, Rabin O, Jorio A, Souza A G, Pimenta M A, Saito R, Samsonidze G G and Dresselhaus G 2003 *Materials Science & Engineering C-Biomimetic and Supramolecular Systems* 23, 129

[3] Iijima S 1991 *Nature* 354, 56

[4] Iijima S and Ichihashi T 1993 *Nature* 363, 603

[5] Bethune D S, Kiang C H, Devries M S, Gorman G, Savoy R, Vazquez J and Beyers R 1993 *Nature* 363, 605

[6] Ebbesen T W and Ajayan P M 1992 *Nature* 358, 220

[7] Journet C, Maser W K, Bernier P, Loiseau A, delaChapelle M L, Lefrant S, Deniard P, Lee R and Fischer J E 1997 *Nature* 388, 756

[8] Guo T, Nikolaev P, Rinzler A G, Tomanek D, Colbert D T and Smalley R E 1995 *Journal of Physical Chemistry* 99, 10694

[9] Thess A, Lee R, Nikolaev P, Dai H J, Petit P, Robert J, Xu C H, Lee Y H, Kim S G, Rinzler A G, Colbert D T, Scuseria G E, Tomanek D, Fischer J E and Smalley R E 1996 *Science* 273, 483

[10] Matveev A T, Golberg D, Novikov V P, Klimkovich L L and Bando Y 2001 *Carbon* 39, 155

[11] Vander Wal R L, Ticich T M and Curtis V E 2000 *Chemical Physics Letters* 323, 217

[12] Yuan L M, Saito K, Pan C X, Williams F A and Gordon A S 2001 *Chemical Physics Letters* 340, 237

[13] Li W Z, Xie S S, Qian L X, Chang B H, Zou B S, Zhou W Y, Zhao R A and Wang G 1996 *Science* 274, 1701

[14] Joseyacaman M, Mikiyoshida M, Rendon L and Santiesteban J G 1993 *Applied Physics Letters* 62, 202

[15] Kukovitsky E F, L'vov S G, Sainov N A, Shustov V A and Chernozatonskii L A 2002 *Chemical Physics Letters* 355, 497

[16] Li J, Papadopoulos C, Xu J M and Moskovits M 1999 *Applied Physics Letters* 75, 367

[17] Cassell A M, Raymakers J A, Kong J and Dai H J 1999 *Journal of Physical Chemistry B* 103, 6484

[18] Hu W C, Gong D W, Chen Z, Yuan L M, Saito K, Grimes C A and Kichambare P 2001 *Applied Physics Letters* 79, 3083

[19] Joselevich E and Lieber C M 2002 *Nano Letters* 2, 1137

[20] Huang S M, Cai X Y and Liu J 2003 *Journal of the American Chemical Society* 125, 5636

[21] Huang S M, Maynor B, Cai X Y and Liu J 2003 *Advanced Materials* 15, 1651

[22] Tans S J, Verschueren A R M and Dekker C 1998 *Nature* 393, 49

[23] Fornasiero F, Park H G, Holt J K, Stadermann M, Grigoropoulos C P, Noy A and Bakajin O 2008 *Proceedings of the National Academy of Sciences of the United States of America* 105, 17250

[24] Huang Y, Duan X F, Cui Y, Lauhon L J, Kim K H and Lieber C M 2001 *Science* 294, 1313

[25] Lee N S, Chung D S, Han I T, Kang J H, Choi Y S, Kim H Y, Park S H, Jin Y W, Yi W K, Yun M J, Jung J E, Lee C J, You J H, Jo S H, Lee C G and Kim J M 2001 *Diamond and Related Materials* 10, 265

[26] Akita S, Nishijima H, Nakayama Y, Tokumasu F and Takeyasu K 1999 *Journal of Physics D-Applied Physics* 32, 1044

[27] Sayago I, Terrado E, Lafuente E, Horrillo M C, Maser W K, Benito A M, Navarro R, Urriolabeitia E P, Martinez M T and Gutierrez J 2005 *Synthetic Metals* 148, 15

[28] Ren Z F, Huang Z P, Xu J W, Wang J H, Bush P, Siegal M P and Provencio P N 1998 *Science* 282, 1105

[29] Sanchez-Portal D, Artacho E, Soler J M, Rubio A and Ordejon P 1999 *Physical Review B* 59, 12678

[30] Treacy M M J, Ebbesen T W and Gibson J M 1996 *Nature* 381, 678

[31] Wong E W, Sheehan P E and Lieber C M 1997 *Science* 277, 1971

[32] Hernandez E, Goze C, Bernier P and Rubio A 1998 *Physical Review Letters* 80, 4502

[33] Gao G H, Cagin T and Goddard W A 1998 *Nanotechnology* 9, 184

[34] Zhu H W, Xu C L, Wu D H, Wei B Q, Vajtai R and Ajayan P M 2002 *Science* 296, 884

[35] Yu M F, Files B S, Arepalli S and Ruoff R S 2000 *Physical Review Letters* 84, 5552

[36] Hone J, Batlogg B, Benes Z, Johnson A T and Fischer J E 2000 *Science* 289, 1730

[37] Yi W, Lu L, Zhang D L, Pan Z W and Xie S S 1999 *Physical Review B* 59, R9015

[38] Lasjaunias J C, Biljakovic K, Benes Z and Fischer J E 2002 *Physica B-Condensed Matter* 316, 468

[39] Popov V N 2002 *Physical Review B* 66, 153408

[40] Kim P, Shi L, Majumdar A and McEuen P L 2001 *Physical Review Letters* 87, 215502

[41] Berber S, Kwon Y K and Tomanek D 2000 *Physical Review Letters* 84, 4613

[42] Shaikh S, Li L, Lafdi K and Huie J 2007 *Carbon* 45, 2608

[43] Huang H, Liu C H, Wu Y and Fan S S 2005 *Advanced Materials* 17, 1652

[44] Xu Y, Zhang Y, Suhir E and Wang X W 2006 *Journal of Applied Physics* 100, 074305 1

[45] Wei W, Liu Y, Wei Y, Jiang K L, Peng L M and Fan S S 2007 *Nano Letters* 7, 64

[46] Langer L, Stockman L, Heremans J P, Bayot V, Olk C H, Vanhaesendonck C, Bruynseraede Y and Issi J P 1994 *Journal of Materials Research* 9, 927

[47] Langer L, Bayot V, Grivei E, Issi J P, Heremans J P, Olk C H, Stockman L, VanHaesendonck C and Bruynseraede Y 1996 *Physical Review Letters* 76, 479

[48] Bockrath M, Cobden D H, McEuen P L, Chopra N G, Zettl A, Thess A and Smalley R E 1997 *Science* 275, 1922

[49] Tans S J, Devoret M H, Dai H J, Thess A, Smalley R E, Geerligs L J and Dekker C 1997 *Nature* 386, 474

[50] Zhu L B, Xu J W, Xiu Y H, Sun Y Y, Hess D W and Wong C P 2006 *Carbon* 44, 253

[51] Deheer W A, Chatelain A and Ugarte D 1995 *Science* 270, 1179

[52] Hazra K S, Rai P, Mohapatra D R, Kulshrestha N, Bajpai R, Roy S and Misra D S 2009 *Acs Nano* 3, 2617

[53] Yuan Z H, Huang H, Dang H Y, Cao J E, Hu B H and Fan S S 2001 *Applied Physics Letters* 78, 3127

[54] Xu D S, Guo G L, Gui L L, Tang Y Q, Shi Z J, Jin Z X, Gu Z N, Liu W M, Li X L and Zhang G H 1999 *Applied Physics Letters* 75, 481

[55] Fan S S, Chapline M G, Franklin N R, Tombler T W, Cassell A M and Dai H J 1999 *Science* 283, 512

[56] Zhang Y N, Lei W, Zhang X B and Wang B P 2005 *Applied Surface Science* 245, 400

[57] Saurakhiya N, Zhu Y W, Cheong F C, Ong C K, Wee A T S, Lin J Y and Sow C H 2005 *Carbon* 43, 2128

[58] Suh J S, Jeong K S, Lee J S and Han I T 2002 *Applied Physics Letters* 80, 2392

[59] Nilsson L, Groening O, Emmenegger C, Kuettel O, Schaller E, Schlapbach L, Kind H, Bonard J M and Kern K 2000 *Applied Physics Letters* 76, 2071

[60] Charlier J C, Terrones M, Baxendale M, Meunier V, Zacharia T, Rupesinghe N L, Hsu W K, Grobert N, Terrones H and Amaratunga G A J 2002 *Nano Letters* 2, 1191

[61] Dillon A C, Jones K M, Bekkedahl T A, Kiang C H, Bethune D S and Heben M J 1997 *Nature* 386, 377

[62] Liu C, Fan Y Y, Liu M, Cong H T, Cheng H M and Dresselhaus M S 1999 *Science* 286, 1127

[63] Zhu H W, Cao A Y, Li X S, Xu C L, Mao Z Q, Ruan D B, Liang J and Wu D H 2001 *Applied Surface Science* 178, 50

[64] Misra A, Giri J and Daraio C 2009 *Acs Nano* 3, 3903

[65] Ye Y, Ahn C C, Witham C, Fultz B, Liu J, Rinzler A G, Colbert D, Smith K A and Smalley R E 1999 *Applied Physics Letters* 74, 2307

[66] Wang Q Y and Johnson J K 1999 *Journal of Physical Chemistry B* 103, 4809

[67] Kong J, Franklin N R, Zhou C W, Chapline M G, Peng S, Cho K J and Dai H J 2000 *Science* 287, 622

[68] Pengfei Q F, Vermesh O, Grecu M, Javey A, Wang O, Dai H J, Peng S and Cho K J 2003 *Nano Letters* 3, 347

[69] Claussen J C, Franklin A D, ul Haque A, Porterfield D M and Fisher T S 2009 *Acs Nano* 3, 37

[70] Cai H, Cao X N, Jiang Y, He P G and Fang Y Z 2003 *Analytical and Bioanalytical Chemistry* 375, 287

[71] Chen R J, Bangsaruntip S, Drouvalakis K A, Kam N W S, Shim M, Li Y M, Kim W, Utz P J and Dai H J 2003 *Proceedings of the National Academy of Sciences of the United States of America* 100, 4984

[72] Zhao J, Buldum A, Han J and Lu J P 2000 *Physical Review Letters* 85, 1706

[73] Che G L, Lakshmi B B, Fisher E R and Martin C R 1998 *Nature* 393, 346

[74] Landi B J, Ganter M J, Cress C D, DiLeo R A and Raffaelle R P 2009 *Energy & Environmental Science* 2, 638

[75] David Linden and Reddy T B eds 2002 *Handbook of Batteries*

[76] Endo M, Kim Y A, Hayashi T, Nishimura K, Matusita T, Miyashita K and Dresselhaus M S 2001 *Carbon* 39, 1287

[77] Wu G T, Wang C S, Zhang X B, Yang H S, Qi Z F and Li W Z 1998 *Journal of Power Sources* 75, 175

[78] Gao B, Kleinhammes A, Tang X P, Bower C, Fleming L, Wu Y and Zhou O 1999 *Chemical Physics Letters* 307, 153

[79] Ma R Z, Liang J, Wei B Q, Zhang B, Xu C L and Wu D H 1999 *Journal of Power Sources* 84, 126

[80] An K H, Kim W S, Park Y S, Moon J M, Bae D J, Lim S C, Lee Y S and Lee Y H 2001 *Advanced Functional Materials* 11, 387

[81] Niu C M, Sichel E K, Hoch R, Moy D and Tennent H 1997 *Applied Physics Letters* 70, 1480

[82] Ago H, Petritsch K, Shaffer M S P, Windle A H and Friend R H 1999 *Advanced Materials* 11, 1281

[83] van de Lagemaat J, Barnes T M, Rumbles G, Shaheen S E, Coutts T J, Weeks C, Levitsky I, Peltola J and Glatkowski P 2006 *Applied Physics Letters* 88, 233503

[84] Smith R C, Cox D C and Silva S R P 2005 *Applied Physics Letters* 87, 103112 1

[85] Tang J, Yang G, Zhang Q, Parhat A, Maynor B, Liu J, Qin L C and Zhou O 2005 *Nano Letters* 5, 11

[86] Druzhinina T S, Hoeppener S and Schubert U S 2010 *Nano Letters* 10, 4009

[87] Lahiri I, Seelaboyina R, Hwang J Y, Banerjee R and Choi W B 2010 *Carbon* 48, 1531

[88] Tsai T Y, Lee C Y, Tai N H and Tuan W H 2009 *Applied Physics Letters* 95, 013107

[89] Jeong H J, Choi H K, Kim G Y, Il Song Y, Tong Y, Lim S C and Lee Y H 2006 *Carbon* 44, 2689

[90] Choi Y C, Shin Y M, Bae D J, Lim S C, Lee Y H and Lee B S 2001 *Diamond and Related Materials* 10, 1457

[91] Jo S H, Tu Y, Huang Z P, Carnahan D L, Wang D Z and Ren Z F 2003 *Applied Physics Letters* 82, 3520

[92] Tung F K, Yoshimura M and Ueda K 2009 *Journal of Nanomaterials* 2009, 612549

[93] Mirfakhrai T, Oh J Y, Kozlov M, Fang S L, Zhang M, Baughman R H and Madden J D W 2009 *Journal of the Electrochemical Society* 156, K97

[94] Wei J Q, Zhu H W, Wu D H and Wei B Q 2004 *Applied Physics Letters* 84, 4869

[95] Qian H, Greenhalgh E S, Shaffer M S P and Bismarck A 2010 *Journal of Materials Chemistry* 20, 4751

[96] Bianco A, Kostarelos K and Prato M 2005 *Current Opinion in Chemical Biology* 9, 674[97] Zhang X T, Lu Z, Wen M T, Liang H, Zhang J and Liu Z F 2005 *Journal of Physical Chemistry B* 109, 1101

CHAPTER 3.0

Experimental procedure and characterization technique

This chapter provides a detailed description on the techniques that are used for the synthesis of vertically aligned carbon nanotubes (VACNTs), the measurement of electron field emission and the fabrication of CNT/SnO_2 core-shell structures.

3.1 Catalyst preparation by nanosphere lithography

Synthesis of aligned CNTs with predetermined density consists of two steps – (i) nanosphere lithography (NSL) and subsequent deposition of catalyst on NSL patterned substrate, and (ii) synthesis by plasma enhanced chemical vapor deposition (PECVD). Nanosphere lithography is a process to form a monolayer of polystyrene spheres (PS) on a substrate to create a mask before catalyst deposition [1]. The catalyst film is then deposited in the interstitial sites of adjoining spheres in a monolayer. Finally, the PS monolayer is removed by chemical lifting to obtain quasi-triangular catalyst dots. Our research group has established NSL as an effective tool for the formation of a monolayer and deposition patterns of catalyst dots with different densities.

In the first step, clean 2 cm × 2 cm Si wafers (donor substrates), were treated in RCA solution for 80 min. The RCA solution contains H_2O_2: NH_4OH: H_2O in a volume ratio of 1:1:5 heated at 80°C. The solution helps to convert the substrate from hydrophobic to hydrophilic [2]. Commercially available (Spherotech Inc.) suspensions of PS (5% weight/volume) with diameters 0.5, 1.0, and 1.8 μm were used to create a monolayer in two steps: spin coating followed by dip coating [3, 4]. The PS suspensions were mixed with ethanol in a volume ratio of 1:7, 1:3, and 1:2 for spheres of diameter

0.5, 1.0, and 1.8 μm, respectively. About 15–20 μL of the mixed solution were then dropped onto the hydrophilic donor substrate, followed by spinning the substrates at a rate of 700 rpm for 40 s. Next, we transferred the monolayer on the donor substrate into a beaker containing deionized water. Finally, the floating monolayer was lifted off the water surface by the recipient substrate. Figure 3.1(a) shows the SEM image of a monolayer of PS forming hexagonally packed structures over a Si acceptor substrate. The recipient substrate was a smoothly polished Cu plate coated with 15 nm Cr layer. Prior to the collection of nanospheres on the recipient substrate, electron-beam (e-beam) evaporation was used to deposit Cr on the Cu substrate at room temperature in an ultra-high vacuum chamber. The recipient Cu substrate was 1 cm × 1 cm × 2 mm and treated in RCA solution for 10 s. The combination of spin-coating and dip-coating facilitated the formation of a well ordered monolayer of PS on the recipient Cr-coated Cu substrate. Finally, a thin layer of 6.5 nm Ni was deposited on the PS patterned recipient substrate by an e-beam evaporation system. The spheres were then removed by sonication in ethanol to obtain a periodic array of quasi-triangular Ni dots over the recipient substrate, Fig 3.1(b).

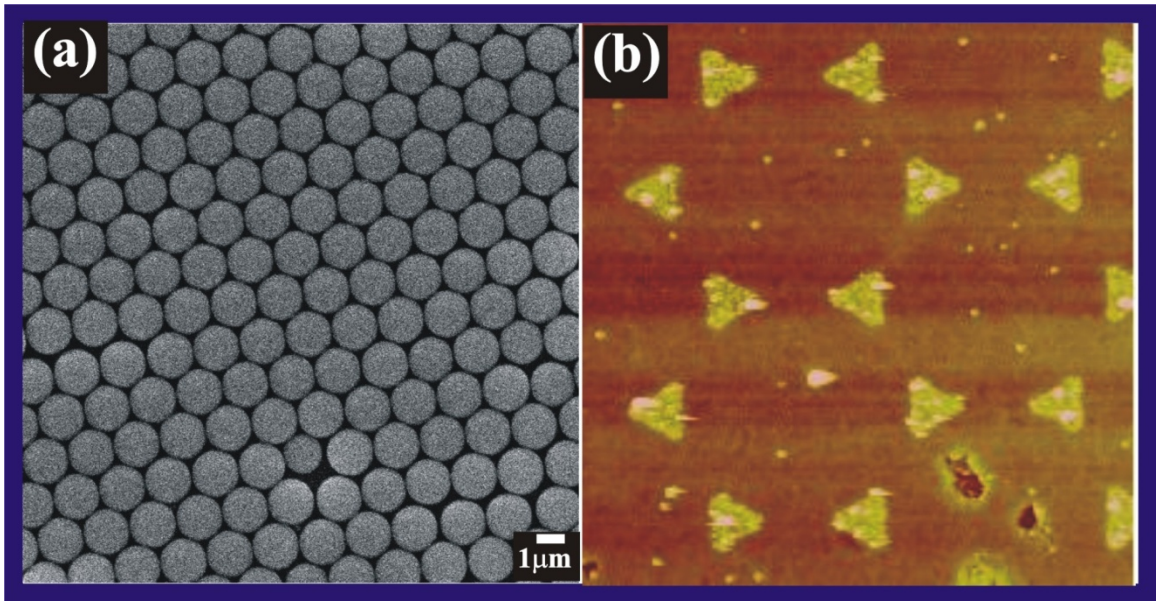

Figure 3.1: *Catalyst deposition by NSL. (a) SEM images of polystyrene monolayer. (b) A representative AFM image of quasi-triangular catalyst dots of Ni obtained on Si substrate after removal of the PS mask with spheres of diameter 1.8 μm.*

Figure 3.2 shows the laboratory set-up of the e-beam deposition apparatus. A beam of electrons, initiated by the increase in the electrical power, resulted in the evaporation of source metal. The thin film of metal is deposited on substrates typically placed at a distance of about 30 cm from the base of the chamber that holds the source metals. The actual thickness of the deposited thin film is recorded by an ultra-sensitive vibrating quartz crystal and read via an Inficon XTM2/Deposition monitor. The inset on the top left of Fig 3.2 shows the schematic of the deposition chamber.

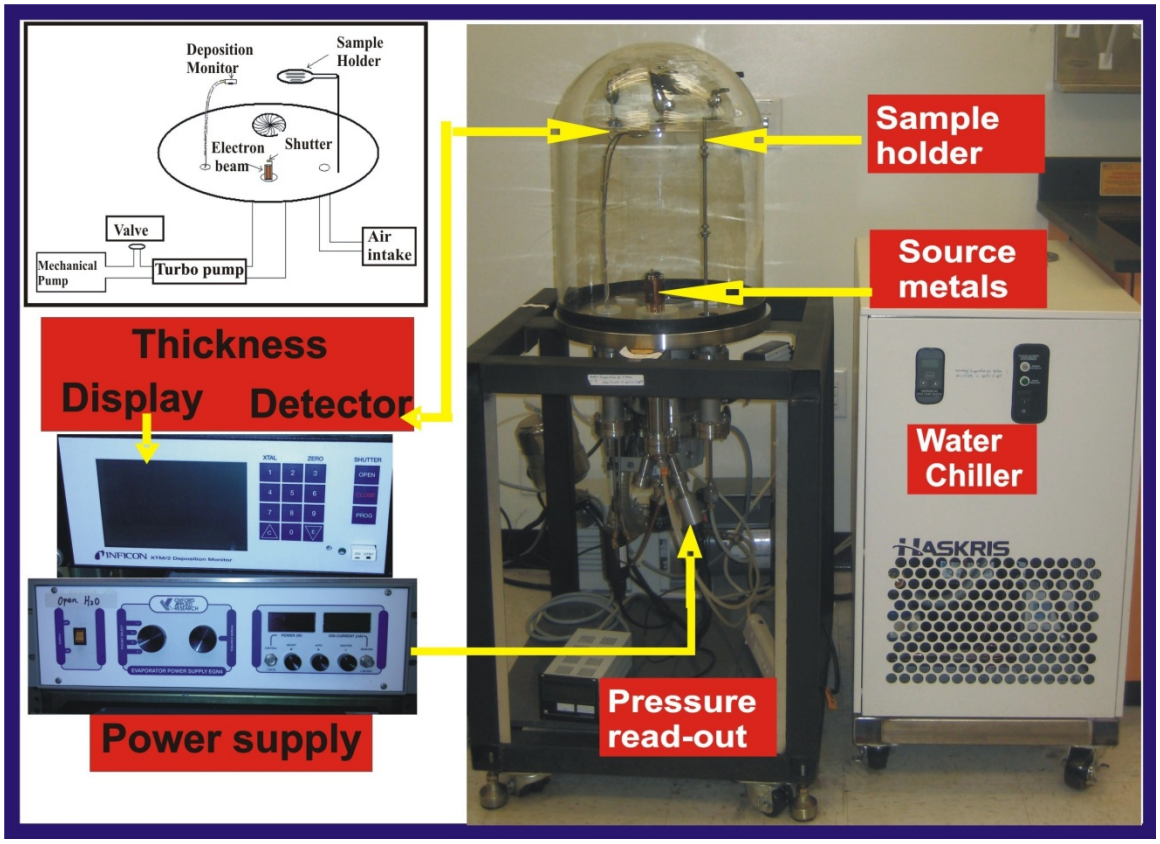

Figure 3.2: *Laboratory set up of the e-beam deposition apparatus. The inset shows the schematic of the deposition chamber.*

3.2 Plasma enhanced chemical vapor deposition

Vertically aligned CNTs were synthesized by choosing and optimizing parameters based on the outcomes of previously published literature [5-7]. Briefly, a substrate was loaded into a PECVD chamber and pumped down to a pressure of 5×10^{-6} torr. For synthesizing CNTs, we used a mixture of C_2H_2 (30 standard cubic centimeter per minute (sccm)) as a carbonaceous precursor and NH_3 (100 sccm) as a diluting and etching gas. The substrate was heated to a required temperature of about 550°C while NH_3 was introduced at a rate of 100 sccm until the pressure in the reaction chamber reached 8 torr.

The power of the DC plasma was maintained at 70 W during the synthesis time. The synthesized CNTs were allowed to cool naturally under high vacuum before further characterization. Table 3.1 presents typical parameters for the synthesis of CNTs on different substrates. Figure 3.3(a) show the laboratory set-up for the PECVD process while the schematic is represented in Fig 3.3(b).

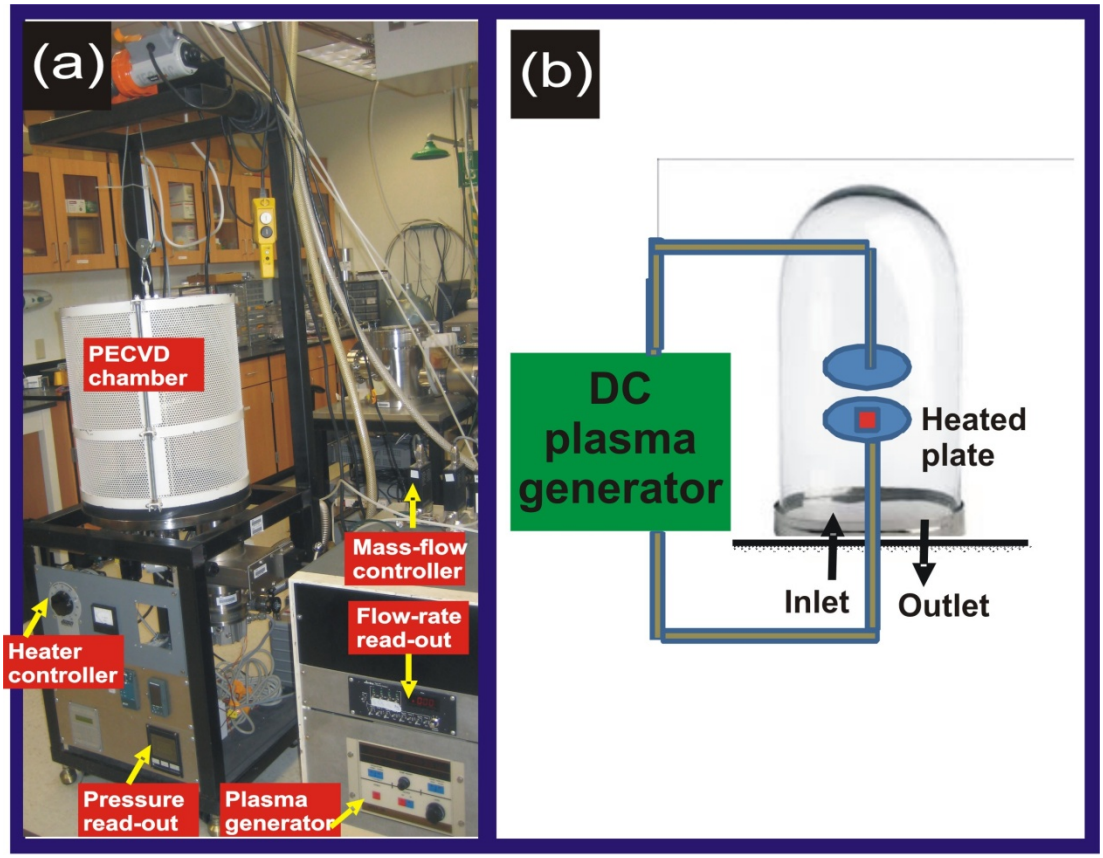

Figure 3.3: *(a) Laboratory set up of the PECVD system. (b) Schematic of PECVD system.*

Table 3.1: *Typical parameters for the synthesis of CNTs on different substrates.*

Substrate	Temperature	Plasma Power	Time	Catalyst thickness
NSL patterned Cu	520 °C	70 W	10 min	Cr (15 nm)/ Ni (6.5nm)
Cu point emitters	520 °C	80 W	10 min	Cr (15 nm)/ Ni (6.5nm)
Stainless steel	600 °C	70 W	5-20 min	(i) None (ii) Cr (15 nm)/ Ni (6.5nm)

3.3 Synthesis of CNT/SnO_2 core-shell structure

The CNTs synthesized on SS were coated with SnO_2 via a wet-chemical route. The CNTs were treated in concentrated HNO_3 for approximately 2 h at room temperature for functionalization and removal of amorphous carbon atoms on the surface [8]. The acid treated samples were then immersed in a solution of 80 mL distilled H_2O, 2 g of $SnCl_2$, and 1.4 mL of HCl (38%) for 15 h for SnO_2 coating. Compressed air was bubbled through the solution to provide a gentle stirring throughout the acid-treatment and coating procedures.

3.4 X-ray diffraction analysis

An X-ray diffraction (XRD) analysis was carried out to identify the phases of SnO_2 present in CNT/SnO_2 core-shell structure. The use of X-ray crystallography allows for determination of the atomic and molecular structure of a crystal in which the crystalline atoms cause a beam of rays to diffract into many specific directions. The XRD measurements were carried out using a Siemens D5000 diffractometer equipped with a Cu anode operated at 40 kV and 40 mA. To obtain an XRD profile, the substrate with as-

synthesized CNTs or SnO_2 coated CNTs was placed directly on the sample stage and targeted with the X-ray beam. The XRD patterns were collected with a step size of 0.01° and a scan rate of 1 sec/step. The SnO_2 phases were determined using the JCPDS standard database.

3.5 Scanning electron microscopy analysis

To image the morphology of the CNTs and polystyrene spheres a JEOL JSM-6330F field emission electron microscope (FE-SEM) operated at 15 kV was used. In FE-SEM, the high-energy incident electron beam interacts with the atoms at or near the surface of a sample. The secondary electrons and back-scattered electrons reflected from the sample reveal the information about the external morphology, orientation, and chemical composition of the sample. To prepare samples for FE-SEM measurements, the samples were directly attached to the sample holder using conducting tape. Samples were sputter coated with gold in some cases to enhance the conductivity and quality of the images.

3.6 Atomic force microscopy

Atomic force microscopy (AFM) is a powerful tool to analyze the surface morphology of different substrates at nanoscale. An AFM consists of a cantilever with a sharp probe at its end which is used to scan the surface of a specimen. As the tip approaches the sample surface, the force between the tip and the sample results into a deflection of the cantilever. The deflection of the cantilever reflects the surface topology of the sample at nanoscopic precision. Tapping mode atomic force microscopy images of

the PS monolayer and stainless steel (SS) surface were acquired by a Veeco Multimode Nanoscope III D. The spring constant of the Si tip was 42 N/m and the resonance frequency was between 250 and 300 kHz. The software used to analyze the surface roughness was Nanoscope Control.

3.7 Transmission electron microscopy analysis

The structural analyses of CNTs were further performed by using a transmission emission microscope (TEM, JEOL-2010F). In a TEM, high-energy electron beam (200keV) is generated to bombard the sample and the transmitted electrons are used to produce an image of the target. To prepare samples for TEM analysis, the CNTs samples are ultrasonically dispersed in ethanol and the solution were drop cast on a carbon-coated copper TEM grid. High-resolution TEM images (HRTEM) and selected area diffraction (SAED) patterns were acquired to understand the crystal structure of CNTs and SnO_2 particles at the atomic level. ImageJ software was utilized for the accurate determination of the lattice spacing between adjacent crystal planes.

3.8 Raman spectroscopic analysis

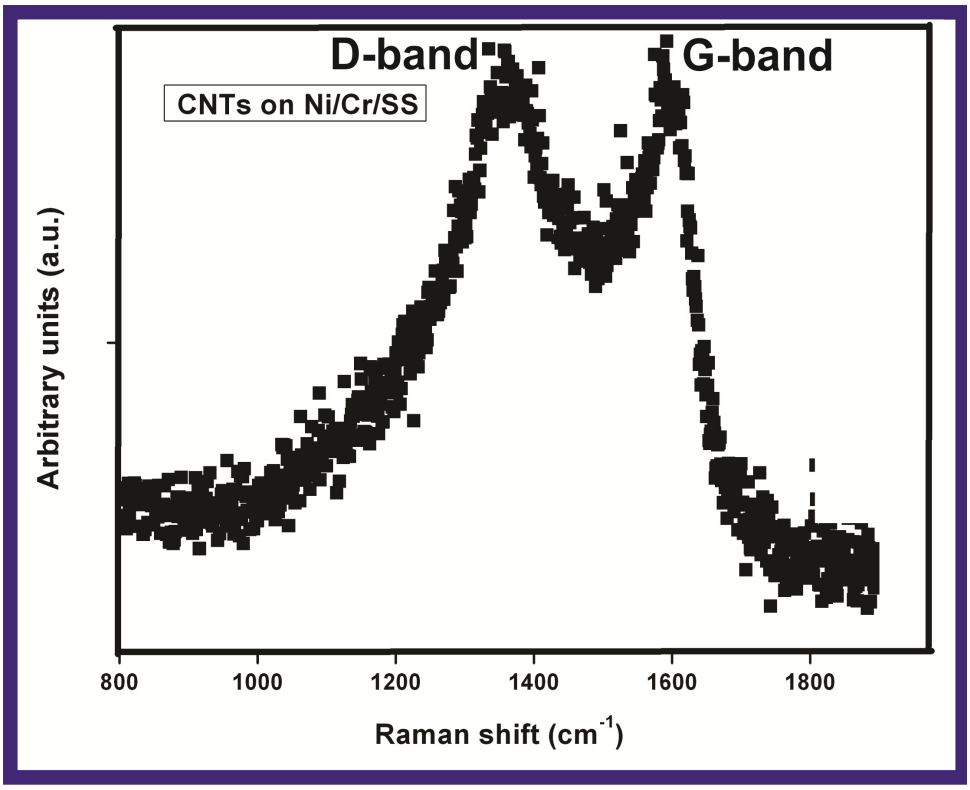

Figure 3.4: *Raman spectra of CNTs synthesized on Ni/Cr coated stainless steel.*

Raman spectroscopy was performed to confirm the degree of graphitization and presence of defect on as-synthesized CNTs. Raman spectrum shows the characteristic peaks for the specific type of bond between the carbon atoms in the CNTs. The G-band in graphite is the result of an optical phonon mode between two dissimilar carbon atoms in the unit cell. The graphitic G-band exhibits one single Lorenztian peak at 1582 cm^{-1} related to the tangential mode of vibration of the carbon atoms. But, the G band in SWNTs is composed of an additional shoulder peak as the consequence of the phonon wave vector confinement along the circumferential direction and because of the symmetry breaking effects [9]. The frequency of radial breathing mode enables the

distinction between metallic and semiconducting SWNTs and the estimation of the diameter of SWNTs. As described earlier in chapter 2, MWNTs contain several graphene layers rolled into a cylindrical structure. Hence, the Raman spectra from individual SWNTs in a MWNT are not so evident because the diameter of the outer tubes differs significantly as compared to the diameter of the inner tubes comprising a MWNT.

The D-band in CNTs is the result of the presence of defects such as vacancies, in-plane substitutional hetero-atoms, and grain boundaries in sp^2 carbon atoms. The characteristic G-band is located between 1330 and 1360 cm^{-1}. The relative intensity of D-band to G-band (I_d/I_g) gives the degree of defects present in the materials [10]. A big ratio of I_d/I_g translates into the presence of large number of defects. Raman spectra of CNT samples were obtained by Ar-ion laser system with 514 nm incident photon operated at a maximum power of 15 mW. The Raman spectra have a resolution of 4 cm^{-1}. Figure 3.4 shows typical Raman spectra of CNTs synthesized on Ni/Cr catalyzed SS. The intensity of D-band is close to the intensity of G-band confirming the presence of a large number of defects in this particular sample.

3.9 Field emission measurements

The field emission measurements were carried out using a diode configuration inside a vacuum chamber at a pressure level of 8×10^{-7} torr. A schematic of the setup of the field emission measurement is shown in Fig. 3.5(a) and the laboratory setup for the measurement of field emission is shown in Fig. 3.5(b). The general purpose interface bus (GPIB) connected directly to a computer is used as a communicating interface while another GPIB acts as the interface between a PC and a power supply. The combination of

these GPIBs helps to protect the PC in case of leakage current while dealing with a very high voltage supply. The separation between the anode and cathode was maintained at 400 μm. The emission current was measured by a Keithley 4200-SCS and the power was provided by a DC power supply (Matsusada AU-15P20). A multiple number of samples with CNTs of various densities were tested to ensure the repeatability and reliability of the obtained results.

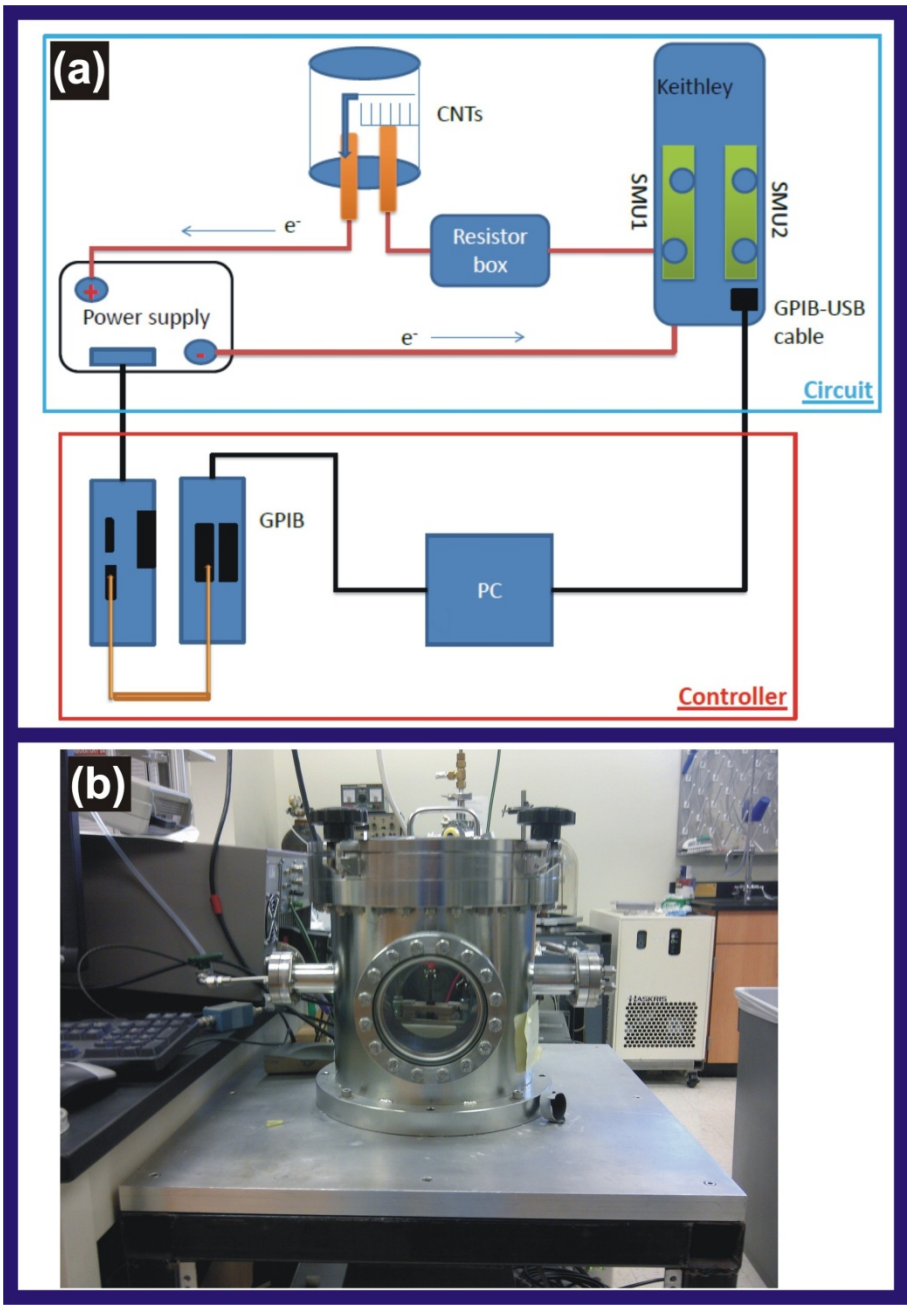

Figure 3.5: *Field emission measurements. (a) A simplified schematic showing the field emission measurement set-up.(b) Laboratory set-up of field emission chamber.*

3.10 References

[1] Hulteen J C and Vanduyne R P 1995 *Journal of Vacuum Science & Technology a-Vacuum Surfaces and Films* 13, 1553

[2] Cheung C L, Nikolic R J, Reinhardt C E and Wang T F 2006 *Nanotechnology* 17, 1339

[3] Jiang P and McFarland M J 2004 *Journal of the American Chemical Society* 126, 13778

[4] Huang Z P, Carnahan D L, Rybczynski J, Giersig M, Sennett M, Wang D Z, Wen J G, Kempa K and Ren Z F 2003 *Applied Physics Letters* 82, 460

[5] Ren Z F, Huang Z P, Xu J W, Wang J H, Bush P, Siegal M P and Provencio P N 1998 *Science* 282, 1105

[6] Park K H, Lee S, Koh K H, Lacerda R, Teo K B K and Milne W I 2005 *Journal of Applied Physics* 97, 024311

[7] Kempa K, Kimball B, Rybczynski J, Huang Z P, Wu P F, Steeves D, Sennett M, Giersig M, Rao D V G L N, Carnahan D L, Wang D Z, Lao J Y, Li W Z and Ren Z F 2003 *Nano Letters* 3, 13

[8] Yu X J, Lin B Y, Gong B B, Lin J X, Wang R and Wei K M 2008 *Catalysis Letters* 124, 168

[9] Dresselhaus M S, Dresselhaus G, Saito R and Jorio A 2005 *Physics Reports-Review Section of Physics Letters* 409, 47

[10] Geng Y, Liu M Y, Li J, Shi X M and Kim J K 2008 *Composites Part a-Applied Science and Manufacturing* 39, 1876

CHAPTER 4.0

Study of electron field emission of carbon nanotubes synthesized on copper

One of the objectives of this research is to explore the electron field emission properties of carbon nanotube emitters to obtain an enhanced field emission. Chapter 4 presents a detailed description of the experimentations and results obtained through rigorous scientific analyses.

4.1 Introduction

Carbon nanotubes (CNTs) exhibit intriguing mechanical, electrical, optical, thermal, and electrochemical properties and have been extensively studied since the landmark paper by Iijima in 1991 [1]. Carbon nanotubes are ideal candidates for field emission applications because of their high electrical and thermal conductivities, tremendous mechanical strength, and high aspect ratio [2]. Carbon nanotubes have shown a potential for application in field emission displays, x-ray sources, lamps, microwave amplifiers, and nanoelectronics [3-7]. Many of these devices require the controlled growth of vertically aligned CNTs (VACNTs) directly on conducting substrates. The CNTs synthesized by arc-discharge and laser ablation methods are highly entangled and possess a lot of impurities [8]. The plasma enhanced chemical vapor deposition (PECVD) process has garnered an appropriate attention because of its ability to synthesize vertically aligned CNT arrays at a predetermined position. It is also desirable to grow CNTs on metallic substrate like Cu, which results in a lower contact resistance as compared to conventional CNTs grown on a silicon substrate. The ohmic contact

between the CNTs and the metallic substrate ensures an easy electron transport while the rigidity of these nanostructures enables the emitters to withstand high current during the process of emission.

Although there have been reports of the synthesis of CNTs using Cu as catalysts [9, 10], it is still challenging to grow well graphitized VACNTs directly over Cu substrates [11, 12]. Dubosc *et al*. have synthesized VACNTs on 400 nm of Cu film on Si/SiO_2 with Ni as catalyst and TiN as a buffer layer using PECVD [13]. Chattopadhyay *et al*. synthesized coiled carbon fibers on hydrogen-fluoride etched Cu substrates by PECVD [14]. Copper has fully filled 3d-orbitals, which prevents the formation of covalent bonds with hydrocarbon molecules. Also, the small binding energy of Cu with carbon subdues the process of graphitization. Furthermore, Cu has low carbon solubility preventing the saturation of carbon atoms required to form the CNT structures [15, 16]. To overcome these problems, a thin buffer layer of Cr or TiN should be deposited on the Cu substrate prior to the deposition of Ni catalyst layer to ensure the synthesis and good adhesion of CNTs with the substrate.

It is possible to enhance the emission properties of CNTs by varying the density of CNTs. A high-density array of CNTs results in the screening of the electric field by the neighboring CNTs and hence the reduction in the emission current, whereas the emission from a low density of CNTs is poor because of the availability of fewer number of emission sites [17]. Selected area low-density growth of CNTs have been achieved by patterning the catalyst using nanosphere lithography (NSL), electron beam lithography, photolithography, focused ion beam lithography, chemical etching, and others [18-23]. A

monolayer of polystyrene spheres (PS) is used to create a mask using NSL. Then, the catalyst is deposited by e-beam evaporation and the PS layer is subsequently removed by wet chemical methods. The VACNTs synthesized over these patterns are expected to exhibit better field emission behavior than the CNT thin films as a result of the decreased screening effect. In the present study, we have employed PS of different diameters to grow CNTs of different densities on Cu substrates and used these CNTs to understand how the densities of CNTs govern the field emission properties.

There have been several reports on the theoretical simulation for the effect of CNT densities on the electron field emission from CNTs. Dionne *et al*. have performed a numerical investigation of the field enhancement factor of individual as well as array of CNTs [24]. It has been reported that CNT emitters have optimal total emission when the spacing between neighboring CNTs is on the order of twice their height. In an array consisting of CNTs with two different heights, there was no significant screening to the electric field of the taller CNTs by the shorter CNTs when the taller CNTs were twice the height of shorter CNTs. Wang *et al*. have solved the Laplace equation for individual CNTs and for the hexagonal arrays of CNTs to understand the influence of intertube distance, anode-cathode distance and the structure of the tip on the field emission [25]. Considering the emission current density, the field emission can be optimal when the intertube distance of CNTs array is close to the CNTs height.

In addition to the improve the electron emission by decreasing the electric field screening, there have been efforts to enhance the performance of existing CNT emitters by doping, plasma irradiation, thermal oxidation, laser pruning, metal coating, *et cetera*

[26-30]. Plasma treatment has been proven as an effective and efficient method to enhance the field emission performance of CNTs by changing the CNT morphology [31], alignment [32], structural defects [33], and work function [34]. Many types of plasma, such as H_2, Ar, CF_4, N_2, and O_2 [31-36], have been investigated.

The performance of the CNT emitters can be improved by varying the morphology of the emitters. The CNT point emitter exhibits a promising choice for some applications such as X-ray sources and electron beam sources because of the small spot size of the electron beam in comparison with the planar field emission electron sources [37]. CNT point emitters have been fabricated by direct growth or by attaching CNTs on tungsten (W) wire or by other methods [38, 39]. Even though these CNT point emitters have demonstrated excellent emission characteristics, they have limited practical applications because of the rapid degradation of the emission capability during emission process. The degradation is often associated with the poor adhesion between the CNTs and the substrate or the shortening of CNTs during the emission process [40]. Few improvements have been made to resolve these issues.

In chapter 4, the synthesis and electron field emission of CNT emitters on Cu substrate are discussed. The effect of the density of CNT emitters, the plasma treatment, and the surface geometry on the electron field emission of the CNT emitters is investigated.

In the present study, we have synthesized dense arrays of VACNTs on Cu substrates with a buffer layer of Cr using PECVD process. We have also employed NSL with PS of different diameters to pattern Ni catalyst dots on which VACNT patterns are

grown. The dense VACNT array and the patterned VACNT arrays allow us to investigate how the variation in spacing between CNTs affects their field emission behavior if the CNTs have a similar height. The growth of patterned CNTs on conducting substrates allows for the in-situ fabrication of electron emitters capable of delivering stable currents under an appropriate vacuum. The enhancement of field emission by the post-growth treatment of the samples by different methods raises an incompatibility issue with the fabricated devices. Hence, it is more desirable to synthesize CNTs of specific density at a predetermined location.

The effects of plasma treatment on the microstructure and the field emission properties of the CNTs were investigated by treating the as-synthesized CNT emitters with NH_3 plasma. It has been found that the CNTs changed from the cylindrical shape to the tapered shape after plasma treatment. The tips of the adjacent CNTs could easily touch each other to form clusters. The plasma treatment also induces some structural defects into CNTs and might result in a doping effect. All of these changes greatly improve the field emission properties of the CNTs.

To study the effect of emitter geometry on the field emission of CNTs, point emitters were directly grown on Cu wires with a flat tip or a sharp tip using PECVD method. The nanostructures and the field emission properties of the two kinds of CNT point emitters were investigated.

4. 2 Experimental

(a) Synthesis of CNT emitters with different densities:

The catalyst pattern of different densities was prepared by using NSL procedures as described in section 3.1. In brief, polystyrene spheres of diameter 0.5, 1.0, and 1.8 μm were used to form a monolayer on a Cr coated Cu substrate. Ni catalyst was then deposited on the NSL patterned Cu and CNTs were finally synthesized by PECVD to synthesize CNTs in different densities.

(b) Plasma treatment of CNTs:

Carbon nanotubes were synthesized using PECVD process as described earlier in section 3.2. The plasma treatment was carried out at 510 ºC under a pressure of 8 torr with a plasma power of 80 W using NH_3 with a gas flow of 100 sccm for 0.5, 1.0 and 2.0 min. The samples were labeled as P-0.0min, P-0.5min, P-1.0min, and P-2.0min for CNTs with plasma treatment for 0, 0.5, 1.0, and 2.0 min, respectively.

(c) Fabrication of CNT point emitters:

Carbon nanotube point emitters were prepared on a Cu wire to understand the field emission properties. Cu wire with a diameter of 1 mm was cut into segments of length 5 mm using scissors. A flat tip (F-tip) was made by polishing one end of the Cu wire using a sand paper while a sharp tip (S-tip) was obtained by etching the Cu wire chemically in a 35 wt% $FeCl_3$ solution for 4 h. The schematic representation of F-tip and S-tip is shown in Fig. 4.1(a). The F-tip and the S-tip were cleaned in acetone bath by ultrasonication, and followed by a similar treatment in alcohol bath to remove any

contaminants. The sharpness of the S-tip was verified by an optical microscope. The prepared Cu wires were then coated with a Cr layer with a thickness of about 15 nm as a buffer layer and then followed by a Ni layer with a thickness of 6 nm as a catalyst film using e-beam evaporation method. VACNTs on the F-tip and S-tip were synthesized using PECVD method as described earlier in section 3.2. The emitters formed by growing VACNTs on the ends of the F-tip and S-tip are illustrated in Fig. 4.1(b), and they will be named as F-tip emitter and S-tip emitter, respectively, in the following text.

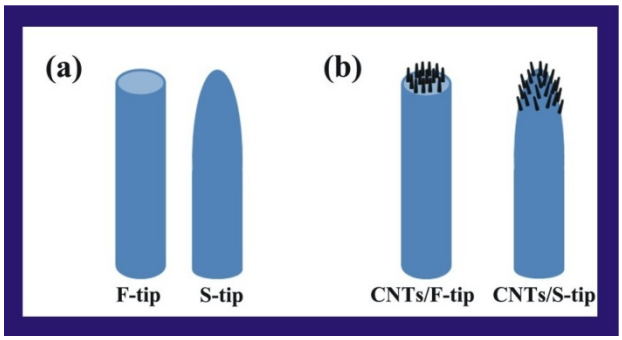

Figure 4.1: *A schematic of the F-tip and S-tip point emitters. (a) before and (b) after CNT growth.*

(d) Field emission measurement:

The field emission measurements were carried out using a diode configuration inside a vacuum chamber as described earlier in section 3.8. The emission performance of CNT emitters were compared by taking into account the following three perspectives:

(i) Effect of CNT emitter densities.

(ii) Effect of plasma treatment for different durations.

(iii) Effect of surface geometry of CNT emitters.

4.3 Results and Discussions

4.3.1 Effects of the densities of CNT emitters on their emission currents

The results of nanosphere lithography employed to pattern catalyst nanodots with different densities and subsequent growth of CNT emitters have been discussed in the following section. The results of the electron emission from CNT emitters with different densities have been discussed.

(a) Nanosphere Lithography:

Nanosphere lithography is an inexpensive and efficient process to selectively pattern catalyst islands over which CNTs can be synthesized. A monolayer of polystyrene spheres of a specified diameter is used to create a mask over which the catalyst is deposited by e-beam evaporation. The interstices between three adjacent spheres in the PS monolayer allow a Ni deposit to form the hexagonal pattern of Ni catalyst. Assuming that the Ni catalyst takes quasi-triangular shape, the size and spacing between the Ni catalyst particles can be calculated [18]. Figures 4.2(a-c) show schematics of the relative variation of catalyst size (d_a) and separation for the catalyst sites (d_s) of closely packed hexagonal structures formed by spheres of diameter 0.5, 1.0, and 1.8 μm, respectively. The site densities of quasi-triangular Ni catalyst dots can be expressed as ($2.3/D^2$), where *D* is the diameter of the sphere. Similarly, the catalyst size is expressed as $d_a = 0.232$ D and their separation is $d_s = 0.577$ D. The size of catalyst dots and catalyst separation increases with the increase of the sphere diameter whilst the site density decreases with the increase of the sphere diameter. The size and separation of the catalyst dots formed

using the spheres of diameter 1.0 and 1.8 μm increase by 100% and 260% compared to that of catalyst dots formed using 0.5 μm spheres. On the contrary, the respective site densities of the catalyst dots formed using 1.0 and 1.8 μm spheres decrease by 75% and 92% as compared to the catalyst dots formed using spheres with diameter of 0.5 μm. The site density, size of a catalyst dot, and the catalyst separation has been presented in Table 4.1 for spheres with different sizes. Figure 4.2(d) shows the SEM image of a typical honeycomb structure of the PS mask formed by the spheres of diameter 1.0 μm. The Ni particles deposited through three adjacent spheres form hexagonal arrays of quasi-triangular catalyst sites as seen in Fig. 4.2(e). The observed separation of the catalyst sites and their size distribution matches well with the theoretical predictions.

Table 4.1: The variation in site density, catalyst size and catalyst separation for spheres of different diameters.

Sphere size (μm)	Site density (per cm^2)	Catalyst size (μm)	Catalyst separation (μm)
0.5	9.2×10^8	0.116	0.289
1.0	2.3×10^8	0.232	0.577
1.8	0.7×10^8	0.418	1.039

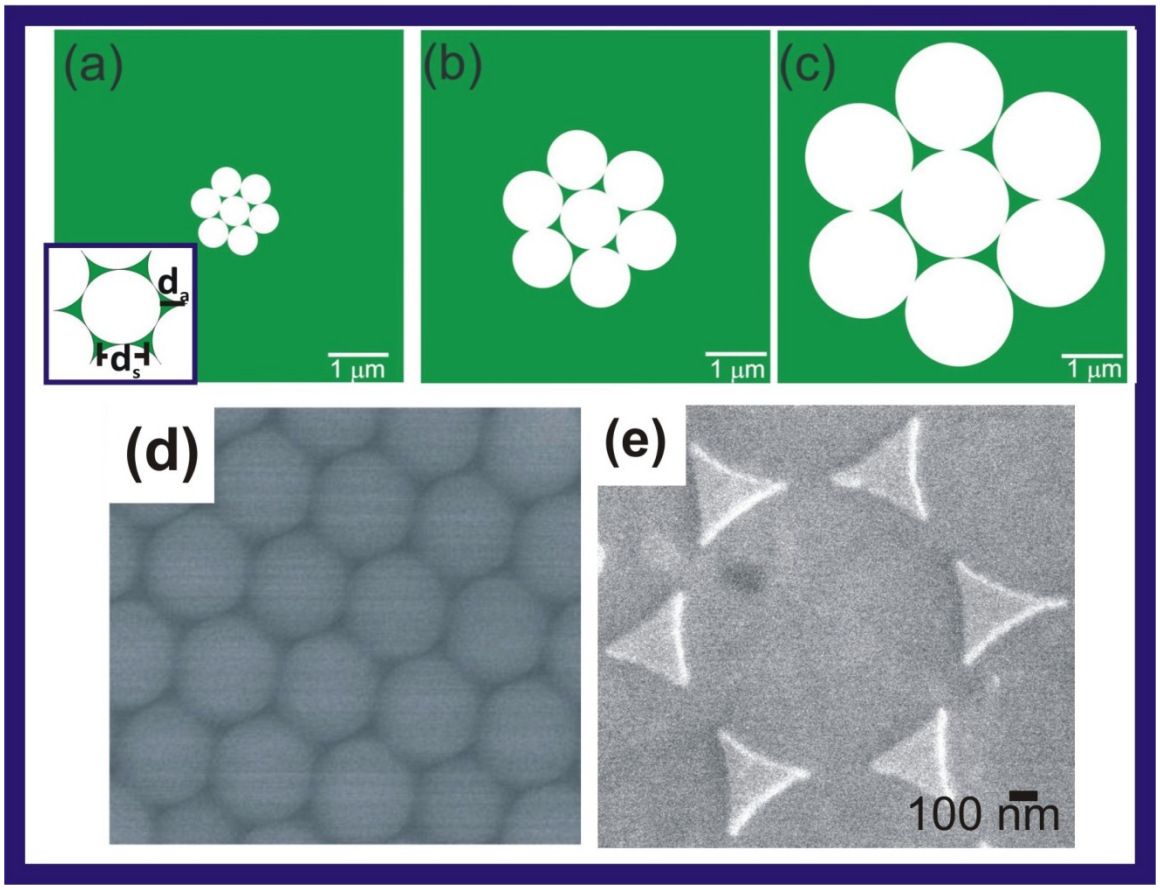

Figure 4.2: *Nanosphere lithography. (a-c) The schematic of the relative variation of catalyst size (d_a) and separation for the catalyst sites (d_s) formed by spheres of diameter 0.5, 1.0, and 1.8 μm, respectively. Inset in Fig. 4.2(a) depicts the definitions of the catalyst size (d_a) and the separation of the catalyst sites (d_s). (d) SEM image of hexagonal pattern formed by a monolayer of spheres with diameter 1.0 μm. (e) SEM image of a well-ordered hexagonal array of quasi-triangular Ni catalyst particles after Ni deposition and removal of 1.0 μm PS spheres.*

(b) Surface morphology analysis by scanning electron microscopy:

The mechanism of CNT growth by a PECVD can be understood as follows: The thermal treatment reduces the thin film or quasi-triangular particles of catalyst into spherical dots. The energy available from plasma generation and heating procedure

decomposes the carbon precursors on the outer surface of the catalyst particles. The carbon atoms diffuse through the catalyst particles and tubular structures are formed with a catalyst particle either at the base or tip [8]. The plasma also helps to etch amorphous carbon that may deposit on top of the Ni particles, thus providing a steady supply of carbon atoms at the surface of the Ni particle [41].

Figures 4.3(a-d) are the top view SEM images which show the distribution of the CNTs, whereas Figs. 4.3(e-h) offer a 45° tilt-view to show the alignment of individual CNTs. Compared to the high-density (HD) growth of CNTs on Ni catalyst film (note: without any catalyst pattern), in Fig 4.3(a), the CNTs synthesized with NSL patterned catalyst exhibit larger separation amongst each other, Fig. 4.3(b-d). A careful observation of Fig. 4.3(c-d) reveals the growth of multiple numbers of CNTs from a single catalyst island. Similar growth behavior has been previously reported by Lee *et al*. [42]. When the size of the catalyst dot increases beyond the critical size, a multiple number of CNTs will grow from a single catalyst dot. During the annealing of catalyst, the Ni film from a single dot disintegrates into a number of particles each of which acts as a nucleation site for CNT growth. Similar reports of multiple growths of CNTs from a single dot have been attributed to the low growth temperature of around 520 °C [43]. Different methods have been suggested to achieve the single growth of CNTs from a catalyst dot. For example, deposition of a thinner layer of Ni catalyst, using spheres of smaller diameters, using a double layer PS mask for the catalyst deposition, chemical etching etc. have been suggested as appropriate methods for the fabrication of a single CNT from a catalyst dot. There have been reports of slight distortion of the CNTs from the original catalyst pattern

because of the migration of catalyst dot owing to their weak adhesion to the buffer layer [42]. However, no such noticeable migration of CNTs was observed in our experiments. The tilted-views in Figs. 4.3(e-h) show the formation of vertically aligned CNTs. These CNTs have a length between 1-2 μm and diameter around 100 nm. The cluster of CNTs originating from a single catalyst dot has a smaller separation as compared to CNTs from the adjacent dots. The aspect-ratio of these CNTs synthesized with different densities has similar values. However, these CNTs are expected to exhibit different field emission properties as the result of the variable proximity between the adjacent CNTs. Compared to the high-density CNTs on Ni film (without any catalyst pattern), CNTs grown on patterned catalyst dots using 0.5 μm spheres are expected to show better field enhancement properties. A further decrease in the density of CNTs grown on patterned catalyst dots, using larger spheres might result in poor emission properties because of the presence of lower number of emitting sites. Hence, it is desirable to find the optimal density or separation of VACNTs (therefore optimal size of PS) to achieve the best field emission properties.

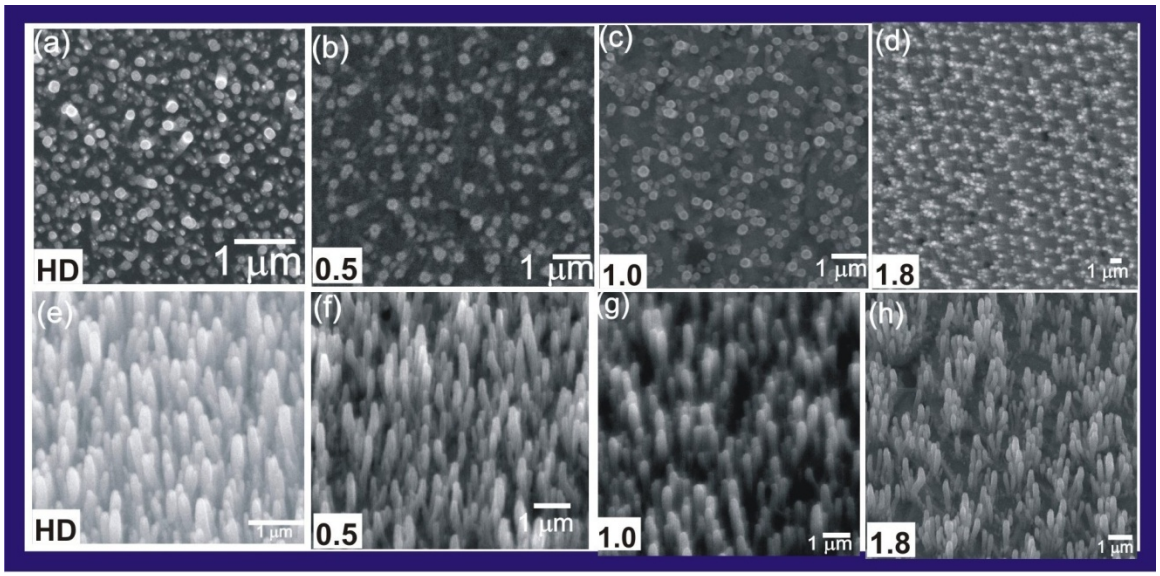

Figure 4.3: *Variations of densities of CNTs prepared without and with different size PS. (a-d) are the SEM top-views of the CNTs; (e-h) are the tilt-views of the CNTs. Figures (a) and (e) are high-density CNTs grown on Ni film deposited without any NSL pattern. The numbers in the box on other images represent the diameter of spheres, in micrometers, used during the NSL.*

(c) Structural analysis by transmission electron microscopy:

The tubular structure of CNTs was verified by TEM observation. Figure 4.4 (a) shows the TEM image of the top portion of CNTs synthesized on Ni catalyst film, and Figs. 4.4(b-d) are the TEM images of CNTs grown from Ni catalyst dots formed with NSL using spheres of diameter 0.5, 1.0, and 1.8 μm, respectively. We found that these multi-walled CNTs had a similar structure but slightly different lengths and diameter. The diameter of an individual CNT depends on the size of the catalyst fragment produced from a catalyst island. Smaller particles result in thinner tubes while bigger catalyst fragments result in thicker tubes. These CNTs have bamboo-like structures with a catalyst particle trapped at the tip suggesting a tip growth model. The graphitic planes in

the tube walls are not always parallel to the tube axis but are often twisted and broken; which is the characteristic of CNTs synthesized by PECVD process [44]. The inset of Fig. 4.4(a) shows a magnified view of a typical CNT which contains a Ni catalyst rod forming a core-shell like structure. The effect of extrusion induced by the compressive force of the graphene layers during the growth of CNTs results in the formation of these core-shell structures. The Ni catalyst particle melts during the growth and a section of it may get trapped half way up the tube. At nanoscale dimensions, the melting point of metals can be significantly lower than that of their bulk counterparts [45]. Similar phenomenon of the melting of Ni catalyst at temperatures far below the melting point of bulk Ni has been reported earlier [46]. The inset in Fig. 4.4(c) shows the HRTEM image of a section of graphitic layers with the separation of about 0.34 nm which correspond to the separation of lattice planes (002) of graphite. The inset in Fig 4.4(d) shows the interface between the graphitic planes of the CNT and the planes of the Ni core in a core-shell structure. The parallel graphitic planes that make up the CNT are seen on the left part of the image in light contrast. The catalyst particle also exhibits crystalline structure with atomic planes separated by 0.18 nm corresponding to the Ni (200) lattice planes.

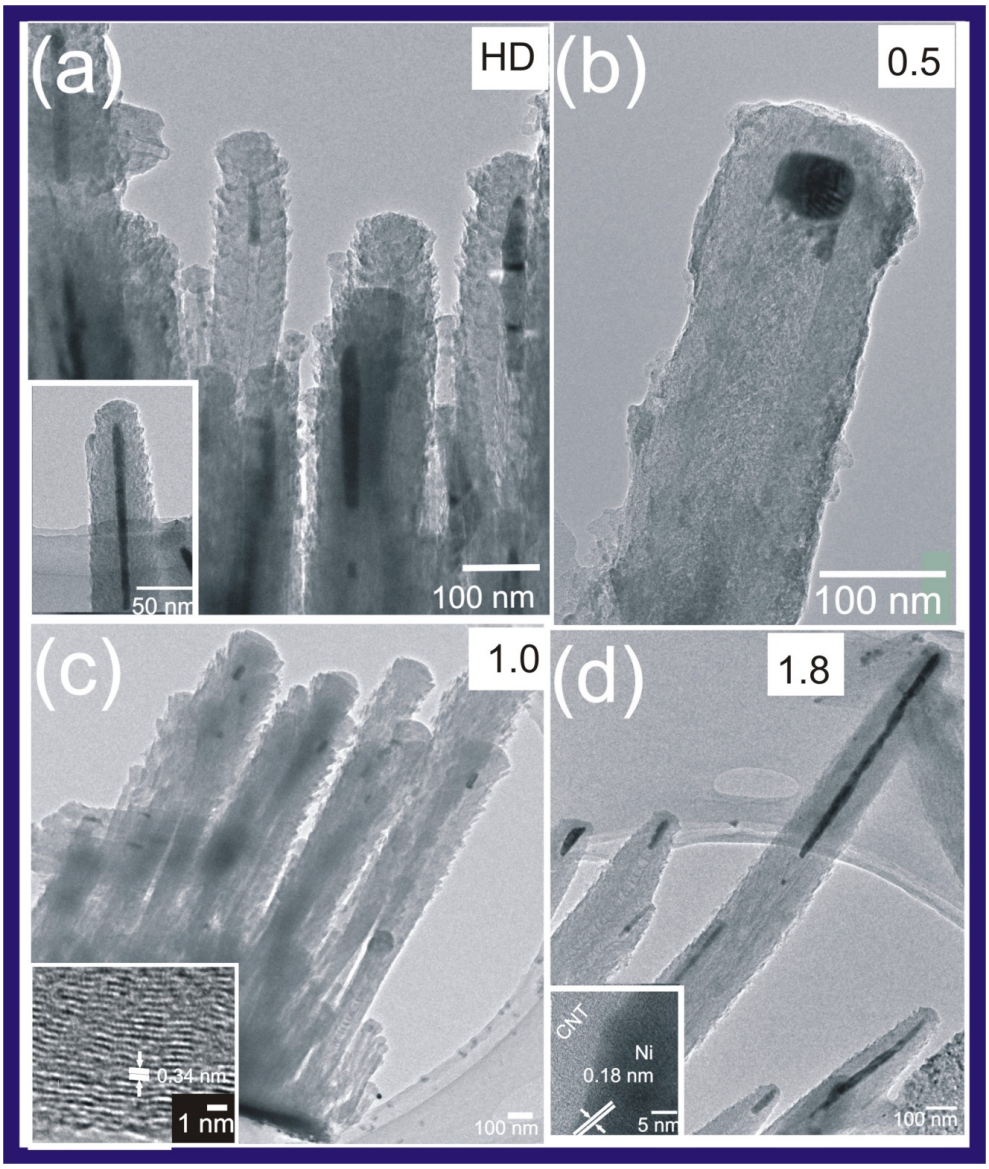

Figure 4.4: *TEM images of the CNTs. (a) TEM image of high density CNTs grown on Ni film catalyst. (b-d) TEM images of CNTs synthesized on Ni catalyst dots patterned using spheres of diameter 0.5, 1.0, and 1.8 μm, respectively. The inset in (a) shows a rod-like Ni catalyst inside a CNT that is forming a core-shell structure. The inset in (c) shows the lattice fringes of graphitic planes in a single CNT. The inset in (d) shows the interface between the CNT and the Ni catalyst trapped inside the CNT.*

(d) Electron field emission of CNT emitters with different densities:

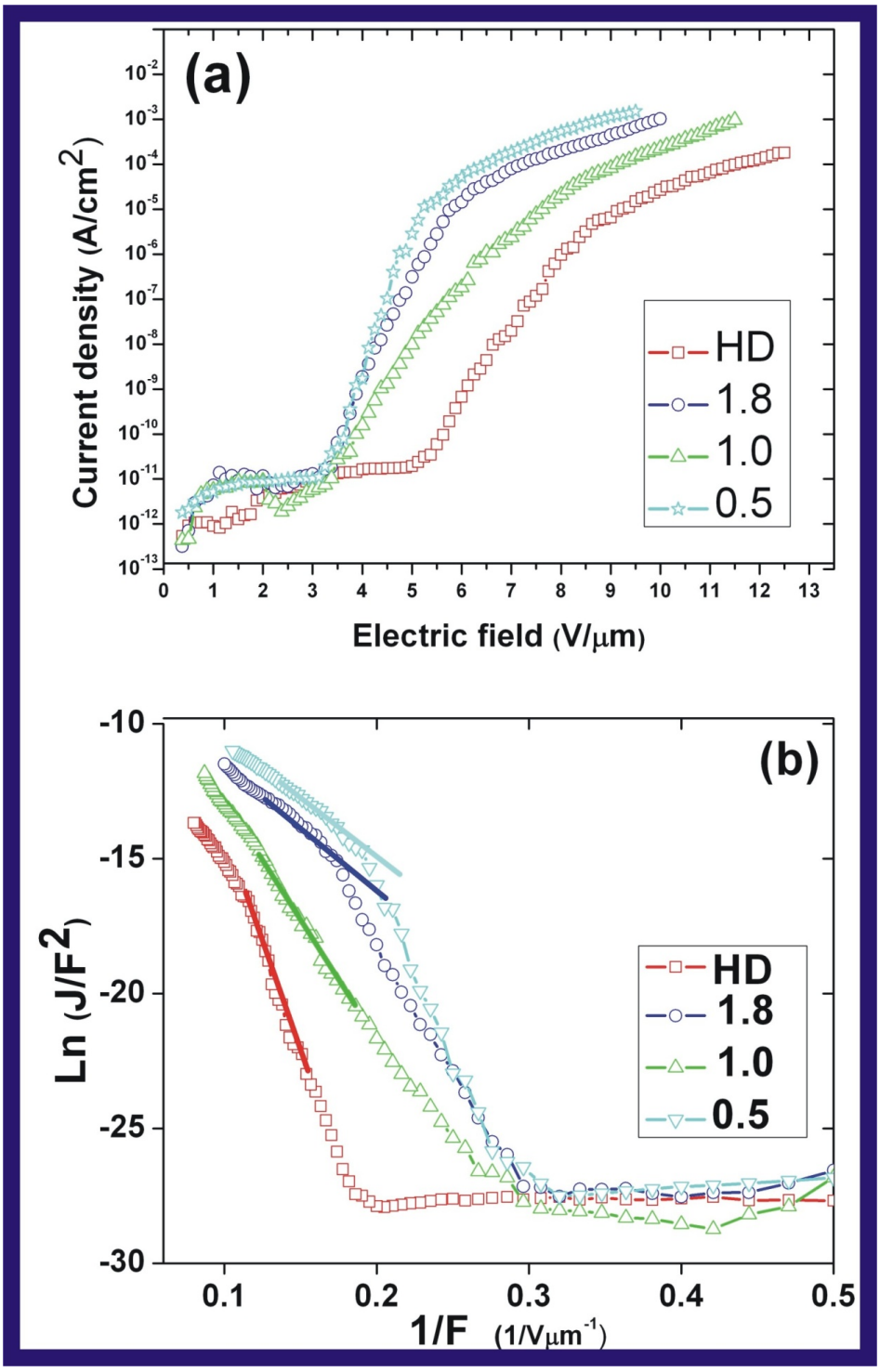

Figure 4.5: *Field emission properties of CNTs with different densities. (a) F-J plot (b) F-N plots.*

The electron field emission properties of CNT emitters with different densities were measured as described earlier in section 3.8. The field emission properties of the high density CNTs grown on Ni film and the low density CNTs grown on Ni dots patterned with the spheres of diameter 0.5, 1.0, and 1.8 μm are shown in Fig. 4.5. Figure 4.5(a) shows the current density versus the electric field (*F-J*) curves of the CNTs with four different densities. All CNTs demonstrated excellent field emission properties with high current density and long stability. We define the turn-on electric field ($E_{turn\text{-}on}$) as the electric field required to obtain the emission current density of 1 μA cm^{-2} [47]. Similarly, the threshold electric field (E_{th}) is defined as the electric field corresponding to the emission current density of 1 mA cm^{-2}. The numerical values of $E_{turn\text{-}on}$ and E_{th} for the four types of samples are presented in Table 4.2. The turn-on electric field for high-density CNTs was 7.96 V μm^{-1}. The turn-on field decreased to 4.71, 6.41, and 5.19 V μm^{-1} for CNTs grown on catalyst dots patterned by spheres of diameter 0.5, 1.0, and 1.8 μm, respectively. Also, the threshold electric fields for CNTs with catalyst patterned by spheres of diameter 0.5, 1.0, and 1.8 μm are 8.71, 11.48, and 9.89 V μm^{-1}, respectively. It is noteworthy that, for high-density CNTs, the emission current density of 1 mA cm^{-2} could not be achieved even after increasing the applied electric field to 13.5 V μm^{-1}. The lower values of turn-on field and threshold electric field clearly suggest that the low-density CNTs synthesized by the catalyst patterned by NSL are more favorable than the high-density growth for the optimum emission current. In the high density CNT arrays grown on Ni catalyst film, some of the emitted electrons will be trapped by the adjacent CNTs and only the CNTs emitted from the tip can contribute to the total current. There is a smaller probability of capturing emitted electrons in the case of low-density growth

than in the high-density growth. This will increase the flux of electrons reaching the anode. Hence, the CNTs synthesized on catalyst patterned by spheres of different diameters exhibit better field emission properties than CNTs synthesized on Ni film. The trapping of the electrons and screening of the electric field can be reduced in a low-density array of CNTs. The CNTs grown on catalyst patterned by NSL using spheres of 0.5 μm diameter had the lowest E_{th} and $E_{turn\text{-}on}$ among the low-density CNTs. The increase in total current despite the lower density indicates that an individual CNT emits more electrons when the CNTs are sparsely distributed. The further decrease in the site density of CNTs by using spheres of 1.0 μm diameter resulted in the reduction in emission current because of the presence of fewer numbers of CNTs. However, the CNTs grown from catalyst patterned by NSL using spheres of diameter 1.8 μm showed improved emission characteristics than those CNTs grown from catalyst patterned by NSL using spheres of diameter 1.0 μm. As evident from the SEM images, the CNTs grown from catalyst patterned by NSL using spheres of diameter 1.8 μm produces more CNTs from a single island as compared to CNTs grown from catalyst patterned by NSL using spheres of diameter 1.0 μm. The presence of a more number of CNTs within a single bundle contributes to the better performance of the emitters. Fuji *et al*. [48] performed a computer simulation to compare the resultant electric field from a CNT bundle and a flat film of CNTs. It was found that electric field of the flat film is constant all over the emitter surface, whereas the electric field of the bundle is significantly higher at the edge than at the center. Hence, the electric field is predominantly concentrated along the circumference of the bundle which results in more emission sites. Thus CNTs synthesized from catalyst patterned using spheres of diameter 1.8 μm exhibited better

emission current than the CNTs grown from catalyst patterned using spheres of diameter 1.0 μm because of the edge effect.

Table 4.2: Turn-on and threshold electrical fields of CNTs with different densities

	High density	0.5 μm	1.0 μm	1.8 μm
$E_{turn-on}$ (V μm^{-1})	7.96	4.71	6.41	5.19
E_{th} (V μm^{-1})	NA	8.71	11.48	9.89
Field enhancement factor (β)	460	1760	855	1680

Figure 4.5(b) shows the corresponding Fowler-Nordheim (F-N) plots for the CNTs with four different densities. The straight lines indicate the quantum mechanical tunneling characteristic of field electron emission. The field enhancement factor can also be calculated using the F-N equation: $J = (A\beta^2F^2/\phi) \exp [-B \phi^{3/2} / \beta F]$ where J is the emission current density, $A = 1.56\times10^{-6}$ AV^{-2} eV, $B = 6.83\times10^{9}$ $eV^{-3/2}$ Vm^{-1} [49], β is the field enhancement factor, ϕ is the work-function, and F is the applied electric field. Assuming the work function of the CNTs to be 5.0 eV [50], the field enhancement factor can be calculated from the slope of the F-N plot. It is reported that the work-function of CNTs reduces to values of 3.0 eV and 2.0 eV at higher applied fields of 10 V μm^{-1} and 14 Vμm^{-1}, respectively [51]. The work-function of CNTs also depends on the presence of amorphous carbon material on the surface, presence of open-ended tube or closed-ended tube, presence of catalyst particle on the tubes, defects and others. Here, in this study, we use $\phi = 5.0$ eV to make the comparison of the emission behavior of the various CNT

arrays easier and simple. Hence, we only consider the region where the work function does not decrease significantly below 5.0 eV and measure the slope of the straight lines as shown in Fig. 4.5(b), to make an estimation for the value of β. The field enhancement factors for high density CNTs and NSL patterned CNTs with spheres of diameter 0.5, 1.0, and 1.8 μm were 460, 1760, 855, and 1680, respectively. It is noteworthy that the experimental β is greater than geometrical β (the ratio of length to radius) of the CNTs by an order of magnitude. These large discrepancies between the β estimated from the F-N plots and geometrical β~50 indicate that there are other mechanisms, in addition to quantum tunneling, for the field emission process [44]. The field emission properties depend upon the morphology of CNTs, structure of CNTs emitter and the method employed to measure the emission current. The ohmic contact between the CNTs and the substrate along with the vertical alignment of CNTs play an important role in the field emission. During the process of field emission, the electrons should cross the interface between substrate and barrier layer, pass through CNTs, and finally emit into the vacuum. The contact resistance is lower for CNTs synthesized on conducting substrates than for the CNTs synthesized with buffer layer of SiO_2, the low contact resistance will assist the process of field emission. The presence of the buffer layer of Cr in our samples ensures a robust contact of CNTs with the substrate over an extended period of emission time. Further, the low contact resistance between CNTs and Cr facilitates the electron transfer from the substrate to the CNTs during the emission [52].

Figure 4.5(b) illustrates two distinct slopes on the F-N plots. The slope of F-N plots in the region of high electric field is lower as compared to the slope in the region of

low electric field. Similar behavior has been attributed to vacuum space charge effects, changes in local density of states at the emitter's tip, interaction among adjacent tubes, solid-state transport, and adsorption and desorption of gaseous species even at high vacuum as a result of emission-assisted surface reaction process [53]. Although, it has been demonstrated that Murphy and Good's theory better explains the emission phenomenon at high electric fields in the range of $10^{7\text{-}10}$ V/m and temperatures of 1000-5000 K [54-56], we estimate that F-N equation is still applicable to explain the field emission in these experiments as such local temperatures on the CNT tip might have not been achieved. In this notion, we believe that the localized tip-cooling during field emission is partially responsible to compensate for the Joule heating [57].

(e) Stability test for CNT emitters with different densities:

The stability of emission current is one of the most important parameters used to estimate the feasibility of CNT emitters for various application purposes. Figure 4.6 shows the field emission stability of emission current from CNTs with different densities during the stability test. The initial emission current was set at the maximum value for the particular sample and the applied voltage was kept constant for 10 h. Only a small degradation in the emission current was observed when the CNTs were subjected to such a stringent current over a long period of time. The critical current, which is the maximum current that a single nanotube can deliver from an individual CNT, increases with the diameter. The CNTs with diameters in the range of 5-20 nm have the critical current in the range of 2-15 μA while CNTs with diameters of about 30 nm deliver the current in the range of 40-250 μA [58]. Wei *et al*. performed in-situ TEM observation on the

degradation of a CNT emitter and observed that CNTs suffered abrupt breaking at the point where the temperature reached a maximum value [59]. The CNTs in the present work have diameters in the range of 80-100 nm and are expected to withstand greater current preventing thermal degradation. The high thermal conductivity of both the CNTs and the Cu substrate allows an unobstructed transfer of heat preventing the occurrence of high temperatures and destruction of the emitters. The conduction of heat will minimize the degradation of CNT emitters subjected to withstand the high temperature caused by Joule heating. Pandey *et al*. have simulated the electrical field for arrays having bundles of CNTs at different sites [60]. The maximum local electric field at the bundle is two-order of magnitude lower than those for rectangular arrays of CNTs. The lowered electric field will result in lower thermal and mechanical stress introduced on CNT bundles. We attribute the high field emission stability of our samples to the strong adhesion of CNTs with the Cu substrate, higher critical current and lowered stress. CNTs synthesized with the catalyst patterned by spheres of diameter of 1.8 μm exhibited a sharper decline in emission current over the test period as compared to other samples. The individual CNTs on samples with catalyst patterned by spheres of diameter 1.8 μm were liable to produce currents of higher magnitude, because of a lower density than the CNTs on other samples, and were prone to quicker degradation.

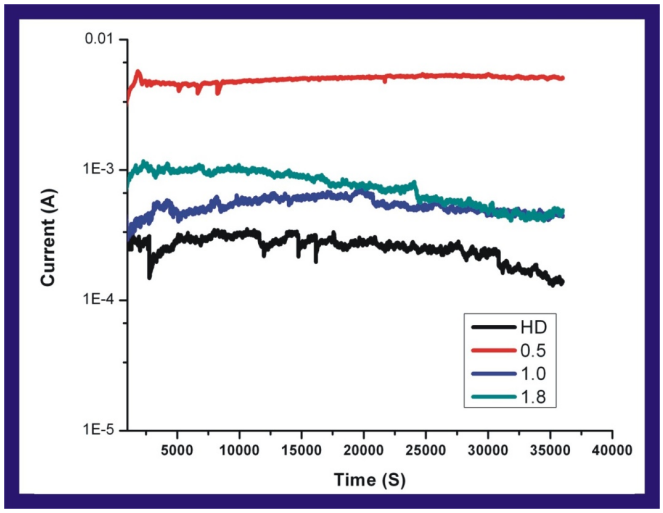

Figure 4.6: *Field emission stability of CNT arrays with different densities.*

4.3.2 Effects of plasma treatment on the emission current of CNT emitters

The evolution of the structure of the CNT emitters after plasma treatment and the effect of plasma treatment on the emission current of the CNT emitters has been discussed in the following section.

(a) SEM observation of the effect of plasma treatment on the structure of the CNT emitters:

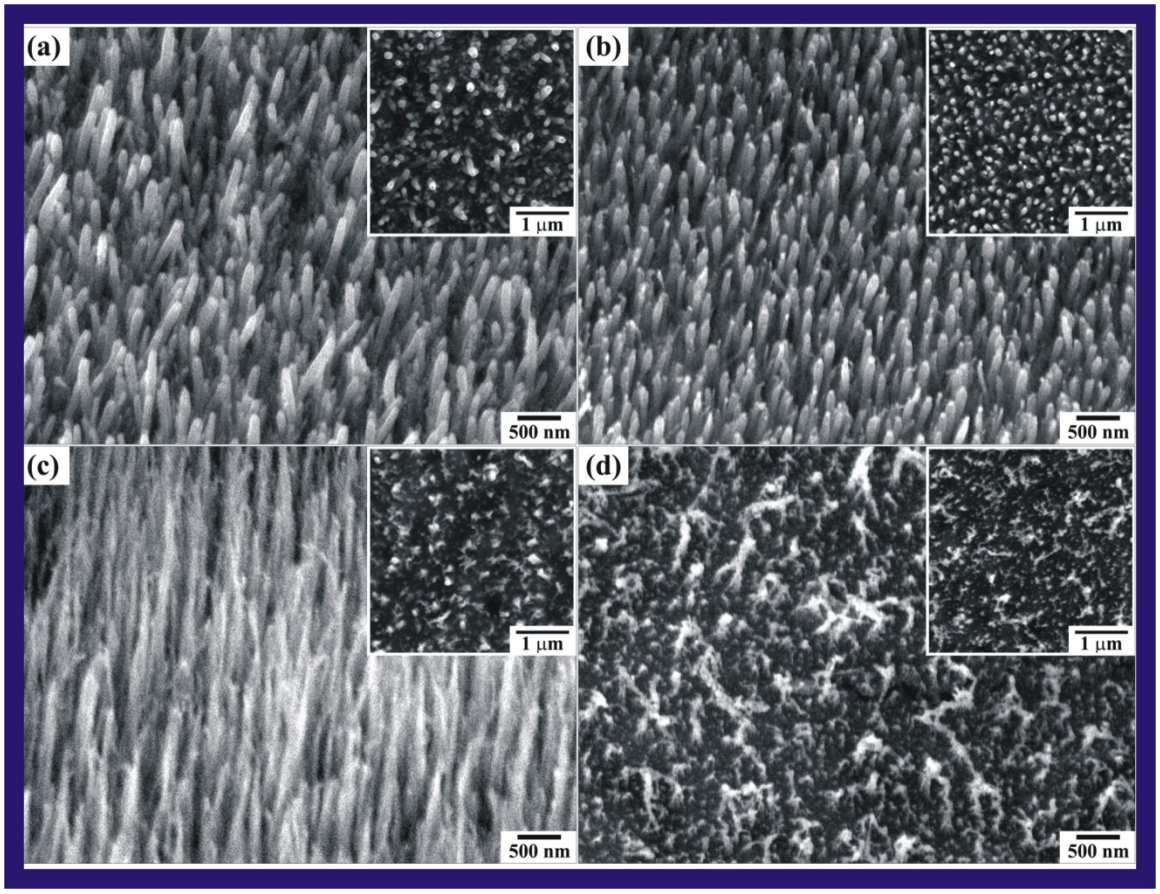

Figure 4.7: *SEM images of the CNTs before and after NH_3 plasma treatment. (a) P-0.0 min, (b) P-0.5 min, (c) P-1.0 min, and (d) P-2.0 min. The insets show the corresponding top-view images.*

Typical SEM images of the CNTs before and after NH_3 plasma treatment are shown in Fig. 4.7. Before plasma treatment, sample P-0.0min showed structurally robust vertically aligned CNTs, as shown in Fig. 4.7(a). The as-grown CNTs showed a cylindrical structure with a large diameter of ~80 nm and length of 1-1.5 μm. The length was not highly uniform and some longer CNTs protruded. After 0.5 min treatment, the

CNTs became thinner due to the etching effect of the plasma as shown in Fig. 4.7(b). The plasma treatment also resulted in sharp tips on the CNTs compared with the pristine CNTs. In addition, the longer CNTs were cut by the plasma, resulting in a uniform length after the plasma etching. The etching effect became more significant after 1.0 min treatment. As shown in Fig. 4.7(c), the CNTs showed a tapered structure with a very sharp tip compared with the pristine CNTs. The tapered structure is favorable for the field emission. These thinner tips easily touched each other and as a consequence seemed to form a cluster structure. It is very clearly shown in the inset of Fig. 4.7(c) that the tips of the CNTs after 1.0 min treatment were bundled together. Each bundle consisted of several CNTs with joined tips. Therefore the inter-tip distance increased as compared with the samples P-0.0min and P-0.5min, as shown in the insets of Fig. 4.7(a-b). The increase in the inter-tip distance will effectively alleviate the screening effect in the CNT film, resulting in the enhanced field emission properties [61]. However, after 2.0 min plasma treatment, the morphology of the CNTs was totally different from the previous samples, as shown in Fig. 4.7(d). The longer duration of plasma treatment caused a very severe damage to the CNTs. The CNTs were badly destroyed and so was the alignment, as shown in the inset of Fig. 4.7(d). It was very difficult to find CNTs with good alignment under SEM observation. Accordingly, the field emission performance should greatly deteriorate.

(b) TEM observation of the effect of plasma treatment on the structure of the CNT emitters:

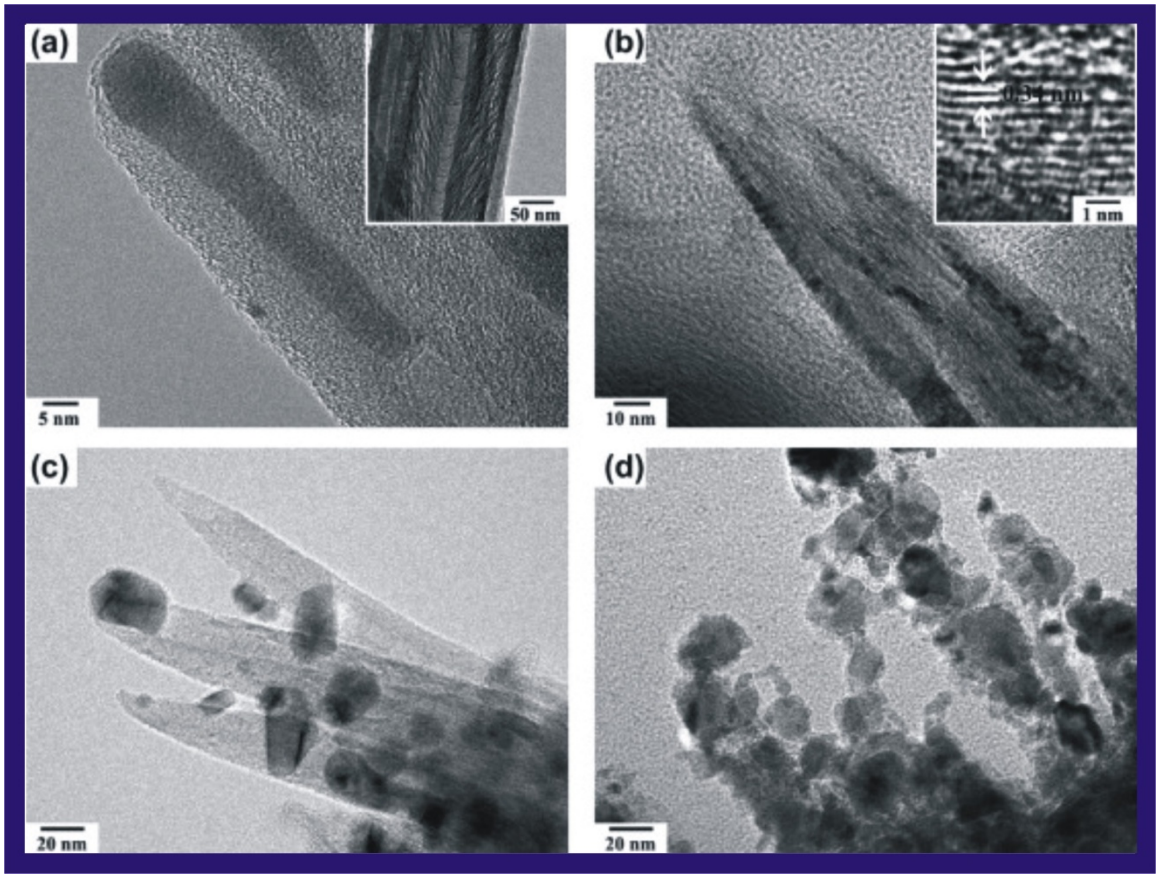

Figure 4.8: *TEM images of the CNTs before and after NH_3 plasma treatment. (a) P-0.0 min, (b) P-0.5 min, (c) P-1.0 min, and (d) P-2.0 min. The inset in (a) shows a bamboo-like structure. The inset in (b) shows the lattice fringes of graphitic planes in a single CNT.*

Transmission electron microscopy observations were carried out to examine the effect of plasma treatment on the microstructures of CNTs, Fig. 4.8. Without the plasma treatment, the CNTs showed a cylindrical structure with good crystallinity, as shown in Fig. 4.8(a). All the CNTs had closed tips with a catalyst particle at the tip. The diameters of the CNTs were around 80 nm. After 0.5 min treatment, the CNTs became thinner

because of the plasma etching effect with a stem diameter of 50 nm, as shown in Fig. 4.8(b). The etching effect was more significant at the tip, resulting in a sharp tip with a diameter of ~20 nm. Specifically, the graphene layers at the tip were severely damaged. As a result, the CNTs showed an open tip with some damage on the wall. The etching effect became more significant while continuing the plasma treatment and the CNTs completely changed from the cylindrical structure to a tapered structure with a very sharp tip. The plasma inevitably induced significant damage and structural defects to the CNTs. All the results were in good agreement with the results of SEM observation and the Raman spectroscopic analysis.

(c) Raman spectroscopic analysis of the effect of plasma treatment on the structure of CNT emitters:

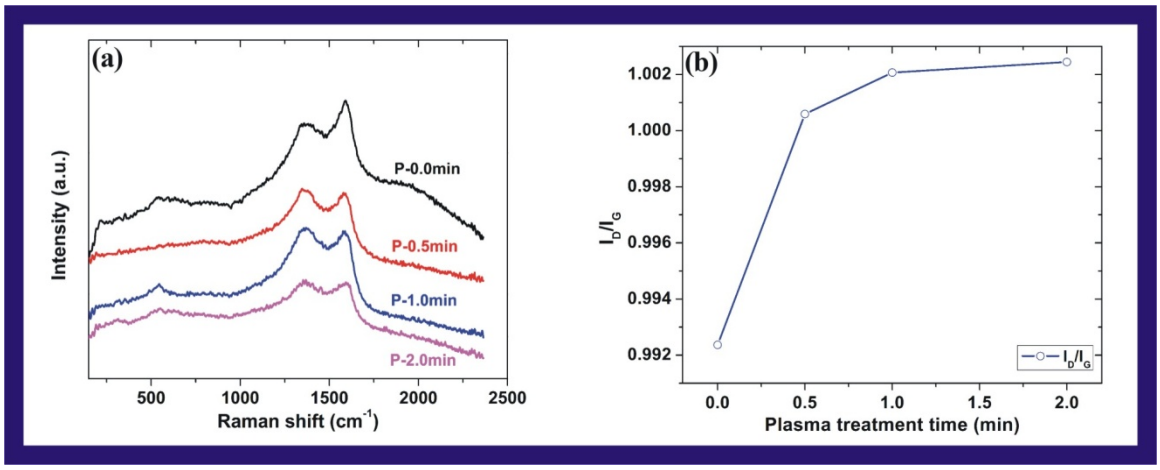

Figure 4.9: *Raman spectroscopic analysis of CNTs. (a) Raman spectra of the CNTs before and after NH_3 plasma treatment for different durations. (b) Corresponding I_D/I_G ratios.*

To further understand the effect of NH_3 plasma treatment on the field emission properties of CNTs, Raman spectroscopy was carried out to analyze the microstructure

and defect density of the samples. Raman spectra of the CNTs before and after the plasma treatment are shown in Fig. 4.9(a). The I_D/I_G ratio, which gives the indication of the level of disorder degree in the graphite sheets, is shown in Fig. 4.9(b) for CNTs with different plasma treatment time. It can be seen that the I_D/I_G ratio increased with the plasma treatment time increasing, indicating that the plasma treatment can result in significant structural defects to the CNTs.

(d) Effect of plasma treatment on the electron field emission of CNT emitters:

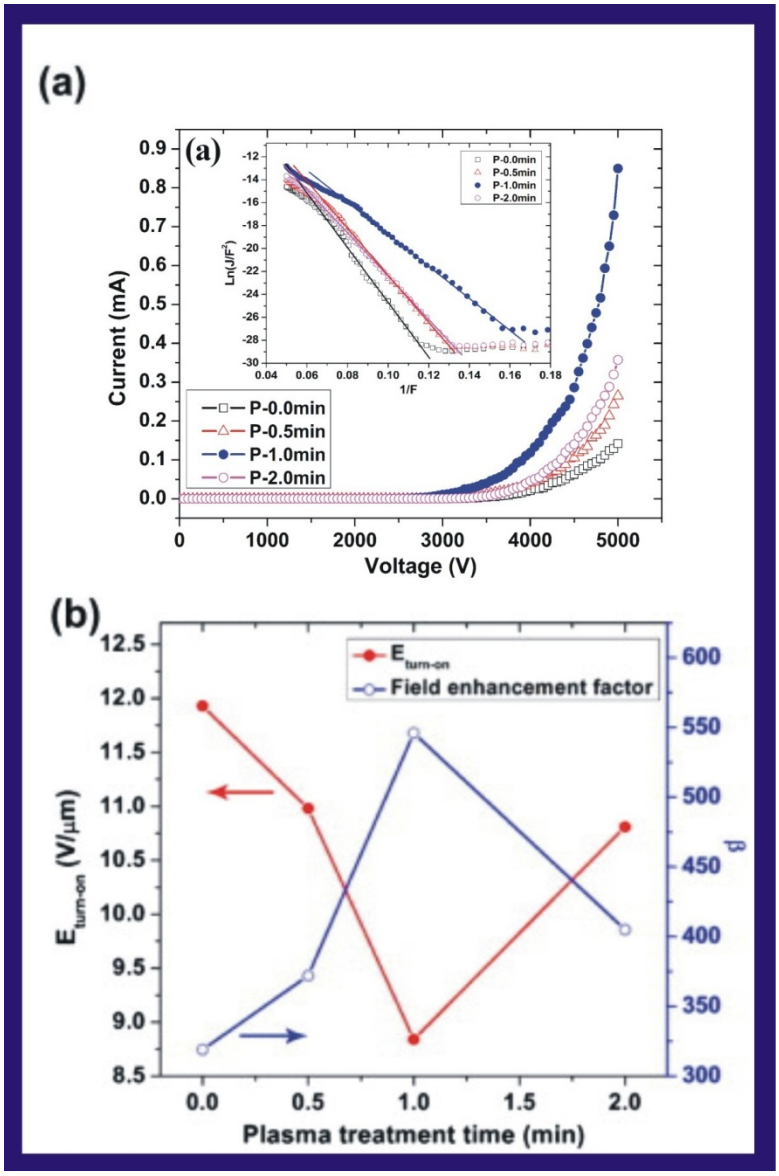

Figure 4.10*: Field emission characteristics of the CNTs before and after NH_3 plasma treatment. (a) I–V curves. The inset shows the corresponding F-N plots. (b) Field enhancement factor (β), $E_{turn\text{-}on}$ of CNTs according to NH_3 plasma treatment time.*

Figure 4.10(a) shows the field emission characteristics of the CNT emitters made by the four kinds of CNTs. The CNTs demonstrated different field emission properties

according to different plasma treatment durations as shown in Fig. 4.10(a). The $E_{turn\text{-}on}$ for sample P-0.0min was 11.93 V/μm. After the plasma treatment, the turn-on electric field decreased according to the plasma treatment durations. More specifically, the $E_{turn\text{-}on}$ for samples P-0.5min and P-1.0min were 10.98 and 8.84 V/μm, respectively. However, after 2 min plasma treatment, the sample showed a slightly increased turn-on electric field, 10.81 V/μm, compared with the sample after 1 min treatment. The sample P-1.0min showed the lowest turn-on electric field among the four kinds of CNTs. In addition, the sample P-1.0min also showed the highest emission current of 0.85 mA among the four kinds of CNTs. Both the lowest turn-on electric field and the highest emission current suggest that 1.0 min NH_3 plasma treatment can greatly improve the field emission performance of CNTs.

Several papers have reported on the Joule's heating effect on the CNTs during electron emission and claimed that the temperature of individual CNT structure can easily go above 1000 K at an emission current level of l μA/tube [24, 57]. It has been reported that the high temperature might influence the emission regime from a Fowler–Nordheim type of emission towards a thermo-field emission where tip temperature plays an important role [56, 57, 62]. We estimated the current per tube in our research. Considering Fig. 4.7(a) as an example, the CNT density was estimated to be about 14 tubes/μm^2. This value was obtained upon considering the screening effect between the CNTs with different heights, namely, the short CNTs will not contribute significantly to the total field emission current [24]. The maximum emission current density of the P-0.0 min sample was about 0.18 mA/cm^2. As a result, the current per tube was around $1.3\times10^{-}$

^{4} nA. This value is far below 300 nA, which is the typical threshold for possible emission degradation of the tubes [63]. We think that high temperatures on the CNT tip might have not been achieved. Therefore, the F–N equation is still applicable in the present experiment.

The inset in Fig. 4.10(a) shows the corresponding F-N plots for the four kinds of CNT emitters. The field enhancement factors for samples P-0.0min, P-0.5min, P-1.0min, and P-2.0min were 319, 372, 546, and 405, respectively. We note that the field enhancement factor increased as the plasma treatment time increased and the CNTs with 1 min plasma treatment showed the highest value of the field enhancement factor. Figure 4.10(b) presents the graph of field enhancement factors and $E_{turn\text{-}on}$ according to the plasma treatment time. With the plasma treatment less than 2 min, the field enhancement factor increased and the turn-on electric field decreased with the plasma treatment duration, indicating enhanced field emission performance of the CNTs. However, after 2 min plasma treatment, the CNTs demonstrated a decreased field enhancement factor and an increased turn-on electric field, indicating that the CNTs were damaged severely and showed a degraded field emission performance. Lee *et al*. studied the field emission characteristics of CNTs after Ar plasma treatment and found that the work function slightly increased from 4.57 eV to 4.87 eV (about 6% increase) after 3 min of plasma treatment [34]. If we assume that the work function changed about 6% for samples P-0.0 min and P-1.0 min (i.e. the sample P-0.0 min has a work function of 4.7 eV and the sample P- 1.0 min has a work function of 5 eV), the enhancement factor will be 291 for sample P-0.0 min and 546 for sample P-1.0 min corresponding to an increase of 88% in

the enhancement factor. Using the work function of 5.0 eV, the calculated enhancement factor is 319 for sample P-0.0 min and 546 for sample P-1.0 min, corresponding to an increase of 71% in the enhancement factor. Comparing the increase of the enhancement factor (88% and 71%) obtained using different work functions, it is clear that the assumption of the work function of 5.0 eV in this work gave reasonable values for the enhancement factors for samples after different plasma treatment. Fig. 4.10(b) shows that the enhancement factor increased at first and then decreased as the plasma treatment time increased which was consistent with the results of SEM and TEM observations. Previous studies investigated the relationship between the field enhancement factor, the aspect ratio of CNT structures, and the spacing between CNT structures [24, 64]. A more accurate expression for the field enhancement factor was considered as $\beta = 1.2[2.15+h/r]^{0.9}$ with large aspect ratios leading to greater field enhancement factor [64]. Plasma treatment made the CNTs tapered and increased the aspect ratio since the reduced tip diameter can be regarded as the effective diameter. As a result, the field enhancement factor increased. In addition, Dionne *et al*. concluded that larger field enhancement factor values can be obtained if the spacing between two tubes is greater than the sum of their heights ($\Delta x > h_1 + h_2$), whereas, significant screening effects will reduce the field enhancement factor if the spacing between the two tubes is equal to or smaller than the sum of their heights ($\Delta x \leq h_1 + h_2$) [24]. Therefore, the increased intertip distance after plasma treatment resulted in the lowered screening effect and consequently an increased field enhancement factor. It is obvious that the 1 min plasma treatment can greatly improve the field emission performance of the CNTs. The tapered CNT structure, the

clustered CNT tips, and the increased inter-tip distance extremely strengthened the field emission properties of the CNTs.

(e) Effect of plasma treatment on the field emission stability of the CNT emitters:

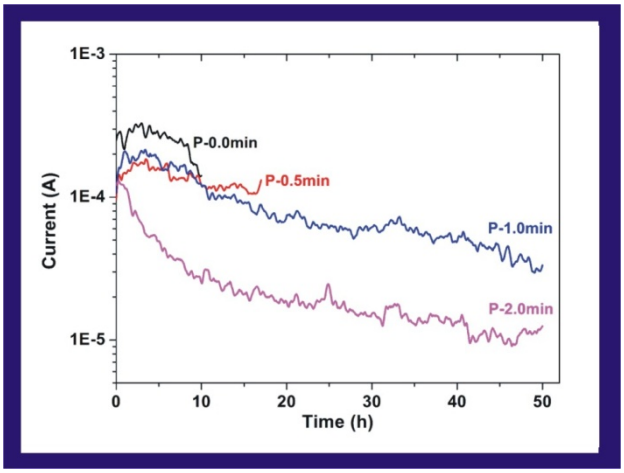

Figure 4.11: *Field emission stability of the CNTs before and after NH_3 plasma treatment.*

We also evaluated the emission current stability of the CNTs before and after NH_3 plasma treatment as shown in Fig. 4.11. The initial emission current was around 0.25 mA and then the applied voltage was kept constant for 10 h or longer. The initial emission current density was about 0.3 mA/cm^2, which is a relatively severe condition to visualize current degradation vividly within a relatively short time. Among the four kinds of CNTs, the sample P-1.0 min demonstrated excellent field emission stability over 50 h even though the emission current still decreased gradually.

The morphology of CNTs can significantly affect their field emission properties. Generally, the field enhancement factor is mainly related to the aspect ratio of the CNT [65]. The thick diameter and the short length may result in a high turn-on electric field

because of the small field enhancement factor. After the NH_3 plasma treatment, the CNTs changed from the thick cylindrical structure to the thin tapered structure. As a result, the field enhancement factor increased from 319 to 546 and the turn-on electric field decreased from 11.93 V/μm to 8.84 V/μm. In addition, the tips of the CNTs were opened by the plasma treatment, and a high density of structural defects was introduced into the CNTs. Both the open-ended tips and structural defects are regarded as one of the possible factors for the improvement on field emission properties of CNTs [66, 67]. Moreover, it's well known that the screening effect in the CNT film can greatly reduce the field emission performance of CNTs [61, 68]. From the top view of the 1.0 min plasma treated sample, the much thinner tips of the CNTs easily touched each other to form clusters and, as a consequence, the inter-tip distance became a slightly bigger compared with the untreated sample. Therefore, the screening effect will be effectively alleviated.

(f) XPS studies on the chemical structure of the CNT emitters:

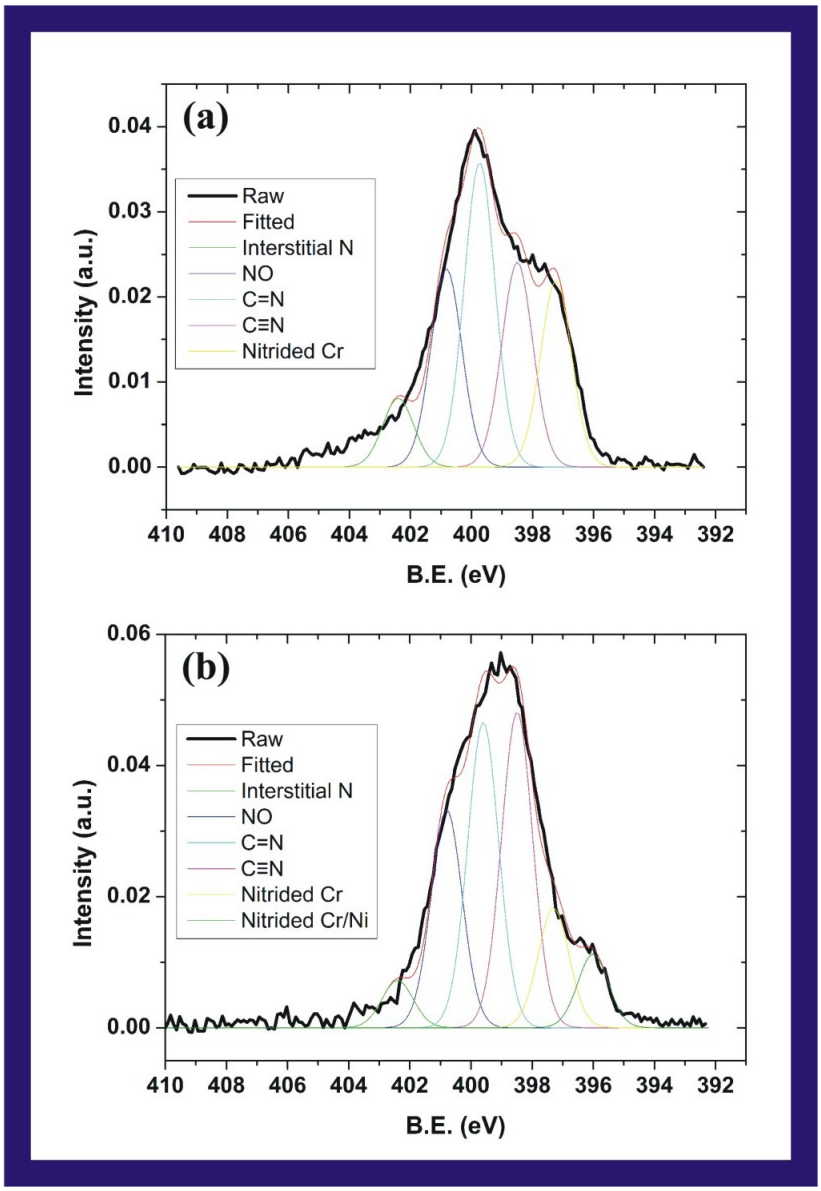

Figure 4.12: *XPS spectra from N 1s core level of the CNTs before and after NH_3 plasma treatment: (a) P-0.0 min, and (b) P-0.5 min.*

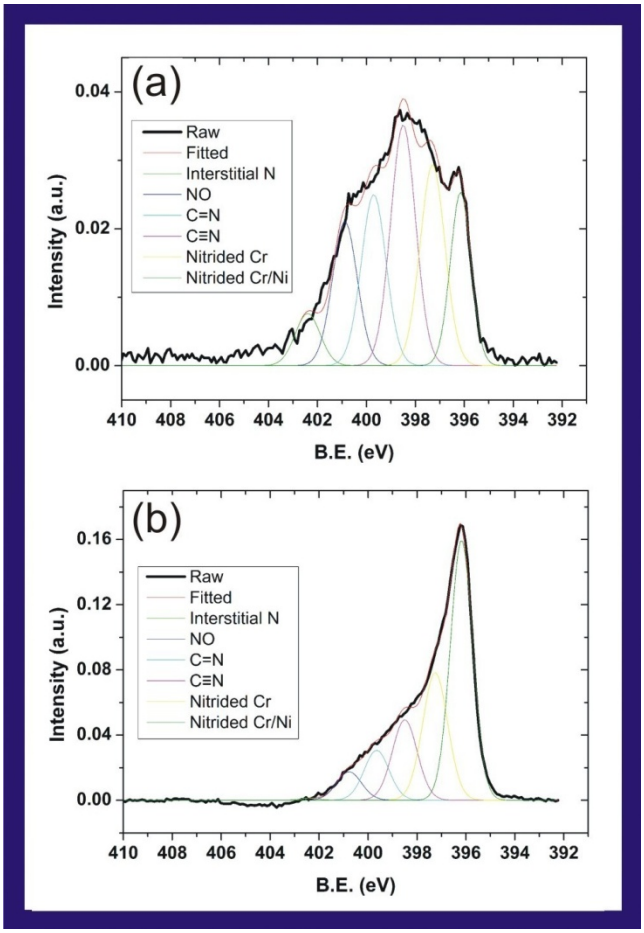

Figure 4.13: *XPS spectra from N 1s core level of the CNTs after NH_3 plasma treatment: (a) P-1.0 min, and (b) P-2.0 min.*

It is suggested that NH_3 plasma treatment not only induces structural defects but also creates doping effects. The XPS measurements were carried out to analyze the CNTs. The XPS spectra from N 1s core level of the CNTs before and after NH_3 plasma treatment are shown in Fig. 4.12 and 4.13. The spectra can be fitted with component peaks labeled N1, N2, N3, N4, N5, and N6 at 402.5, 400.8, 399.7, 398.6, 397.2, and 396.1 eV, respectively. The values of the full width at half maxima of each peak were about 0.9–1.2 eV, which were in agreement with the previous report [69]. The peaks of

N2, N3 and N4 corresponded to NO, C=N (sp^2 bonding), and C≡N (sp^3 bonding), respectively [69]. The high binding energy N1 peak was attributed to interstitial N [32]. The two low binding energy peaks of N5, and N6 were attributed to Cr_2N [70], and CrN [71], respectively. The intensities of these two peaks increased dramatically, especially after 2 min plasma treatment (not shown here). We can also confirm the chromium nitrides based on the structure change observed under SEM, showing that CNTs were badly destroyed so that the substrate was exposed. Considering the growth in this work followed the tip growth mode, many Ni catalyst nanoparticles were encapsulated in the CNTs. Therefore, the chromium nitrides formed on the substrate contributed dominantly to the XPS spectra as increasing the plasma treatment time. From the XPS spectra, we have confirmed that nitrogen has been doped into the CNTs even for the untreated CNTs, since we used NH_3 plasma during growth. Fig. 4.14 shows the area fraction of CN bonding (N3 and N4 peaks) with respect to the full N 1s spectra for different NH_3 plasma treatment durations. The area fraction reflects the number of CN bonding (N3 and N4 peaks) in the full N 1s spectra. Thus, the number of CN bonding increased at first and then decreased, indicating the doping effect changed along with NH_3 plasma treatment time. The number of CN bonding peaked at 0.5 min NH_3 plasma treatment. Longer plasma treatment time resulted in lower area fraction of CN bonding. It has been shown that nitrogen doping can improve the field emission performance of CNTs [72]. Although 0.5 min NH_3 plasma treatment showed the highest area fraction of CN bonding, NH_3 plasma treatment after 1 min demonstrated the best field emission performance. We suggest that the little difference is mainly attributed to the morphology change. The morphology change played a dominant role in field emission in this work. On the basis of

above viewpoints, the NH_3 plasma treatment could greatly improve the field emission performance of the CNTs grown on a Cu substrate.

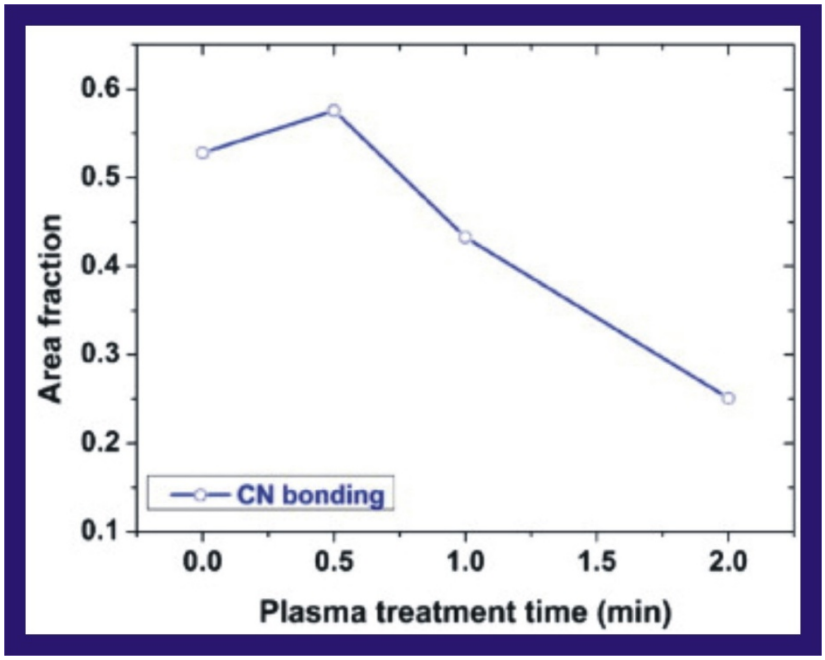

Figure 4.14: *Area fraction of CN bonding according to NH_3 plasma treatment time.*

4.3.3 Effects of CNT emitter geometry on their emission currents

The effects of CNT emitter geometry on the emission currents have been investigated and presented in detail in the following sections. The structure of the CNT point emitters has also been analyzed using scanning and transmission electron microscopy.

(a) SEM analysis of the point emitters:

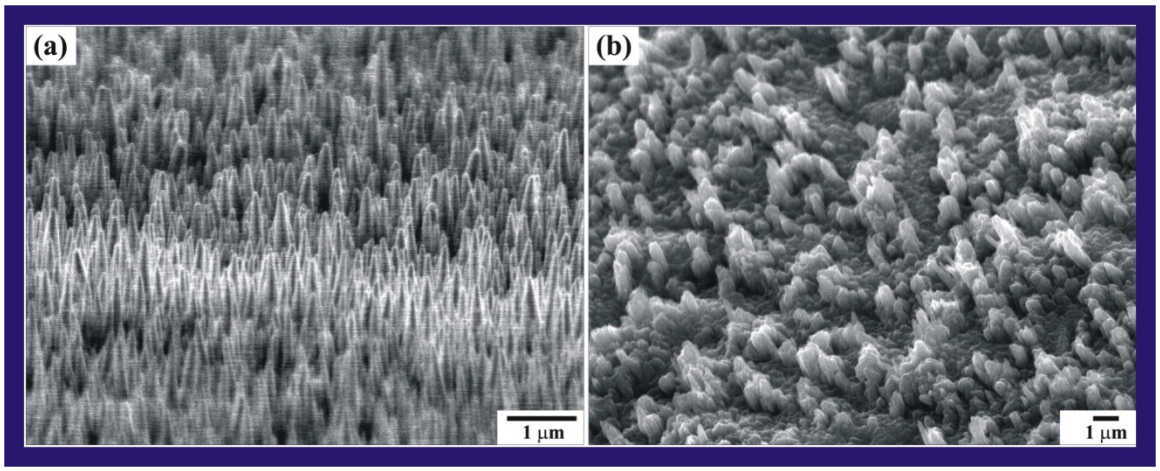

Figure 4.15: *SEM images of the two kinds of point emitters. (a) The F-tip emitter. (b) The S-tip emitter.*

The CNT morphologies of the two kinds of point emitters are shown in Fig. 4.15. Both of the CNTs were synthesized under identical conditions. However, the two kinds of point emitters showed quite different morphologies. The CNTs of the F-tip emitter showed a tapered shape with good vertical alignment, as shown in Fig. 4.15(a). The length of the CNTs was about 1.5 μm. The F-tip emitter consisted of a very high density aligned CNTs. However, the CNTs of the S-tip emitter demonstrated remarkably different structure. As shown in Fig. 4.15(b), the CNTs of the S-tip emitter showed a cylindrical stem and a coarse tip. The CNTs of the S-tip emitter had a short length in the range of 0.7–1.0 μm and showed a fairly low density as compared with that of the F-tip emitter. The low density of CNTs may result in good field emission as a consequence of the reduction of the screening effect [24].

Another obvious feature of the CNTs of the S-tip emitter is that they tend to grow connected to form bundles. The difference of morphologies between the two kinds of

point emitters can be attributed to the difference of electric field distribution during the PECVD growth because of the shape difference between the F-tip and the S-tip. The S-tip results in higher electric field gradient around the tip. As a result, some of the Ni catalyst particles might be destroyed or etched away by the plasma. This contributes to the low density of CNTs on the S-tip as compared to the high density on the F-tip.

(b) TEM analysis of the point emitters:

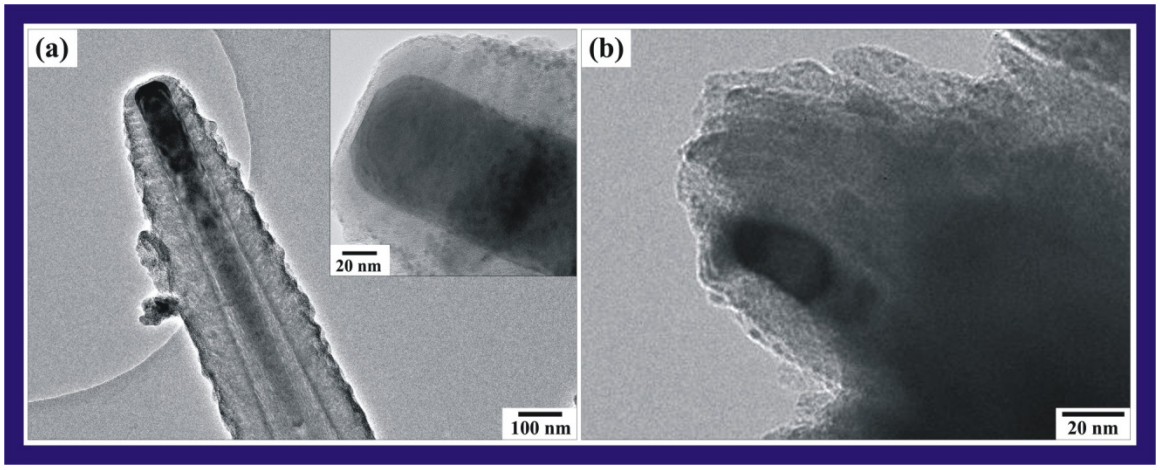

Figure 4.16: *TEM images of the two kinds of point emitters. (a) The F-tip emitter. (b) The S-tip emitter.*

Figure 4.16(a) shows a low magnification TEM image of the dispersed CNTs from the F-tip emitter. The CNTs displayed a multi-walled bamboo-liked structure. A catalyst particle was encapsulated inside the CNT tip, indicating the growth of the CNTs followed the tip growth model. The CNT had a large diameter of 110–140 nm at the tip and around 300 nm at the stem. High resolution TEM image indicated the CNT showed well-graphitized outer walls whereas the inner walls showed a bamboo-liked structure. Some amorphous carbon materials were found on the surface of the CNTs and might be produced during the TEM sample preparation. The inset in Fig. 4.16(a) shows a high

magnification TEM image of the tip of a CNT, revealing the highly ordered crystalline structures of both the carbon layers and the encapsulated catalyst particle. TEM examination indicated that the CNT of the S-tip have a diameter of around 100 nm, as shown in Fig. 4.16(b). However, it is very difficult to get a clear TEM image for a single CNT on the S-tip emitter because the CNTs are often connected together. Even though it is hard to know the crystallinity of the CNTs through TEM images, it is speculated that the CNTs of the S-tip emitter also had highly graphitized structures because the emitter demonstrated excellent field emission characteristics and good stability (more discussions to follow).

(c) Electron field emission of the point emitters:

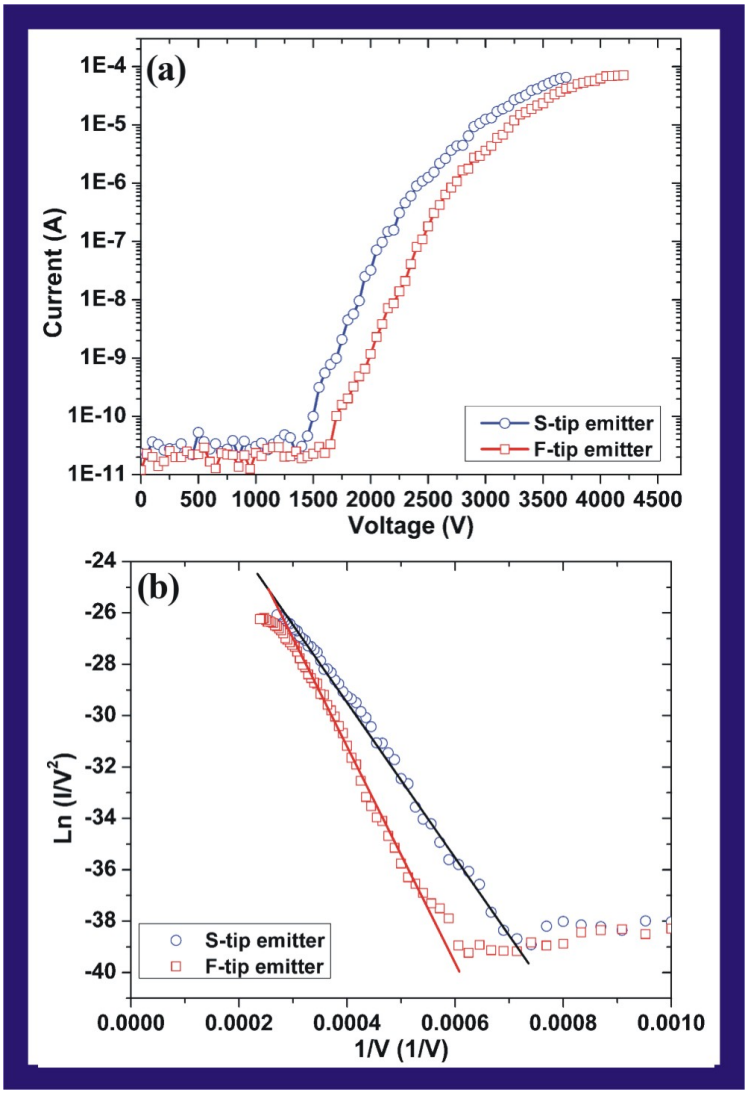

Figure 4.17: *Field emission characteristics of the two kinds of point emitters. (a) I–V curves. (b) The corresponding F–N plots.*

The field emission characteristics of the two kinds of CNT point emitters are shown in Fig. 4.17. I–V curves of both CNT point emitters demonstrated excellent field emission properties regardless of the shape of the tip of the Cu wires, Fig. 4.17(a). We tested both the F-tip and S-tip emitters before CNT growth and could not get any

emission current from either of them even when the applied voltage was increased to 5000 V. Therefore, we claimed that the excellent field emission performance was attributed to the CNTs grown on both tips. We defined the turn-on voltage as the applied voltage to obtain an emission current of 0.1 μA. The F-tip emitter showed a turn-on voltage of about 2450 V. The S-tip emitter demonstrated a lower turn-on voltage of 2100 V compared with the F-tip emitter, indicating that the S-tip emitter had a better field emission performance than the F-tip emitter. In addition, the F-tip emitter reached the highest emission current of 70 μA at an applied voltage of 4200 V. On the contrary, the S-tip emitter obtained the highest emission current of 65 μA at 3700 V. These emission magnitudes of current are good enough for practical applications.

The straight lines in the F-N plot shows the electron emission from these CNT point emitters is a quantum mechanical tunneling process. Assuming the work function of the CNTs to be 5.0 eV, the estimated field enhancement factors of the F-tip and S-tip emitters from the F-N plots are 907 and 1264, respectively.

(d) Electron field emission stability test of the point emitters:

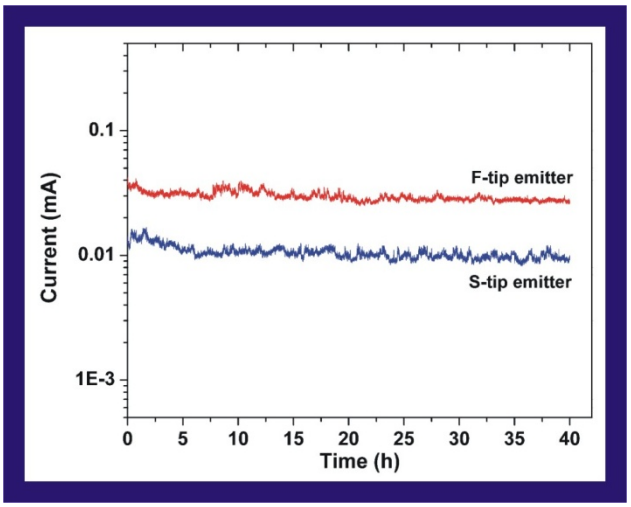

Figure 4.18: *Field emission stability of the two kinds of point emitters.*

We applied a certain voltage to the emitter for 40 h and monitored the change of the emission current to investigate the field emission stability of both emitters to study the field emission stability of these CNT-based field emitters. We applied 4000 V and 3600 V, where the emission current saturated for the F-tip emitter and the S-tip emitter, respectively. Fig. 4.18 shows the field emission stability of the F-tip and S-tip emitters. Both emitters showed very stable emission current during the stability test. The emission current from the F-tip emitter gradually decreased from an initial current of about 40 μA to around 30 μA. Similarly, the emission current from the S-tip emitter gradually decreased from about 13 μA to 10 μA. There was no sudden degradation of emission current for either of the two kinds of point emitters during the stability test. We attribute the excellent field emission stability of our CNT point emitters to the good morphologies and the strong adhesion between CNTs and the Cu wire.

It is well known that field emission properties are largely dependent on the morphology of the CNTs. Table 4.3 shows field emission properties of various point emitters on different support materials [73-80]. Most of these point emitters were grown on tungsten tip (W tip) and were randomly oriented CNTs. The CNT point emitters directly grown on Cu wires demonstrated a comparable to or even better field emission properties than other point emitters. Especially, the point emitters on Cu wires showed a very stable field emission current during the stability test for 40 h. The observed stability is a good feature for the practical applications of miniaturized X-ray sources and electron beam sources. The different field emission properties were attributed to the morphology difference between the two kinds of CNT point emitters, especially to the density of CNTs.

As mentioned earlier, for the F-tip emitter, the length of the CNTs is about 1.5 μm and the CNT had a large diameter of 110–140 nm at the tip. For the S-tip emitter, the CNT has a short length in the range of 0.7–1.0 μm and a diameter of around 100 nm. Therefore, we consider that the field enhancement factor of the emitter itself in the F-tip emitter is slightly bigger than or similar to that in the S-tip emitter as evident from $\beta = 1.2[2.15+h/r]^{0.9}$. However, the density of CNTs in the S-tip emitter was much lower compared to that in the F-tip emitter. The high density of CNTs can highly degrade the field emission performance of CNT emitters as a result of the screening effect [17]. Therefore, the S-tip emitter showed a better field emission performance compared with the F-tip emitter. In this work, we consider that the density of CNTs playing a dominant role in the field emission because the S-tip emitter demonstrated a better field emission

performance than the F-tip emitter. This means that the screening effect which reduces the local electric field is more dominant than the geometry of CNTs in field emission in this work.

Table 4.3: Field emission properties of various point emitters.

Support	Fabrication method	CNT orientation	Gap	Best emission	Best stability	Ref.
W tip	PECVD	Randomly	250 μm	26 μA @ 1200 V	26 μA @ 1200	[73]
W tip	PECVD	Randomly	250 μm	51 μA @ 630 V	Over 40 h @ 10 mA	[74]
W tip	Pyrolysis of ferrocene	Randomly	5 cm	1 mA @ 16.5 KV	200 min @ 500 μA	[75]
W wire	Biased thermal CVD	Randomly	1 mm	4 μA @ 6000 V	15 h @ 1.2 μA	[76]
W tip	PECVD	Vertically	1-10 mm	100 μA below 10 kV	100 h @ 80 μA	[77]
Pd wire	PECVD	Vertically	0.5 mm	1.3 mA @ 3400 V	Over 500 h @ 1 mA	[78]
W tip	CNT/Ag paste	Randomly	2 mm	465 μA @ 6600 V	40 h @ 100 μA	[79]

4.4 Conclusions

In summary, the enhancement of electron field emission of CNT emitters has been achieved by using three separate approaches. Vertically aligned CNTs were synthesized on copper substrates with Ni catalyst nanodots patterned by nanosphere lithography. The density and location of CNTs were determined by the diameter of spheres. The as-synthesized CNTs followed a tip-growth mechanism with the Ni catalyst forming almost a core–shell like structure several nanometers long in many cases. The low-density CNTs and the low contact resistance between the CNTs and the metal substrate were favorable for the field emission process. Among the high-density CNTs grown on Ni catalyst film and low-density CNTs grown on NSL patterned Ni catalyst dots, low-density CNTs synthesized on catalyst dots patterned from spheres of diameter 0.5 μm exhibited the best field emission properties in terms of lower turn-on and threshold field, higher field enhancement, and longer stability. These results could facilitate the direct fabrication of more cost-effective and site-selective CNT structures compatible with novel nanoelectronic devices.

The effects of NH_3 plasma treatment on the microstructure and field emission properties of vertically aligned CNTs grown on a Cu substrate were investigated. After 1.0 min treatment, a great improvement on the field emission properties of the CNTs was obtained. This improvement was caused primarily by the morphology change. The CNTs changed from the cylindrical shape to the tapered shape after plasma treatment. The thinner tips of the CNTs could easily touch each other to form clusters; consequently, the inter-tip distance increased. The tips of the CNTs were opened by the plasma treatment,

and a high density of structural defects was introduced into the CNTs, both of which could improve field emission performance. The nitrogen doping induced by NH_3 plasma treatment might also effectively improve the field emission properties. All the results indicate that NH_3 plasma treatment could be an effective way to improve the field emission performance of CNTs.

In another approach, the performance of vertically aligned CNT point emitters grown on Cu wires with flat or sharp tips were compared. The F-tip emitter showed tapered CNTs with a longer length, thinner diameter, and a high density whereas the S-tip emitter showed almost cylindrical CNTs with a shorter length, a thicker diameter, and a low density. The CNTs on the F-tip displayed a multi-walled bamboo-liked structure whereas the CNTs on the S-tip showed no clear graphitization because of the difficulty in separating a single CNT from the bundles. The two types of point emitters have exhibited excellent field emission performance, such as high emission current at relatively low voltage and longtime emission stability at high current level. The excellent field emission properties are attributed to the point emitter structure and the good contact between the CNTs and the Cu tip. We believe that the CNT point emitters grown on Cu wires are beneficial to the real application of miniaturized X-ray sources and electron beam sources.

In conclusion, inter-tip distance appeared to be the most important factor that dominates the electron emission from CNTs. The close proximity of CNT emitters resulted in the screening of the electric field by the adjacent emitters and thus the degraded emission properties in the case of CNT emitters synthesized over a catalyst thin

film. The separation between CNT emitters could be tailored by the selective growth at predetermined distances or post-growth treatments to obtain the stable electron sources.

4.5 References

[1] Iijima S 1991 *Nature* 354, 56

[2] Treacy M M J, Ebbesen T W and Gibson J M 1996 *Nature* 381, 678

[3] Chang R P H, Wang Q H, Setlur A A, Lauerhaas J M, Dai J Y and Seelig E W 1998 *Applied Physics Letters* 72, 2912

[4] Kim J M, Lee N S, Chung D S, Han I T, Kang J H, Choi Y S, Kim H Y, Park S H, Jin Y W, Yi W K, Yun M J, Jung J E, Lee C J, You J H, Jo S H and Lee C G 2001 *Diamond and Related Materials* 10, 265

[5] Zhou O, Yue G Z, Qiu Q, Gao B, Cheng Y, Zhang J, Shimoda H, Chang S and Lu J P 2002 *Applied Physics Letters* 81, 355

[6] de Jonge N, Lamy Y, Schoots K and Oosterkamp T H 2002 *Nature* 420, 393

[7] Teo K B K, Milne W I, Minoux E, Groening O, Gangloff L, Hudanski L, Schnell J P, Dieumegard D, Peauger F, Bu I Y Y, Bell M S, Legagneux P, Hasko G and Amaratunga G A J 2006 *Journal of Vacuum Science & Technology B* 24, 345

[8] Meyyappan M, Delzeit L, Cassell A and Hash D 2003 *Plasma Sources Science & Technology* 12, 205

[9] Coville N J, Shaikjee A and Franklyn P J 2011 *Carbon* 49, 2950

[10] Li Y, Zhou W W, Han Z Y, Wang J Y, Zhang Y, Jin Z, Sun X, Zhang Y W and Yan C H 2006 *Nano Letters* 6, 2987

[11] Talapatra S, Kar S, Pal S K, Vajtai R, Ci L, Victor P, Shaijumon M M, Kaur S, Nalamasu O and Ajayan P M 2006 *Nature Nanotechnology* 1, 112

[12] Liu Y Q, Wang B A, Liu X Y, Liu H M, Wu D X, Wang H P, Jiang J M, Wang X B, Hu P A and Zhu D B 2003 *Journal of Materials Chemistry* 13, 1124

[13] Dubosc M, Casimirius S, Besland M P, Cardinaud C, Granier A, Duvail J L, Gohier A, Minea T, Arnal V and Torres J 2007 *Microelectronic Engineering* 84, 2501

[14] Chattopadhyay K K, Banerjee D and Jha A 2010 *Applied Surface Science* 256, 7516

[15] Mata D, Amaral M, Fernandes A J S, Oliveira F J, Costa P M F J and Silva R F 2011 *Carbon* 49, 2181

[16] Lahiri I, Seelaboyina R, Hwang J Y, Banerjee R and Choi W B 2010 *Carbon* 48, 1531

[17] Nilsson L, Groening O, Emmenegger C, Kuettel O, Schaller E, Schlapbach L, Kind H, Bonard J M and Kern K 2000 *Applied Physics Letters* 76, 2071

[18] Ren Z F, Huang Z P, Carnahan D L, Rybczynski J, Giersig M, Sennett M, Wang D Z, Wen J G and Kempa K 2003 *Applied Physics Letters* 82, 460

[19] Teo K B K, Lee S B, Chhowalla M, Semet V, Binh V T, Groening O, Castignolles M, Loiseau A, Pirio G, Legagneux P, Pribat D, Hasko D G, Ahmed H, Amaratunga G A J and Milne W I 2003 *Nanotechnology* 14, 204

[20] Kim D H, Cho D S, Jang H S, Kim C D and Lee H R 2003 *Nanotechnology* 14, 1269

[21] Jiao J, Wu J, Eastman M, Gutu T, Wyse M, Kim S M, Mann M, Zhang Y and Teo K B K 2007 *Applied Physics Letters* 91

[22] Lee Y H, Lee C J, Kim D W, Lee T J, Choi Y C, Park Y S, Choi W B, Lee N S, Park G S and Kim J M 1999 *Chemical Physics Letters* 312, 461

[23] Ren Z F, Tu Y and Lin Y H 2003 *Nano Letters* 3, 107

[24] Dionne M, Coulombe S and Meunier J L 2008 *Ieee Transactions on Electron Devices* 55, 1298

[25] Wang X Q, Wang M, Ge H L, Chen Q and Xu Y B 2005 *Physica E-Low-Dimensional Systems & Nanostructures* 30, 101

[26] Terrones M, Charlier J C, Baxendale M, Meunier V, Zacharia T, Rupesinghe N L, Hsu W K, Grobert N, Terrones H and Amaratunga G A J 2002 *Nano Letters* 2, 1191

[27] Hong J P, Ahn K S, Kim J S and Kim C O 2003 *Carbon* 41, 2481

[28] Zeng B Q, Xiong G Y, Chen S, Wang W Z, Wang D Z and Ren Z F 2006 *Applied Physics Letters* 89

[29] Cheng H F, Hsieh Y S, Chen Y C and Lin I N 2004 *Diamond and Related Materials* 13, 1004

[30] Lee C J, Liu C, Kim K S, Baek J, Cho Y, Han S, Kim S W, Min N K, Choi Y and Kim J U 2009 *Carbon* 47, 1158

[31] Ahn K S, Kim J S, Kim C O and Hong J P 2003 *Carbon* 41, 2481

[32] Gohel A, Chin K C, Zhu Y W, Sow C H and Wee A T S 2005 *Carbon* 43, 2530

[33] Gui X C, Wei J Q, Wang K L, Xu E Y, Lv R T, Zhu D, Guo Z G, Kang F Y, Zhu Y Q, Li D J, Zhu H W and Wu D H 2010 *Materials Research Bulletin* 45, 568

[34] Lee K, Lim S C, Choi Y C and Lee Y H 2008 *Applied Physics Letters* 93, 063101

[35] Zhu Y W, Cheong F C, Yu T, Xu X J, Lim C T, Thong J T L, Shen Z X, Ong C K, Liu Y J, Wee A T S and Sow C H 2005 *Carbon* 43, 395

[36] Hou Z Y, Cai B C, Liu H and Xu D 2008 *Carbon* 46, 405

[37] Fursey G N, Novikov D V, Gyuzhev G A, Kotcheryzhenkov A and Vassiliev P O 2003 *Applied Surface Science* 215, 135

[38] Ferrer D, Tanii T, Matsuya I, Zhong G, Okamoto S, Kawarada H, Shinada T and Ohdomari I 2006 *Applied Physics Letters* 88, 033116

[39] Chen G H, Shin D H, Roth S and Lee C J 2009 *Nanotechnology* 20, 315201

[40] Wei Y, Xie C G, Dean K A and Coll B F 2001 *Applied Physics Letters* 79, 4527

[41] Hofmann S, Ducati C, Robertson J and Kleinsorge B 2003 *Applied Physics Letters* 83, 135

[42] Lee S, Park K H, Koh K H, Lacerda R, Teo K B K and Milne W I 2005 *Journal of Applied Physics* 97

[43] Houweling Z S, Verlaan V, ten Grotenhuis G T and Schropp R E I 2009 *Thin Solid Films* 517, 3566

[44] Chhowalla M, Ducati C, Rupesinghe N L, Teo K B K and Amaratunga G A J 2001 *Applied Physics Letters* 79, 2079

[45] Ph. Buffat and Borel J-P 1976 *Physical Review A* 13, 2287

[46] Derakhshandeh J, Abdi Y, Koohsorkhi J, Mohajerzadeh S, Hoseinzadegan H, Robertson M D, Bennett J C, Wu X and Radamson H 2006 *Materials Science & Engineering C-Biomimetic and Supramolecular Systems* 26, 1219

[47] Lee C J, Chen G H, Shin D H, Iwasaki T and Kawarada H 2008 *Nanotechnology* 19

[48] Fujii S, Honda S, Machida H, Kawai H, Ishida K, Katayama M, Furuta H, Hirao T and Oura K 2007 *Applied Physics Letters* 90

[49] de Jonge N, Allioux M, Doytcheva M, Kaiser M, Teo K B K, Lacerda R G and Milne W I 2004 *Applied Physics Letters* 85, 1607

[50] Groning O, Kuttel O M, Emmenegger C, Groning P and Schlapbach L 2000 *Journal of Vacuum Science & Technology B* 18, 665

[51] Zheng X, Chen G H, Li Z B, Deng S Z and Xu N S 2004 *Physical Review Letters* 92

[52] Lim S C, Jang J H, Bae D J, Han G H, Lee S, Yeo I S and Lee Y H 2009 *Applied Physics Letters* 95

[53] Ramaprabhu S, Rakhi R B, Reddy A L M, Shaijumon M M and Sethupathi K 2008 *Journal of Nanoparticle Research* 10, 179

[54] Dionne M, Coulombe S and Meunier J L 2009 *Physical Review B* 80

[55] Dionne M, Coulombe S and Meunier J L 2008 *Journal of Physics D-Applied Physics* 41

[56] Coulombe S and Meunier J L 1997 *Journal of Physics D-Applied Physics* 30, 776

[57] Dionne M, Coulombe S and Meunier J L 2009 *Physical Review B* 80, 085429

[58] Doytcheva M, Kaiser M and de Jonge N 2006 *Nanotechnology* 17, 3226

[59] Wei W, Liu Y, Wei Y, Jiang K L, Peng L M and Fan S S 2007 *Nano Letters* 7, 64

[60] Pandey A, Prasad A, Moscatello J, Ulmen B and Yap Y K 2010 *Carbon* 48, 287

[61] Kyung S J, Park J B, Lee J H and Yeom G Y 2006 *Journal of Applied Physics* 100, 124303

[62] Dionne M, Coulombe S and Meunier J L 2008 *Journal of Physics D-Applied Physics* 41, 245304

[63] Nilsson L, Groening O, Groening P and Schlapbach L 2001 *Applied Physics Letters* 79, 1036

[64] Edgcombe C J and Valdre U 2001 *Journal of Microscopy-Oxford* 203, 188

[65] Cui H, Zhou O and Stoner B R 2000 *Journal of Applied Physics* 88, 6072

[66] Zhi C Y, Bai X D and Wang E G 2002 *Applied Physics Letters* 81, 1690

[67] Vincent P, Purcell S T, Journet C and Binh V T 2002 *Physical Review B* 66, 075406

[68] Neupane S, Lastres M, Chiarella M, Li W Z, Su Q M and Du G H 2012 *Carbon* 50, 2641

[69] Bhattacharyya S, Cardinaud C and Turban G 1998 *Journal of Applied Physics* 83, 4491

[70] Ma H, Berthier Y and Marcus P 2002 *Corrosion Science* 44, 171

[71] Agouram S, Bodart F and Terwagne G 2004 *Journal of Electron Spectroscopy and Related Phenomena* 134, 173

[72] Che R C, Peng L M and Wang M S 2004 *Applied Physics Letters* 85, 4753

[73] Heo S H, Ihsan A and Cho S O 2007 *Applied Physics Letters* 90, 183109

[74] Kim J P, Kim Y K, Park C K, Choi H Y, Shon C H, Kim J U and Park J S 2009 *Diamond and Related Materials* 18, 486

[75] Sharma R B, Tondare V N, Joag D S, Govindaraj A and Rao C N R 2001 *Chemical Physics Letters* 344, 283

[76] Zhang Y B, Lau S P, Huang L and Tanemura M 2005 *Applied Physics Letters* 86, 123115

[77] Sakai Y, Tone D, Nagatsu S, Endo T, Kita S and Okuyama F 2009 *Applied Physics Letters* 95, 073104

[78] Kita S, Sakai Y, Fukushima T, Mizuta Y, Ogawa A, Senda S and Okuyama F 2004 *Applied Physics Letters* 85, 4478

[79] Heo S H, Ihsan A, Yoo S H, Ali G and Cho S O 2010 *Nanoscale Research Letters* 5, 720

[80] Cheng H F, Tsau Y M, Chang T Y, Lai T S, Kuo T F and Lin I N 2002 *Physica B-Condensed Matter* 323, 158

CHAPTER 5.0

Field emission properties of vertically aligned carbon nanotubes on stainless steel

In this chapter, the synthesis and characterization of vertically aligned carbon nanotube arrays on stainless steel substrate will be discussed. Then, the field emission properties of these carbon nanotubes (CNTs) were studied to understand the correlation between their structure and field emission properties.

5.1 Introduction

Carbon nanotubes have attracted a great research interest since the landmark report on the discovery of CNTs by Iijima in 1991 [1]. As discussed in earlier sections, CNTs exhibit superior chemical stability, remarkable electrical and thermal conductivities, and robust structural integrity. These properties can be exploited for possible applications in field emission devices, gas sensors, Li-ion battery, and nanoelectronics [2-4]. However, for a viable application, it is desirable to have a controlled growth of aligned CNTs at relatively lower temperatures compatible with currently available device fabrication techniques. Plasma enhanced chemical vapor deposition (PECVD) process has been adopted as a suitable method to synthesize arrays of vertically aligned CNTs at lower temperatures than the conventional arc-discharge or laser ablation methods [5]. In addition, it is also possible to control the length, diameter, and density of CNTs by adjusting the various parameters during the PECVD synthesis [6, 7].

Carbon nanotubes are ideal candidates for electron field emission applications because of their high aspect-ratio. The emission current from CNTs can also be expressed by Fowler-Nordheim (F-N) equation: $I = a\, E_{eff}^{2}\, exp\ (-b/\, E_{eff})$, where the constants a and b are dependent on the work-function of the material and the local electric field at the emission tip [2]. The effective electric field (E_{eff}) can be expressed as $E_{eff} = \beta E_o$, where E_o is the applied electric field between the CNT emitters and the anode, and β is the field enhancement factor. The large aspect-ratio of CNTs enables a higher field enhancement and consequently the increased emission current. Carbon nanotubes can also act as efficient electrode material for electrochemical tests because of their superior conductivity and great charge transfer rate [8]. Carbon nanotubes offer high surface area which is easily accessible for ions to interact during electrochemical measurements. As a result, charges can be quickly stored and then released at the CNT electrodes for efficient performance of devices with a quick response time. However, for a reliable performance of a fabricated device, the adhesion of the CNTs to the substrate and the density of the CNTs play a crucial role during the electrical and electrochemical measurements.

Recently, many efforts have been focused on the synthesis of arrays of vertically aligned CNTs (VACNTs) directly on conductive metals or their alloys such as copper, nickel, titanium, stainless steel (SS), inconel, nichrome and others [9-12]. The in-situ synthesis of CNTs on conductive substrates prevents the introduction of impurities and defects on CNTs incurred during the device fabrication for various applications. Growth of CNTs on metallic substrates or their alloys have been performed by first depositing a thin layer of catalyst on the metal substrate and then initiating a thermal decomposition of

carbonaceous precursor on the catalyst 'seed'. In this approach, usually the substrates will be subjected to chemical or thermal treatment prior to the introduction of a carbon source for CNT growth [12-19]. Wang *et al*. used acid-assisted electrochemical polishing and plasma pre-treatment to obtain VACNTs on SS [13]. Park *et al*. treated SS substrate with HF etching and hydrogen plasma during the sequential combination of PECVD and thermal chemical vapor deposition (CVD) to obtain randomly oriented spaghetti-like CNTs [14]. Lin *et al*. were successful in synthesizing CNTs by PECVD and studying their field emission properties [18]. Sparse but well-aligned CNTs were synthesized for the growth period of 5 min, and the growth had to be prolonged for about 30 min to obtain a dense array of VACNTs. Synthesis of CNTs with non-uniform substrate coverage were reported by Masarapu *et al*. and Baddour *et al*. on SS substrates subjected to chemical etching to activate nucleation sites prior to the growth [15, 16]. Parthangal *et al*. reported the synthesis of randomly oriented and weakly adhered CNTs on SS by CVD method [12]. There have been further attempts to deposit a catalyst layer to enhance the quality of as-synthesized CNTs on SS. Abad *et al*. reported the PECVD synthesis of sparse and thick bundles of CNTs on bare SS, while the cobalt nanoparticle on SS catalyzed a dense growth of VACNTs [19]. Kim *et al*. used a water assisted CVD to grow CNTs on Al and Fe coated SS [17]. Duy *et al*. synthesized VACNTs on Ni coated SS substrates (with a buffer layer of 100 nm TiN) by PECVD and studied their field emission properties [11]. Most of the reported results rely on chemical, thermal, or plasma treatment of pristine SS or metal-catalyzed SS to develop active nucleation sites before the introduction of carbon precursor for the growth of CNTs. The pretreatment of substrate is regarded as an efficient and essential approach for the formation of

homogenous granular nanoscale structures which act as catalysts for the uniform growth of VACNTs.

Synthesis of CNTs on SS was widely reported; however, the vertical alignment mechanism of the as-synthesized CNTs and a detailed characterization of their electrical and electrochemical properties of the as-synthesized CNTs are still lacking. In this chapter, we report the synthesis of arrays of VACNTs on pristine SS 304 substrate with or without any chemical treatments. We have also analyzed the topological features of the substrate after chemical etching for different times to develop an understanding of the evolution of the surface and the resulting particles. We have also examined the progression of CNT structures upon increasing the growth time. We further investigated the field emission performance of CNTs synthesized directly on SS substrates. The emission performance was compared between CNT arrays synthesized on pristine SS and Ni/Cr catalyzed SS. The conventional role of the buffer layer of Cr is to facilitate a robust contact between the CNTs with the substrate while Ni acts as a catalyst for the growth of CNTs.

5.2 Experimental methods

Vertically aligned CNT arrays were synthesized by PECVD process. The details of the process have been described earlier in section 3.2. Briefly, a SS substrate (1 cm × 1 cm × 0.1 mm) was loaded into a PECVD system which was then pumped to a pressure of 5×10^{-6} torr. The SS substrate was heated to a temperature of 600 °C while NH_3 was introduced at a constant flow rate of 100 sccm. Then, C_2H_2 was introduced as the carbon source at 30 sccm. The power of the DC plasma was maintained at 70 W and the pressure

was fixed at 8 torr during the CNT growth [7]. On a different approach, pristine SS substrates were chemically etched in a mixture of concentrated H_2SO_4: H_2O_2: H_2O (4:1:15, volume ratio) for different time durations in an ultrasonic bath. The chemically treated substrates were used to grow CNTs by PECVD using the same conditions as described above. The morphology of CNTs synthesized on as-treated SS substrates was investigated. The field emission measurements were performed as described earlier in sections 3.9.

5.3 Results and discussions

5.3.1 Effect of synthesis time on the formation of CNTs

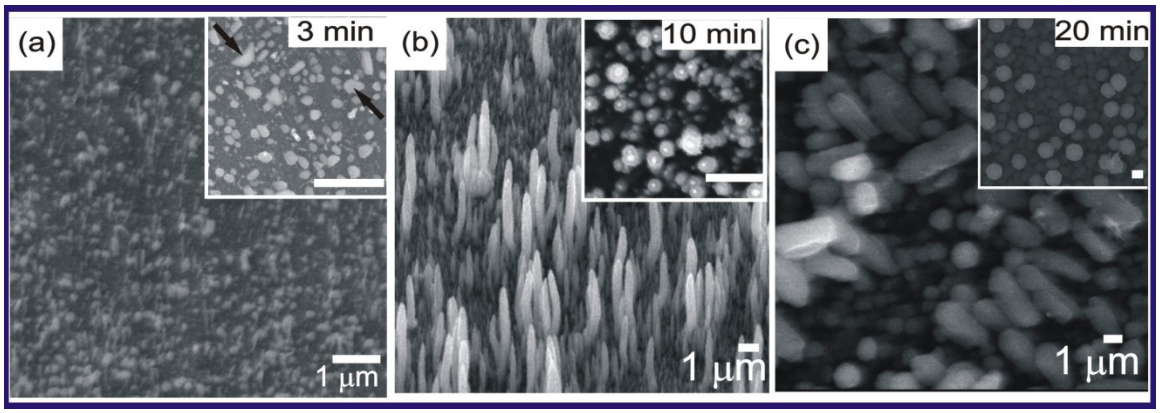

Figure 5.1: *SEM images (30° tilt-view) of CNTs grown on pristine SS substrates at 600 °C for (a) 3 min, (b) 10 min, and (c) 20 min. The inset in each image shows the corresponding top-view image of the CNTs. All scale bars are 1 μm.*

The synthesis time plays an important role in the length and diameter of CNTs. Figure 5.1 shows the SEM images of CNTs synthesized on SS without any external catalyst or chemical etching. The ammonia-plasma etching exposes the intrinsic Fe, Co,

and Ni present on the SS, all of which can act as catalyst for the growth of CNTs. Hence, chemical pretreatment to the SS substrates would not be necessary to synthesize CNTs by PECVD. As evident from the growth after 3 min, the CNTs show a random distribution in the initial phase of growth. These CNTs acquire an average length of 600 nm after the 3 minute growth and the diameters also differ on an individual basis. In addition to these CNTs, the substrate contains catalyst particles of irregular sizes as shown by the dark arrows in the inset. With the onset of plasma treatment, the substrate forms catalyst fragments of different dimensions; the smaller of which contributes toward the growth of CNTs while the bigger ones remain. In comparison to the sample after 3 min growth, the CNTs after 10 minutes growth exhibit an increased density and length, Fig. 5.1(b). After a prolonged synthesis time, new nucleation sites develop in the area where the density of CNTs from 3 minutes growth was low, as a result, the density of the CNTs after 10 minutes will increase significantly. After 10 minutes growth, the average length of the CNTs is 3.4 μm with the diameter around 80 nm. It is also observed that the big catalyst particles have disappeared most probably as a result of the continuous etching of plasma. The small individual catalyst particles formed from further plasma etching can initiate the growth of CNTs, contributing to an increased density of CNTs as compared to samples with 3 min growth. A further increase in the synthesis time to 20 min led to short and stubby microstructures with an average length of 2.5 μm and diameter of 1 μm, Fig. 5.1(c). It has been reported that the catalyst particles lose their catalytic activity in PECVD growth after a certain period, and the growth of CNTs ceased [20]. Beyond this point, the plasma starts the destructive etching to the CNTs which results in the taller CNTs to fall apart. After 20 min of growth, the height of the CNTs was uniform and the

diameter was increased, which could be attributable to the deposition of amorphous carbon on the exterior of the CNTs. These results indicate that the growth time of CNTs can be varied to produce CNTs of desired length and density.

5.3.2 Effect of chemical etching on the formation of CNTs

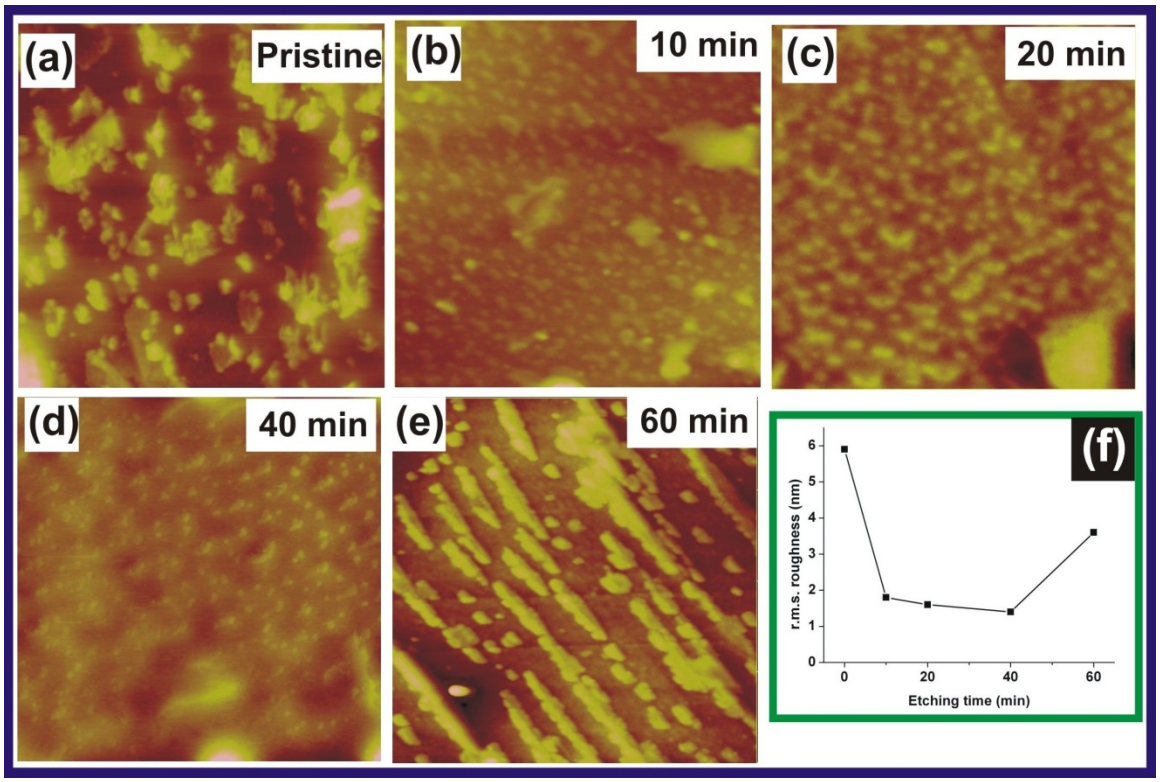

Figure 5.2: *AFM images of stainless steel substrates chemically etched for (a) 0, (b) 10, (c) 20, (d) 40, and (e) 60 min, respectively. (f) Graph showing the variation of surface roughness with different chemical etching time. The scan size of all AFM images is 1 μm.*

Stainless steel-304 is commercially available with a Cr rich passive oxide film which prevents against the corrosion [15]. Chemical etching of SS substrates before growth will remove this layer and expose islands of Fe which act as catalyst islands for the growth of CNTs. Figs. 5.2(a-e) show the AFM images of the surfaces of the as-

received pristine SS and SS substrates after chemical etching for 10, 20, 40, and 60 min, respectively. As expected, the pristine SS surface is rough with grain sizes of non-uniform dimensions scattered across the surface as shown in Fig. 5.2(a). After etching the SS for 10 min, the surface morphology changed with the appearance of particles as shown in Fig. 5.2(b). The number of particles increased further after etching for 20 min, Fig. 5.2(c). After 40 min, as shown in Fig. 5.2(d), uniformly distributed fine particles were observed on the surface. A 60 min chemical etching resulted in ridges or lines of big particles on the substrate surface because the small particles were etched away and only large particles remained. The root mean square roughness were 5.9, 1.8, 1.6, 1.4, and 3.6 nm for surfaces etched for 0, 10, 20, 40, and 60 min, respectively. The evolution of the surface roughness for different etching periods has been shown in Fig. 5.2(f). The results show that a 40-minute chemical etching resulted in fine particles with uniform sizes which will be favorable for the growth of CNTs with uniform diameter. It should also be noted that a catalyst particle of few nanometers may be blown away during thermal annealing and plasma annealing before the introduction of carbon precursor in the PECVD growth.

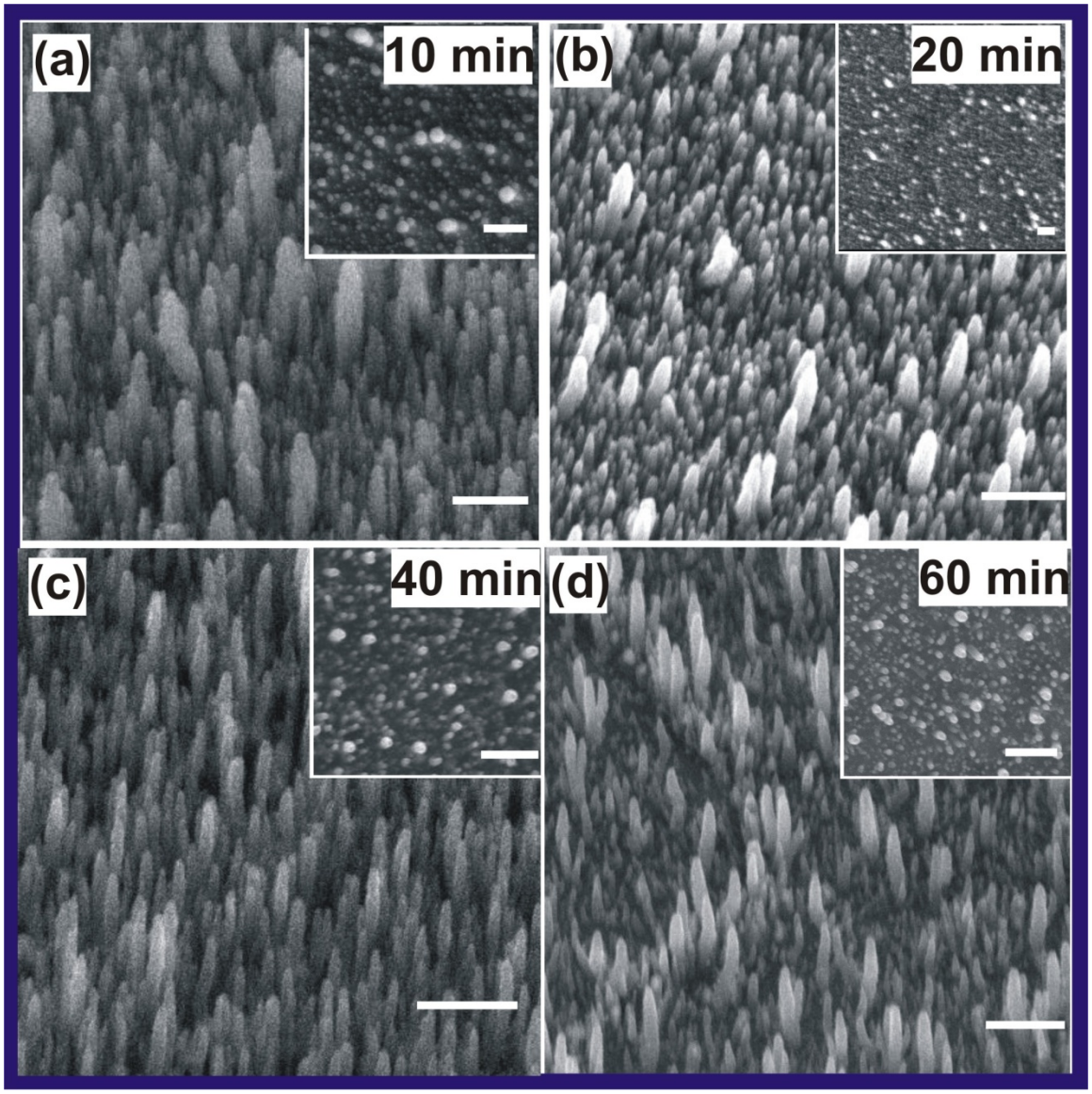

Figure 5.3: *SEM images (30° tilt-view) of CNTs grown on SS substrates chemically etched in a mixture of H_2SO_4: H_2O_2: H_2O (4:1:15, volume ratio) for (a) 10 min, (b) 20 min, (c) 40 min, and (d) 60 min respectively. The synthesis was carried at 600 °C for 10 min. The insets show the corresponding top-view images of the CNTs. All scale bars are 1 μm.*

Figures 5.3(a-d) show the morphology of CNTs synthesized on SS substrates subjected to chemical etching for 10, 20, 40, and 60 min, respectively. The insets show the corresponding top-view images of the CNTs. The growth was carried out at 600 °C

for 10 min. The average diameter of CNTs for the case of 10 min etching was 190 nm and the length was 1.7 μm, Fig. 5.3(a). The average length of the CNTs increased to 2.2 μm and 3.4 μm for CNTs synthesized on SS subjected to the chemical etching for a period of 20 min and 40 min respectively, while the respective diameter decreased to 160 nm and 95 nm, Fig. 5.3(b) and (c). The decrease in the diameter of the CNTs grown on SS for an increased etching time can be understood as follows: an increase in the etching period resulted in small grain sizes of the catalysts which grew CNTs with small diameter. A further increase in the chemical etching time to 60 min resulted in short and thick CNTs with a high degree of variation in lengths. The average length of the resulting CNTs was 1.7 μm and the diameter was 140 nm, Fig. 5.3(d). The chemical etching for 60 min resulted in rougher surface and reduced the density of small particles which were favorable for the nucleation of CNTs. Hence the site density of CNTs decreased as evident from the top-view images in the inset of Fig. 5.3(d). A careful comparison between Figs. 5.1(b) and 5.3(c) shows that for the same growth time interval, the diameter and length of the CNTs were more uniform for the growth on chemically etched SS than on the pristine SS substrate. An optimum chemical etching to the SS substrate induced a homogenous distribution of catalyst particles and resulted in the CNTs with uniform length and diameter.

5.3.3 TEM analysis

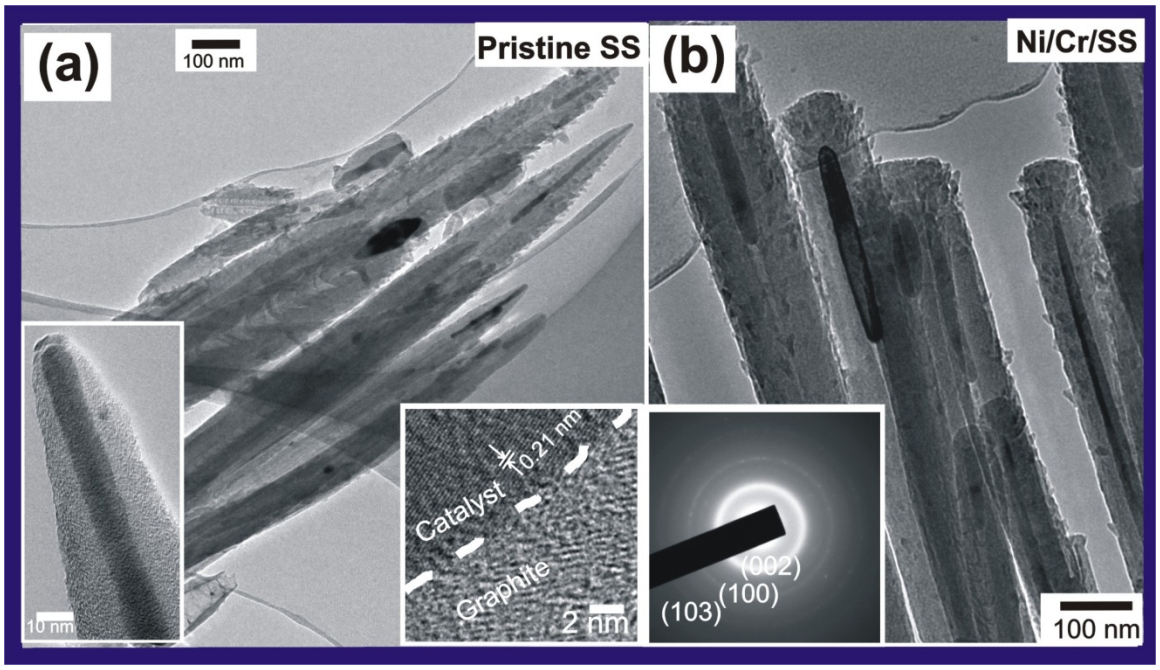

Figure 5.4: *TEM images of CNTs synthesized on (a) pristine SS, and (b) Ni/Cr catalyzed SS. The inset on the left side of (a) shows a rod-like Fe catalyst encapsulated inside a CNT, forming a core-shell structure. The inset on the right side of (a) shows the interface between the graphitic layers of the CNT and the Fe trapped inside the CNT. The inset in (b) shows the SAED pattern of the Fe-filled CNTs.*

The graphitic structures of the as-synthesized CNTs were verified by TEM analysis. Figs. 5.4(a-b) show the TEM images of the CNTs synthesized on pristine SS and Ni/Cr catalyzed SS, respectively. In one of the experiments, CNTs were synthesized on Ni catalyzed SS with a buffer layer of Cr since a thin layer of Cr ensures the better adhesion between the substrate and as-synthesized CNTs [6]. Thin films of Cr and Ni were deposited onto SS substrates by e-beam evaporation at a pressure of 2×10^{-6} torr at room temperature. The thickness of Cr and Ni layers was 15 nm and 6.5 nm, respectively. The synthesis time was 10 minutes with the temperature maintained at 600 °C for both

samples. TEM images show that there is a slight variation in the diameter of individual CNTs as the diameter is dependent on the size of the catalyst particle formed right before the introduction of C_2H_2. Big catalyst fragments result in thick tubes while small particles result in thin tubes. We found that these CNTs show similar growth mechanism with catalyst particles in the tip. The graphitic planes are not always parallel to the tube axis but are often twisted and broken to form a bamboo-like growth pattern, which is the common characteristic of the PECVD process [21]. The inset on the left of Fig. 5.4(a) shows a typical image of a catalyst rod encapsulated inside a CNT forming a core-shell structure. The compressive force of the graphene layers during the growth results in the formation of these core-shell structures [22]. At nanoscale dimensions, the melting point of metal catalysts can be significantly lower than that of their bulk counterparts. Hence there is a high probability of melting of the catalyst particles which may get trapped half way up the tube. The HRTEM image, as shown in the inset on the right side of Fig. 5.4(a), shows the interface between the graphitic planes of CNTs and the planes of the catalyst core in the core-shell structure. The graphitic planes that make up the CNT are observed on the right part of the image in light contrast. The catalyst core also exhibits crystalline structure with atomic planes separated by 0.21 nm corresponding to Fe (111) planes. In most cases, the (111) lattice planes of Fe make an angle with the tube axis of CNTs. The concentric rings obtained in the SAED pattern (inset in Fig. 5.4(b)) also confirm the hollow tube with many layers in the multiwalled CNTs.

5.3.4 Field emission properties of CNTs

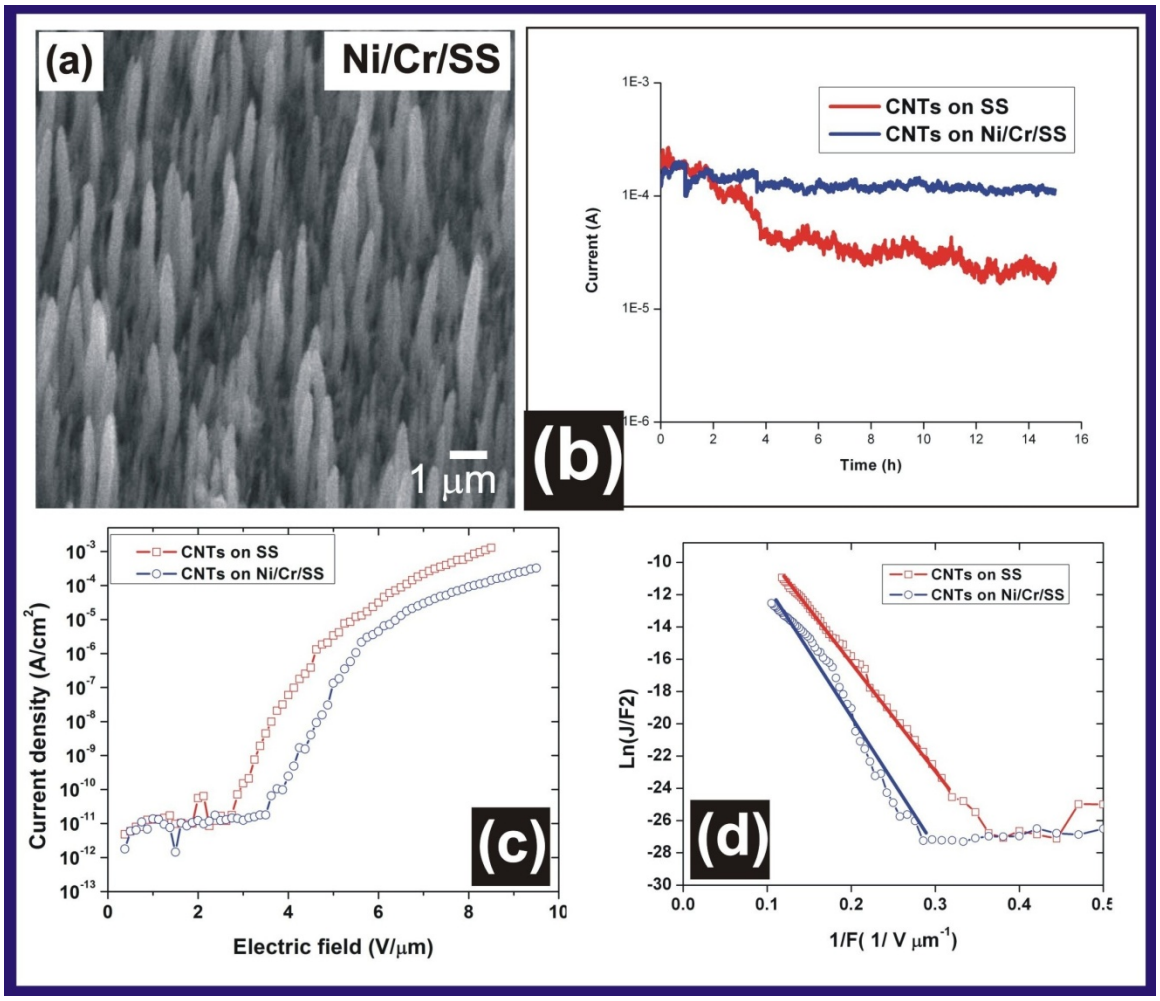

Figure 5.5: *Field emission properties of CNTs grown on pristine SS and Ni/Cr coated SS. (a) SEM images of CNT emitters on Ni/Cr coated SS (30° tilt-view), the CNTs were synthesized at 600 °C for 10 min. (b) Stability test, (c) F–J plots, and (d) F–N plots.*

To understand the performance of CNT emitters, field emission current from CNTs synthesized on pristine SS was measured. The emission current was also compared with that of the CNTs synthesized on Ni/Cr coated SS as Cr is known to provide a stable adhesion of CNTs to the substrate. The synthesis time of CNT emitters was 10 min for

both samples and the temperature was fixed at 600 °C. From the SEM images, the average length and diameter of the CNT emitters synthesized on Ni/Cr coated SS are 2.8 μm and 100 nm respectively as shown in Fig. 5.5(a). During the emission current measurement, the applied voltage was increased steadily in the steps of 200 V until the emission current saturated. The emission current was increased to the maximum value for each sample and the applied voltage was kept constant for 15 h to test the stability of the emission current. The emission current was measured several times for each of the CNT samples exposed to 'electric annealing' to confirm the repeatability of the emission characteristics. The field emission performance of CNTs synthesized on pristine SS and Ni/Cr coated SS is shown in Figs. 5.5(b-d). Both types of CNT emitters exhibit excellent field emission properties with high current density and long stability. From the curves of current density versus applied electric field (F-J plots) in Fig. 5.5(c), we can estimate the turn-on ($E_{turn\text{-}on}$) and threshold (E_{th}) electric fields [23]. The numerical values for $E_{turn\text{-}on}$ and E_{th} for CNTs on pristine SS were 4.7 V/μm and 8.3 V/μm respectively. Similarly, the corresponding electric fields were 5.5 V/μm and 10 V/μm for the CNTs synthesized on Ni/Cr coated SS. The lower values of E_{th} and $E_{turn\text{-}on}$ for CNTs grown on pristine SS suggest that the electrons emission is easier from the CNTs grown on pristine SS substrate than from the CNTs grown on the Cr buffer layer on the SS substrate. During the process of field emission, the electron should cross the interface between the substrate and the buffer layer (Cr), then pass through the CNTs, and finally emit into the vacuum. Although the presence of a Cr layer would ensure the robust contact between the CNTs and the substrate, the emitted electrons are subjected to a higher contact resistance, thereby increasing $E_{turn\text{-}on}$ and E_{th}. CNTs synthesized on pristine SS exhibit better field

emission properties since they experience lower contact resistance than the CNTs synthesized on SS with the buffer layer of Cr. Fig. 5.5(d) shows the corresponding F-N plots for the CNT emitters grown on SS and on Ni/Cr coated SS. The straight line in the high electric field region shows the quantum mechanical tunneling process [24]. From the F-N plots, the field enhancement factor (β) was estimated to be 1140 and 950 for CNTs grown on pristine SS and Ni/Cr coated SS, respectively, assuming the work function is 5 eV for CNTs.

The stability of emission current is an important aspect to be considered for the real application of CNTs in the field emission based devices. For stability test, the emission current of the CNT emitters was held at a maximum value by increasing the electric field to a certain value which was maintained for a duration of 15 h. We observed only a small degradation of the emission current from the CNTs subjected to such stringent conditions over a long period of time. It is observed that the emission current from CNT emitters on Ni/Cr coated SS remained at a steady level over an extended period of time during the stability tests. However, the current from CNT emitters on pristine SS deteriorated at a higher rate when the starting currents were held at the same level. Although the CNT emitters on pristine SS demonstrated greater field enhancement than the CNT emitters on Ni/Cr coated SS, the emission current is less stable because of the absence of buffer layer. The presence of the buffer layer of Cr enhances the adhesion of CNTs to the substrate and the CNTs would not peel off during the stability test. The critical current, which is the maximum current that can be delivered through a single CNT before the breakdown, from an individual CNT increases with the diameter of the

CNT. The critical current for the CNTs with diameters in the range of 5-20 nm is 2-15 μA while the CNTs of diameter of about 30 nm can withstand a current of 40-250 μA [25]. The CNTs in the present work has diameter about 100 nm and are expected to withstand greater current preventing from thermal degradation. Considering the density CNTs of 2×10^9 /cm^2 (estimated from the SEM images) and the emission current density of 1 mA/cm^2, the current per CNT is in the range of pA which is far below the critical current that a CNT can withstand. The conductive substrate, robust contact between the CNTs and the substrate, and the high stability will benefit the field emission applications of VACNTs.

5.4. Conclusions

In summary, vertically aligned CNTs have been synthesized on stainless steel substrates with or without chemical etching or catalyst deposition. The density and length of CNTs are determined by the synthesis time. For a prolonged growth time, the catalyst activity will be terminated and the plasma will start etching CNTs destructively. Chemical treatment of the substrate before the synthesis has a profound effect on the diameter and length of the CNTs. CNTs with uniform diameter and length have been synthesized on SS substrates subjected to chemical etching for a period of 40 minutes before the growth. In comparison to the CNTs synthesized on Ni/Cr coated SS, the CNTs synthesized on pristine SS substrates have demonstrated better field emission properties with lower turn-on and threshold voltages but higher field enhancement. The decrease in the contact resistance resulted in the improved emission behavior from CNT emitters.

These CNT emitters could facilitate the direct fabrication of CNT structures compatible with novel nanoelectronic devices.

5.5 References

[1] Iijima S 1991 *Nature* 354, 56

[2] Deheer W A, Chatelain A and Ugarte D 1995 *Science* 270, 1179

[3] Yun Wang and Yeow J T W 2008 *Journal of Sensors* 2009, 493904 1

[4] Ng S H, Wang J, Guo Z P, Wang G X and Liu H K 2005 *Electrochimica Acta* 51, 23

[5] Zhifeng Ren, Yucheng Lan and Wang Y eds 2013 *Physics of direct current plasma enhanced chemical vapor deposition* (Berlin: Springer)

[6] Wang Y, Rybczynski J, Wang D Z, Kempa K, Ren Z F, Li W Z and Kimball B 2004 *Applied Physics Letters* 85, 4741

[7] Neupane S, Lastres M, Chiarella M, Li W Z, Su Q M and Du G H 2012 *Carbon* 50, 2641

[8] Koehne J, Li J, Cassell A M, Chen H, Ye Q, Ng H T, Han J and Meyyappan M 2004 *Journal of Materials Chemistry* 14, 676

[9] Talapatra S, Kar S, Pal S K, Vajtai R, Ci L, Victor P, Shaijumon M M, Kaur S, Nalamasu O and Ajayan P M 2006 *Nature Nanotechnology* 1, 112

[10] Lahiri I, Oh S W, Hwang J Y, Cho S, Sun Y K, Banerjee R and Choi W 2010 *Acs Nano* 4, 3440

[11] Duy D Q, Kim H S, Yoon D M, Lee K J, Ha J W, Hwang Y G, Lee C H and Bach T C 2009 *Applied Surface Science* 256, 1065

[12] Parthangal P M, Cavicchi R E and Zachariah M R 2007 *Nanotechnology* 18, 185605 1

[13] Wang N and Yao B D 2001 *Applied Physics Letters* 78, 4028

[14] Park D, Kim Y H and Lee J K 2003 *Carbon* 41, 1025

[15] Masarapu C and Wei B Q 2007 *Langmuir* 23, 9046

[16] Baddour C E, Fadlallah F, Nasuhoglu D, Mitra R, Vandsburger L and Meunier J L 2009 *Carbon* 47, 313

[17] Kim B, Chung H, Chu K S, Yoon H G, Lee C J and Kim W 2010 *Synthetic Metals* 160, 584

[18] Lin C L, Chen C F and Shi S C 2004 *Diamond and Related Materials* 13, 1026

[19] Abad M D, Srichez-Lopez J C, Berenguer-Murcia A, Golovko V B, Cantoro M, Wheatley A E H, Fernandez A, Johnson B F G and Robertson J 2008 *Diamond and Related Materials* 17, 1853

[20] Bower C, Zhou O, Zhu W, Werder D J and Jin S H 2000 *Applied Physics Letters* 77, 2767

[21] Chhowalla M, Ducati C, Rupesinghe N L, Teo K B K and Amaratunga G A J 2001 *Applied Physics Letters* 79, 2079

[22] Buffat P and P B J 1976 *Phys Rev A* 13, 2287

[23] Chen G H, Shin D H, Iwasaki T, Kawarada H and Lee C J 2008 *Nanotechnology* 19, 415703 1

[24] Pandey A, Prasad A, Moscatello J P and Yap Y K 2010 *ACS Nano* 4, 6760

[25] Doytcheva M, Kaiser M and de Jonge N 2006 *Nanotechnology* 17, 3226

CHAPTER 6.0

Fabrication of CNT/SnO_2 core-shell structure

This chapter describes the synthesis of arrays of vertically aligned carbon nanotube (CNT) and the fabrication of CNT/SnO_2 core-shell structures. Arrays of vertically aligned CNTs were synthesized on stainless steel substrate by plasma enhanced chemical vapor deposition (PECVD) and the coating of SnO_2 nanoparticles on the CNT array was realized by a wet chemical route.

6.1 Introduction

SnO_2 is a wide band n-type semiconductor which finds enormous potentials for the applications in conductive electrodes, transparent coatings, solar cells, and gas sensors [1-3]. SnO_2 based materials are suitable candidates for the future generation of anode materials for Li-ion batteries as a consequence of their high theoretical Li-ion storage capacity and low potential of Li-ion intercalation [4]. Despite having the maximum theoretical charge storage capacity (781 $mAhg^{-1}$) over twice as much as the carbon anodes (372 $mAhg^{-1}$), SnO_2 based materials have to overcome the high volume change occurring during the charging and discharging processes [5]. In order to improve the stability and reversible cyclic performance of the electrodes, SnO_2 could be incorporated with CNTs to absorb the large stress developed during the alloying and dealloying processes [6]. CNTs exhibit excellent mechanical strength and superior electrical properties and hence show good cyclic stability. The large surface area of the SnO_2 provides more reaction sites, and the small size could shorten the diffusion length

for Li^+ insertion. Hence, it is reasonable to decorate CNTs with a uniform layer of SnO_2 nanoparticles to enhance the performance of Li-ion batteries.

SnO_2 based films have been deposited by evaporation, chemical vapor deposition, sputtering, sol-gel deposition, hydrothermal method, screen printing *et cetera* [7-9]. However, uniformly distributed SnO_2 nanoparticles can also be synthesized using wet chemical routes using $SnCl_2$ salt solution in water in an acidic medium [10]. There are several reports of coating CNTs with SnO_2 using various approaches. For example, Han *et al*. deposited SnO_2 nanoparticles on randomly oriented CNTs using a wet chemical route [10]. Noerochim *et al*. coated CNTs with SnO_2 nanoparticles by using $SnCl_4$ and H_2O_2 in a hydrothermal reaction [11]. Du *et al*. synthesized CNT/SnO_2 core-shell structure by a layer by layer technique accompanied by heat-treatment [12]. Most of these reported results are aimed at coating SnO_2 on randomly oriented CNTs.

A uniform layer of SnO_2 has been successfully coated on arrays of vertically aligned CNTs through a simple wet-chemical route [10]. Free-standing arrays of CNTs were synthesized on stainless steel (SS) substrate by plasma enhanced chemical vapor deposition (PECVD) process. The robust contact of the CNTs with the substrate ensured the fabrication of CNT/SnO_2 core-shell structure preserving the vertical alignment of CNTs during the coating process. The in-situ synthesis of CNTs on conductive substrates and fabrication of CNT/SnO_2 core-shell structures provides a direct platform for testing novel anode material for Li-ion battery. These free-standing, vertically aligned CNT/SnO_2 core-shell structures are capable of exhibiting better performance as electrode

materials in Li-ion battery as the electrolytes will have an easy access to a large surface area.

6.2 Experimental methods

Stainless steel substrates were chemically etched in a mixture of concentrated H_2SO_4: H_2O_2: H_2O (4:1:15, volume ratio) for 40 minutes in an ultrasonic bath and vertically aligned CNTs (VACNTs) were synthesized by DC-PECVD as described earlier in chapter 3. Briefly, the synthesis was carried at 600 °C for 5 min at a pressure of 8 torr using a mixture of NH_3 and C_2H_2 [13]. The as-synthesized VACNTs were functionalized by submerging in concentrated HNO_3 for 2 h at room temperature, then the functionalized sample was submerged in a bath of 2 g $SnCl_2$, 80 ml H_2O, and 1.4 ml concentrated HCl for 15 h for the SnO_2 deposition. Compressed air was bubbled through the solution to provide a gentle stirring throughout the acid-treatment and coating procedures to facilitate a uniform SnO_2 deposition.

6.3 Results and discussions

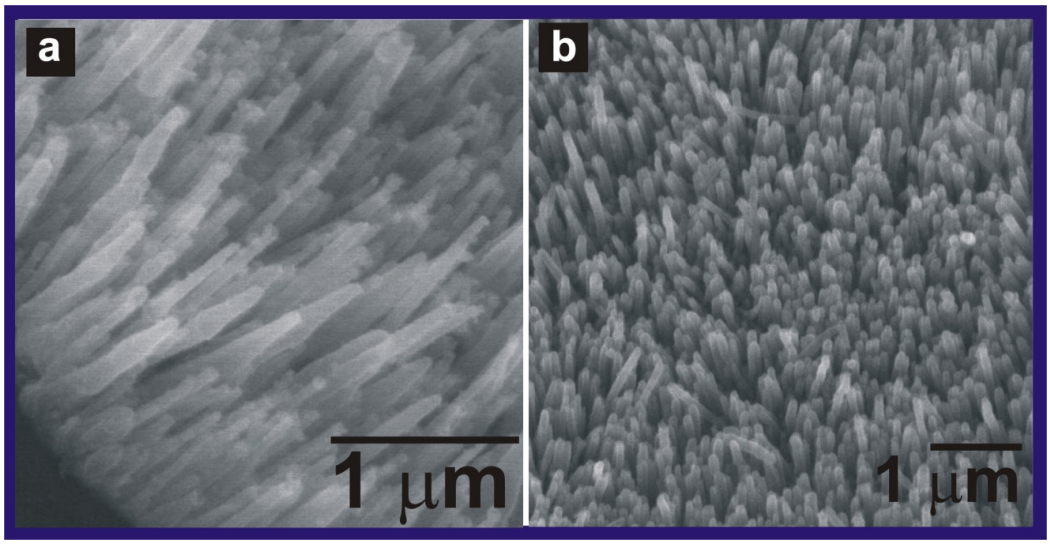

Figure 6.1: *SEM images of SnO_2 coated CNTs. (a) Side-view image showing the entire length of the SnO_2 coated CNTs and (b) 30° tilt-view image showing the retention of the alignment of the CNTs in the array after SnO_2 coating.*

In the first step, SS substrates were chemically etched as described earlier in a mixture of H_2SO_4:H_2O_2:H_2O (4:1:15, volume ratio) for different durations. The evolution of the surface for different chemical treatment time has been explained in detail on section 5.3. In brief, a 40-minute chemical etching resulted in fine particles with uniform sizes which are favorable for the growth of CNTs with uniform diameter. The CNTs synthesized on such substrates demonstrated a uniform diameter and length, Fig. 5.3. After 5 min growth, the average length of the CNTs is 2 μm. Fig. 6.1(a). The treatment of the as-synthesized CNTs using the acid bath introduces hydroxyl or carboxylic acid groups to the surface of CNTs to create a suitable hydrophilic environment necessary for the uniform coating of SnO_2 nanoparticles over the entire length of CNTs [14]. SEM

examination reveals that a uniform layer of SnO_2 is conformally coated on every tapered CNT. Most importantly, the CNT arrays retained their structural integrity after the HNO_3 treatment and subsequent SnO_2 coating procedure in a harsh chemical environment, in other words, the SnO_2 coated CNTs are still vertically aligned, well-separated from each other, and strongly connected to the SS substrate, Figs. 6.1(b) and 6.2. This remarkable stability indicates the robustness of VACNT arrays grown on SS substrate and shows the possibility of using the CNT/SnO_2 core-shell structure as anode materials for Li-ion batteries.

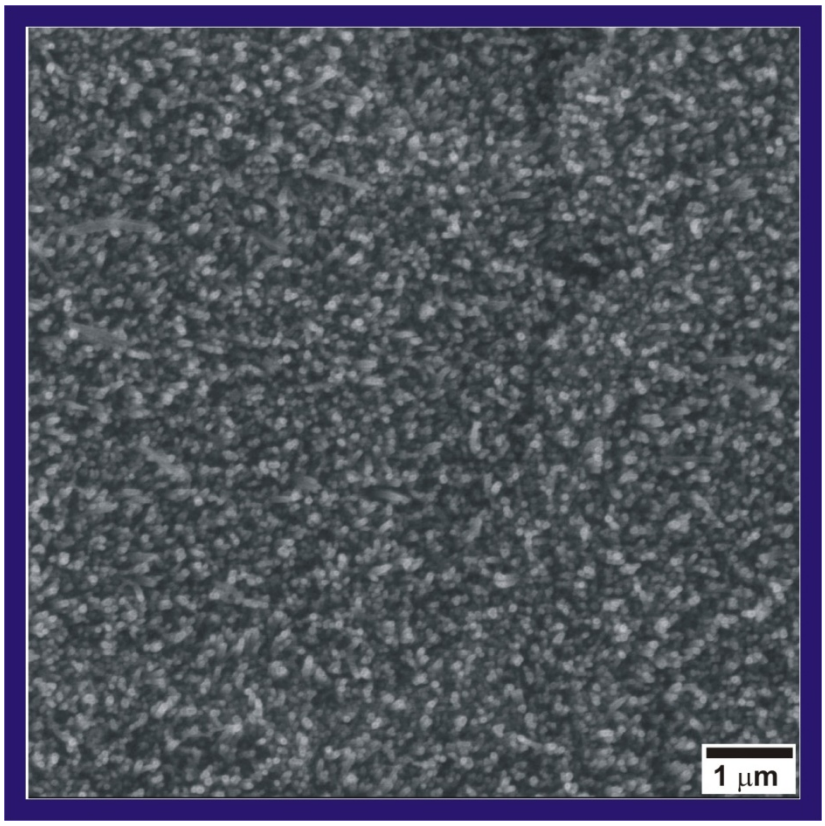

Figure 6.2: *SEM images of SnO_2 coated CNTs. Top-view image showing a large area of CNTs after SnO_2 deposition.*

Transmission electron microscopy investigations of the CNTs revealed the morphology and distribution of SnO_2 nano-particles on the surfaces of CNTs. It can be observed that all CNTs have been fully coated with SnO_2 particles to form a core-shell CNT/SnO_2 structures. The underlying chemical reaction which governs the formation of SnO_2 particles from the precursor $SnCl_2$ in aqueous solution is as follows [15]:

$$2SnCl_2 \cdot H_2O + O_2 \rightarrow 2SnO_2 + 4HCl$$

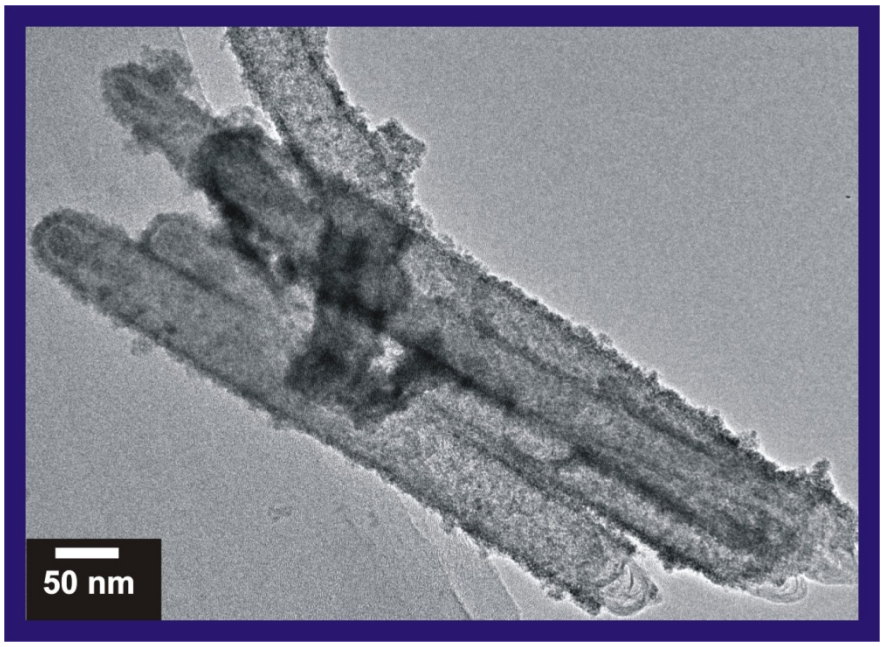

Figure 6.3: *TEM images of CNT/SnO_2 core-shell structures. CNTs with uniform SnO_2 coverage along their entire length.*

Firstly, the tin (Sn^{2+}) ions are adsorbed on the surface of CNTs functionalized by HNO_3 acid-treatment due to electrostatic interaction. These ions are then oxidized due to the presence of residual oxygen in the solution to become SnO_2 nanocrystals [15]. The addition of HCl with the reactants prevents the hydrolysis of $SnCl_2$ and suppresses the

formation of SnO particles. The low resolution TEM images show the complete coverage of SnO_2 around CNT samples, Fig. 6.3. It is observed that SnO_2 particles cover the entire length of CNTs to form a core-shell structure. It was reported that defect sites on the graphitic edges of CNTs is favorable for the formation of SnO_2 nanoparticles on the CNT surface [14]. In our experiment, the CNTs synthesized by PECVD contain a myriad of topological defects as a result of fast growth rate under the plasma. The high density of defects on the surface of VACNTs leads to the formation of a layer of SnO_2 nanoparticle on the entire surface of CNTs. Figures 6.4(a-b) also show the TEM images of CNT/SnO_2 core-shell structures at higher magnifications. The degree of surface coverage and uniformity of the SnO_2 nanoparticles is remarkable in these samples. The high-resolution TEM (HRTEM) image (Fig. 6.5(a)) shows a section of lattice planes with the interplanar separation of 0.33 nm and 0.27 nm corresponding to (110) and (101) planes of tetragonal phases of SnO_2. The selected area diffraction (SAED) pattern (Fig. 6.5(b)) depicts the polycrystalline nature of SnO_2 layer. Histograms of SnO_2 nanoparticles on the CNT/SnO_2 core-shell structure demonstrate a narrow size distribution of SnO_2 nanoparticles with an average size of 4 nm (Fig. 6.5(c)).

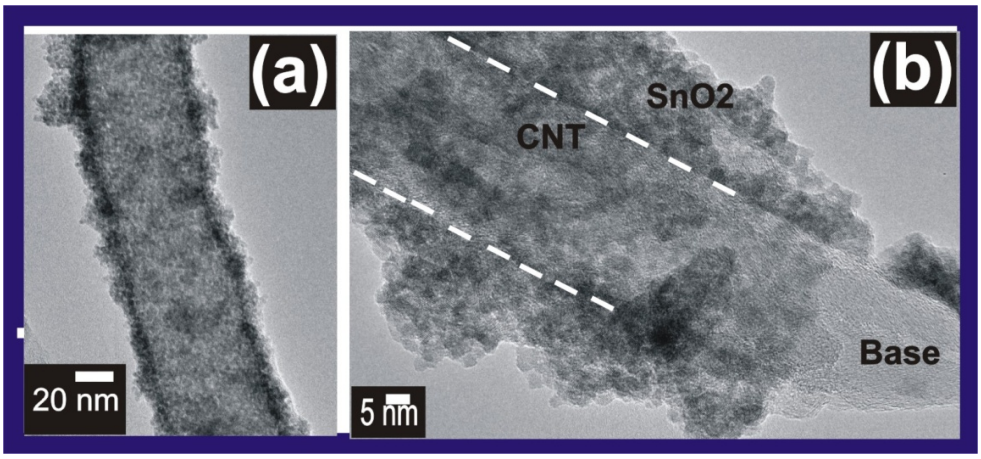

Figure 6.4: *TEM images of CNT/SnO_2 core-shell structures. (a) Magnified view of a CNT/SnO_2 core-shell structure, showing clearly the SnO_2 coating layer on the CNT surface. (b) Magnified view of the base region of a CNT/SnO_2 core-shell structure, showing that a layer of SnO_2 can be formed at the root region of the CNT. The dashed white line shows the interface between the CNT and the layer of SnO_2 nanoparticles.*

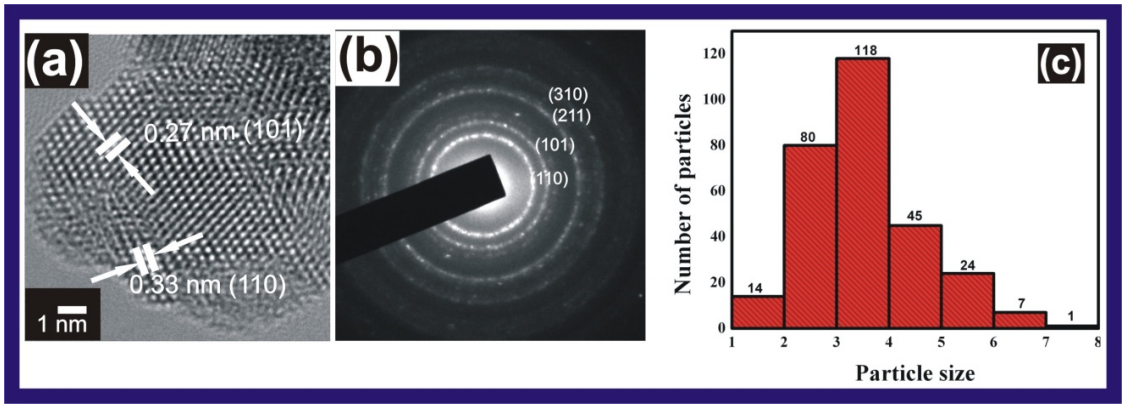

Figure 6.5: *TEM images of CNT/SnO_2 core-shell structures (a) HRTEM image of SnO_2 nanoparticles showing clear lattice fringes separated by a distance of 0.33 nm and 0.27 nm, which can be assigned to the interplanar distances corresponding to the (110) and (101) planes, respectively, of the SnO_2 crystal. (b) A SAED pattern confirming the polycrystalline nature of SnO_2 layer. (c) A histogram showing the size distribution of the SnO_2 nanoparticles in CNT/SnO_2 core-shell structures.*

6.4 Conclusions

In summary, we have fabricated large arrays of freely-standing vertically aligned CNT/SnO_2 core-shell structures by a simple wet-chemical route. CNTs with large number of surface graphitic edges provide large number of nucleation sites for a uniform deposition of SnO_2 nanoparticles. The strong adhesion of CNTs with the conducting substrate like stainless steel provides a perfect robust structure for realizing core-shell structures of CNTs with SnO_2 or other metal oxides. Such a uniform CNT/SnO_2 core-shell structure is expected to show high performance as electrode materials in rechargeable batteries. Further experiments are ongoing in our laboratory to measure the charge-discharge capacity of these core-shell structures as anode materials in Li-Ion batteries.

6.5 References

[1] Idota Y, Kubota T, Matsufuji A, Maekawa Y and Miyasaka T 1997 *Science* 276, 1395

[2] Wei B Y, Hsu M C, Su P G, Lin H M, Wu R J and Lai H J 2004 *Sensors and Actuators B-Chemical* 101, 81

[3] Zhou J G, Fang H T, Maley J M, Ko J Y P, Murphy M, Chu Y, Sammynaiken R and Sham T K 2009 *Journal of Physical Chemistry C* 113, 6114

[4] Ding S J, Chen J S and Lou X W 2011 *Chemistry-an Asian Journal* 6, 2278

[5] Paek S M, Yoo E and Honma I 2009 *Nano Letters* 9, 72

[6] Parthangal P, Cavicchi R E, Meier D C, Herzing A and Zachariah M R 2011 *Journal of Materials Research* 26, 430

[7] Kohl D 2001 *Journal of Physics D-Applied Physics* 34, R125

[8] Simon T, Barsan N, Bauer M and Weimar U 2001 *Sensors and Actuators B-Chemical* 73, 1

[9] Zhao L P and Gao L 2004 *Carbon* 42, 1858

[10] Han W Q and Zettl A 2003 *Nano Letters* 3, 681

[11] Noerochim L, Wang J Z, Chou S L, Li H J and Liu H K 2010 *Electrochimica Acta* 56, 314

[12] Du N, Zhang H, Chen B D, Ma X Y, Huang X H, Tu J P and Yang D R 2009 *Materials Research Bulletin* 44, 211

[13] Neupane S, Lastres M, Chiarella M, Li W Z, Su Q M and Du G H 2012 *Carbon* 50, 2641

[14] Fang H T, Sun X, Qian L H, Wang D W, Li F, Chu Y, Wang F P and Cheng H M 2008 *Journal of Physical Chemistry C* 112, 5790

[15] Wang Z Y, Chen G and Xia D G 2008 *Journal of Power Sources* 184, 432

CHAPTER 7.0

Conclusions

7.1 Summary

This dissertation presents the results of synthesis and electron field emission properties of aligned carbon nanotube (CNT) arrays. Plasma enhanced chemical vapor deposition (PECVD) method was employed to fabricate CNT arrays on copper or stainless steel substrate. It was demonstrated that CNT arrays can be directly synthesized on conducting metal surface and used as efficient in-situ electron field emitters.

The as-synthesized high density CNT emitters demonstrated a low field enhancement and high turn-on and threshold electric fields. Low density of CNTs synthesized by nanosphere lithography showed increased field enhancement and decreased turn-on and threshold electric fields. More specifically, CNTs synthesized on the catalyst dots patterned by using polystyrene spheres of 0.5 μm during nanosphere lithography displayed the best electron emission properties. The low density of CNTs reduces the screening of the electric field and results in the improved electron emission.

CNTs treated by NH_3 plasma for different durations increased their electron emission properties due to their morphology change from cylindrical shape to tapered shape after plasma treatment. Plasma treatment resulted in the increase in the aspect ratio of CNTs, introduction of defects, increase in the inter-tip distance, nitrogen doping, and the opened tip. As a result, CNTs subjected to 1.0 min of NH_3 plasma treatment exhibited the greatest improvement in their field emission properties. This result indicates that NH_3

plasma treatment could be an effective approach to improve the field emission performance of CNTs.

The electron emission properties of CNT point emitters grown on copper wires with flat or sharp tips were also studied. The two types of point emitters have exhibited excellent field emission performance, such as high emission current at relatively low voltage and longtime emission stability at high current level. The excellent field emission properties are attributed to the point emitter structure and the good contact between the CNTs and the Cu tip. These CNT point emitters grown on Cu wires can find possible applications in miniaturized X-ray sources and electron beam sources.

Vertically aligned CNTs were synthesized on stainless steel (SS) substrates with or without chemical etching or catalyst deposition. The density and length of the CNTs synthesized on SS substrates were determined by the synthesis time. For a prolonged growth time, the catalyst activity terminated and the plasma started etching the CNTs destructively. CNTs with uniform diameter and length have been synthesized on SS substrates subjected to chemical etching for a period of 40 minutes before the growth. In comparison to the CNTs synthesized on Ni/Cr coated SS, the CNTs synthesized on pristine SS substrates have demonstrated better field emission properties with lower turn-on and threshold voltages and higher field enhancement due to the decrease in the contact resistance. However, the CNTs emitters synthesized on pristine SS substrates exhibited a sharper decline during the stability tests as compared to the CNT emitters synthesized on Ni/Cr coated SS. These CNT emitters could facilitate the direct fabrication of CNT structures compatible with novel nanoelectronic devices. The growth of CNT emitters on

metal substrates may be applied for development of other types of nanoelectronic devices.

Finally, large arrays of freely-standing vertically aligned CNT/SnO_2 core-shell structures were fabricated by a simple wet-chemical route. CNTs with large number of surface graphitic edges provided a large number of nucleation sites for a uniform deposition of SnO_2 nanoparticles. The average size of SnO_2 nanoparticles on the CNT/SnO_2 core-shell structure was 4 nm. Such uniform CNT/SnO_2 core-shell structure is expected to show high performance as electrode materials in rechargeable batteries.

7.2 Future Work

This dissertation has outlined various approaches to fabricate CNT emitters with improved electron field emission properties. The proposed strategies suggest new directions for the possible development of CNT emitters in the near future. However, some of the topics require further investigations for real applications.

In case of CNT emitters with different densities, the proposed nanosphere lithography technique still needs to be optimized to achieve a better control over the density and size of catalyst dots. The catalyst dots can be further subjected to thermal treatment or plasma treatment to reduce their sizes to grow a single CNT from each catalyst site. The size of the catalyst dot can be reduced by angled deposition and double layer formation of the polystyrene spheres in nanosphere lithography, chemical etching or other approaches. More comprehensive studies can be performed by changing the synthesis time to obtain CNTs with different aspect ratio but with similar densities.

Computational simulations can be performed to confirm and explain the observed experimental results.

There are further possibilities of comparing the results of using various gases during plasma treatment to determine the most effective gas for plasma treatment of CNTs. Different gases generate plasma with different intensities and their bonding affinity with graphitic layers also differ. Thus the plasma treatment can be optimized to develop CNT emitters with higher field enhancement. Point emitters can also be subjected to plasma treatment to investigate the possibility of further enhancement of field emission. In addition, point emitters can also be fabricated by attaching CNTs at the tip by dielectrophoresis or other methods. The field emission properties and stability of point emitters fabricated by direct synthesis and the emitters formed by mechanical attachment can be further compared.

Vertically aligned CNT/SnO_2 core-shell structures have been synthesized and further experiments can be performed to fabricate Li-ion battery using such core-shell structures as anode materials. Experiments can also be conducted to open the tips of these CNTs to deposit SnO_2 particles both in the interior and exterior of the CNTs to increase the mass-fraction of SnO_2.

VITA

SUMAN NEUPANE

2014	Doctoral Candidate Florida International University, Florida, United States
2005	Master of Science Tribhuvan University, Kathmandu, Nepal
2001	Bachelor of Science Tribhuvan University, Kathmandu, Nepal

PUBLICATIONS AND SELECTED PRESENTATIONS

Journal articles:

1. Q, Su, G. Du, J, Zhang, Y. Zhong, B. Xu, Y. Yang, S. Neupane, W. Z. Li, "*In situ transmission electron microscopy observation of electrochemical sodiation of individual Co9S8 filled carbon nanotubes*", ACS Nano, 10.1021/nn500194q (2014).

2. Q, Su, G. Du, J, Zhang, Y. Zhong, B. Xu, Y. Yang, S. Neupane, K. Kadel, W. Z. Li, "*In situ Transmission Electron Microscopy Investigation of the Electrochemical Lithiation–Delithiation of Individual Co_9S_8/Co–Filled Carbon Nanotubes*", ACS Nano, 7 (2013) 11379-11387.

3. M. Yang, S. Neupane, X. Wang, J. He, W. Z. Li, N. Pala, "*Multiple step growth of single crystalline rutile nanorods with the assistance of self-assembled monolayer for dye sensitized solar cells",* ACS Applied Materials &Interfaces 5 (2013) 9809−9815.

4. S. Neupane, Y. Yang, W.Z. Li, Y. Gao *"Synthesis and enhanced electron field emission of vertically aligned carbon nanotubes grown on stainless steel substrate*", Journal of Nanoscience Letters, 2014 14:4 (2013).

5. G. H. Chen, S. Neupane, W. Z. Li, L. Chen, J. Zhang, "*An increase in the field emission from vertically aligned multiwalled carbon nanotubes caused by NH_3 plasma treatment*", Carbon 50 (2013), 468-475.

6. S. Neupane, M. Lastres, M. Chiarella, W. Z. Li, Q. Su, G. H. Du, "*Synthesis and field emission properties of vertically aligned carbon nanotube arrays on copper*", Carbon 50 (2012) 2641-2650.

7. G. H. Chen, S. Neupane, W. Z. Li, "*Electron field emission properties of vertically aligned carbon nanotube point emitters*" Diamond and Related Materials, 25 (2012), 134-138.

8. S. Neupane, G. Kaganas, R. Valenzuela, L. Kumari, X. W. Wang, W. Z. Li, "*Synthesis and characterization of ruthenium dioxide nanostructures*", Journal of Materials Science, 46, (2011) 4803-4811.

Proceedings Paper:

1. S. Neupane, W.Z. Li, Proceedings of 26th International Vacuum Nanoelectronics Conference IVNC (2013) 1-2, DOI: 10.1109/IVNC.2013.6624720.

Book Chapter:

1. S. Neupane, W. Z. Li "*Carbon Nanotube Arrays: Synthesis, Properties and Applications*" Chapter 10 in Three-Dimensional Nanoarchitectures: Designing Next-Generation Devices, Springer, (2011), 261-285.

Selected presentations:

1. S. Neupane, W.Z. Li, "*Synthesis and Electron Field Emission from Vertically Aligned Carbon Nanotubes on Stainless Steel Substrate*" International Vacuum Nanoelectronics Conference (IVNC), Roanoke-VA July 8-12, 2013.

2. S. Neupane, W. Z. Li, "*Synthesis and field emission properties of periodic arrays of vertically aligned carbon nanotubes on copper*", American Physical Society-APS March Meeting, Boston-MA, Feb 27- Mar 2, 2012.

3. S. Neupane, W. Z. Li, "*Synthesis and field emission properties of vertically aligned carbon nanotube arrays*", 4th Nanoscience Technology Symposium NanoFlorida™ 2011, Miami-FL, Sep 30-Oct 1, 2012.

4. S. Neupane, L. Kumari, G. Kaganas, W. Z. Li, "*Synthesis and characterization of ruthenium dioxide nanorods*", American Physical Society-APS March Meeting, Portland- OR, Mar 15- Mar 19, 2010.